THE UNIVERSITY OF CHICAGO

NON-UNIFORM SINGLE-CELL AND SUBCELLULAR GLYCOLYSIS FUELS HETEROGENEOUS CELL MOTILITY

A DISSERTATION SUBMITTED TO

THE FACULTY OF THE DIVISION OF THE PHYSICAL SCIENCES

AND

THE FACULTY OF THE DIVISION OF THE BIOLOGICAL SCIENCES

AND THE PRITZKER SCHOOL OF MEDICINE

IN CANDIDACY FOR THE DEGREE OF

DOCTOR OF PHILOSOPHY

GRADUATE PROGRAM IN BIOPHYSICAL SCIENCES

BY

DEVIN HARRISON

CHICAGO, ILLINOIS

AUGUST 2021

Copyright © 2021 by Devin Harrison
All Rights Reserved

TABLE OF CONTENTS

LIST OF FIGURES v

LIST OF TABLES vii

ACKNOWLEDGEMENTS viii

ABSTRACT xi

1 GENERAL INTRODUCTION 1

1.1 Motivation and short summary 1
1.2 Endothelial cell motility: signaling, structure, and energetic demand 4
1.3 Energetic metabolism: overview and methods 6
1.4 About this dissertation 8

2 LACTATE PRODUCTION RATE (LPR) IS A SINGLE-CELL MEASUREMENT OF GLYCOLYSIS 10

2.1 Introduction 10
2.2 Single-cell lactate production rate method and benchmarking 12
2.3 Single-cell LPR of activated endothelial and T cells 16
2.4 LPR distinguishes heterogeneous metabolic populations in response to flow 19
2.5 Conclusions and future directions 21

3 ENDOTHELIAL CELL MOTILITIES ARE DRIVEN BY GLYCOLYSIS 23

3.1 Introduction 23
3.2 Migratory cells are more glycolytic than stationary cells 24
3.3 RhoA stimulation triggers a glycolytic burst 26
3.4 RhoA activates contractile machinery through glycolysis 28
3.5 Conclusions and future directions 30

4 SLC2A3/GLUT3 CONTRIBUTES TO RHOA-TRIGGERED ENDOTHELIAL CELL CONTRACTION 32

4.1 Introduction 32
4.2 Comparative SLC2A3/GLUT3 and SLC2A1/GLUT1 studies in endothelial cell contraction 32
4.3 SLC2A3/GLUT3 is translocated to the membrane during contraction to up regulate glycolysis 36
4.4 SLC2A3/GLUT3-dependent contraction is conserved across multiple endothelial cell types 39
4.5 SLC2A3/GLUT3 endothelial overexpression *in vivo* increases vascular leak 41
4.6 Conclusions and future directions 44

5 RHOA COORDINATES SUBCELLULAR GLYCOLYSIS WITH CYTOSKELETAL REMODELING 45

5.1 Introduction 45

5.2 Subcellular LPR is spatially heterogeneous and overlaps with actin remodeling..... 45
5.3 Subcellular distribution of LPR and RhoA activity are similar..... 48
5.4 Conclusions and future directions..... 52

6 CONCLUSIONS AND PERSPECTIVES..... 54

6.1 Introduction..... 54
6.2 Mechanotransduction and the metabolon..... 55
6.3 Motility and glycolysis in other cell types..... 57
6.4 Lactate as an epigenetic regulator..... 59
6.5 SLC2A3 in human health..... 60
6.6 Conclusions..... 52

APPENDIX I: SINGLE-CELL LACTATE PRODUCTION RATE PROTOCOL..... 64

A.I.1 Summary..... 64
A.I.2 Before you begin..... 65
A.I.3 Key resources table..... 69
A.I.4 Materials and equipment..... 72
A.1.5 Step-by-step method details..... 74
A.1.6 Expected outcomes..... 93
A.I.7 Quantification and statistical analysis..... 93
A.I.8 Additional Controls..... 96
A.I.9 Limitations..... 97
A.I.10 Troubleshooting..... 97
A.I.11 Figures and Tables..... 100

APPENDIX II: MATERIALS AND METHODS..... 109

CONTRIBUTION STATEMENT..... 131

BIBLIOGRAPHY..... 133

LIST OF FIGURES

Figure 2.1: Single-cell metabolism methodology 11

Figure 2.2: Single-cell metabolic assay utilizes deep learning-enabled segmentation of a lactate-sensing probe 13

Figure 2.3: The LPR assay reflects the glycolytic rate of individual cells. 15

Figure 2.4: Single-cell lactate levels mimic traditional metabolic measurements 16

Figure 2.5: LPR is able to distinguish metabolic subpopulations 17

Figure 2.6: Additional glycolytic metabolites are measurably increased following DMOG stimulation 18

Figure 2.7: Single-cell LPR can be extended to other metabolically dynamic cell types 19

Figure 2.8: Endothelial LPR in response to shear stress is heterogeneous 21

Figure 3.1: Glucose consumption via glycolysis fuels migration 24

Figure 3.2: Single-cell metabolism links migratory cell phenotypes to glycolytic states 25

Figure 3.3: Single-cell imaging of lactate production reveals RhoA drives endothelial cell glycolysis 27

Figure 3.4: Glycolysis is necessary for activation of contractile machinery 29

Figure 4.1: Inhibition of SLC2A3 but not SLC2A1 reduces RhoA activation of contractile machinery 33

Figure 4.2: SLC2A3 knockdown prevents RhoA-induced glycolysis 35

Figure 4.3: SLC2A3 localization to the membrane contributes to contraction 37

Figure 4.4: Contraction under SLC2A3 knockdown is partially rescued by increasing glucose availability 38

Figure 4.5 SLC2A3 inhibition abrogates thrombin-induced phosphorylation of CFL and MLC and contraction across multiple endothelial cell types 40

Figure 4.6: *In vivo* over expression of SLC2A3 increases vascular leak 43

Figure 5.1: Subcellular distribution of LPR colocalizes with actin remodeling in contractile cells 47

Figure 5.2: Subcellular distribution of LPR colocalizes with actin remodeling in migratory cells 48

Figure 5.3: Subcellular RhoA activity and LPR are spatially similar 50

Figure 5.4: RhoA activity is highest at the center of cells and contractile cell edges 51

Figure 5.5: Proposed mechanism of RhoA regulating glycolysis and contraction 52

Figure 6.1: Non-uniform single-cell and subcellular glycolysis fuels heterogeneous motility 63

Figure A.I.1: Comparison of different methods of Laconic expression in endothelial cells 100
Figure A.I.2: Ibidi imaging chamber assembly 101
Figure A.I.3: Laconic calibration curve 103
Figure A.I.4: Deep learning architecture for semantic segmentation 104
Figure A.I.5: Training and validation of the convolutional neural network 105
Figure A.I.6: Single field-of-view segmentation example 105
Figure A.I.7: LPR single-cell trace 106
Figure A.I.8: LPR bulk data for distinguishable populations in HAECs treated with control vs DMOG. 106
Figure A.I.9: Ground truth fluorescence vs. predicted fluorescence 107
Figure A.I.10: Total quantification of LPR 107

LIST OF TABLES

Table 2.1: Deep learning semantic segmentation evaluation metrics 14

Table A.I.1: Generating Laconic template for *in vitro* transcription..... 101
Table A.I.2: Solutions for calibration curve 102
Table A.I.3: Example solution calculator for LPR injection solutions 103

Table A.II.1: RhoA, mCherry, and eBFP2 over expression primers 110
Table A.II.2: Quantitative real-time PCR (qRT-PCR) primers 125
Table A.II.3: CDH5-Glut3 construction primers 131

ACKNOWLEDGEMENTS

Any success I've had has been a direct result of the supportive people around me. I must start by thanking my graduate program which first set me up to succeed. I have to thank the administrators, specifically Michele Wittels, Julie Feder, and Adam Hammond who have been there for me since the beginning. They are the best part of the program and without them, I couldn't recommend such a hard-fought path to a PhD. I also must thank my cohort: Hallie Sussman, Wenli Dai, Yifan Zhou, Alan Selewa, Andrés Moya Rodríguez, Amar Risbud, and Evan Kiefl. They have been teaching me since we started together and I'm most excited to share my research progress with them, knowing each person has their own unique perspective forged from their background and current fields of study (plus they are very fun which we all need during such arduous and focused work.)

I was immediately drawn to the Biophysical Sciences PhD program at UChicago where students are required to select two advisors from disparate scientific fields and design a project that unites the primary investigators' research programs while forging the student's own. Luckily, I found two advisors, Yun Fang and Jun Huang, who have been incredibly supportive. There are so many students who don't have the opportunity to feel both valued as a scientist and cared about as an individual by their mentors. Beyond supporting me as their mentee, they also were staunch allies to a woman in science. I've seen many toxic scientific lab cultures and I can say with certainty, you won't find those usual antics anywhere near these labs. Yun has been an exceptional boss: he always encouraged and allowed me to go after the hard problems and experiments that I designed myself, he's not afraid of new technology or new research avenues so long as it's interesting and worthwhile, and he's always able to see the big picture, especially when I get stuck in the nitty gritty, and communicate it in an efficient way. Jun has always served as a role model, being one of the hardest working and self-disciplined scientists I've met, pushing me out of my

comfort zone but never too far that I can't gain confidence in a new research area. He's also helped me develop my writing and presentation skills in a way that I'll always be using. I'll forever be grateful for my time working with Jun and Yun. If there are any future students reading this, looking for advisors—pick these two!!

Next, I must acknowledge Dave Wu, the co-first author on both of my first author publications during my PhD. Dave is, in my mind, a humble genius. He understands so much about basic science while still able to switch into clinical mode where he relates basic cellular biology to complex pathologies. I have grown so much as a scientist from our talks looking at weird data, forming hypotheses, or lamenting about the state of academia. He doesn't judge my lack of understanding of something but instead is eager to explain it further. More importantly, he's always listened to me, and for that, I'm grateful.

Aside from my professional acknowledgements, I must thank the support network that I grew in Chicago. Specifically, I wouldn't have been able to get through any of this without my first and closest friend in Chicago, Eunie Cho, who always celebrated my achievements when I didn't see them as such, listened to me complain and offered useful solutions to my problems, and most importantly, served as a role model for being a hard-working woman who doesn't let anything stop her. Additionally, my quarantine pod helped get me through some of the worst and best times of my PhD: Steven Redford, Meike Lobb-Rabe, Emily Fogarty, Cat Triandafillou, Jimmy Elias, Kourtney Kroll, and Evan Kiefl, and Julianna McCorkle. I also can't forget additional Chicago friends: Maulik Jani, Steven Wasserman, Vaughn Spurrier, Elizabeth White, and Margo MacDonald. Though it's time for me to move on from Chicago, these are the people that have changed my life for the better and part of my heart will stay in Chicago forever.

Finally, I will thank the people who stuck by my side even when I abandoned them to selfishly pursue science in Chicago: my long-distance partner, New York family and Massachusetts family. Andrew, the love of my life, has received so many phone calls in the middle of the night and has always listened to me stress out about the same things all the time even though he would eventually give me the same advice and still make me feel better. He has sent me care packages to manage my stress even when it meant spending more time apart. I'm so grateful to have a partner that supports my professional life in the way that he does. Similarly, three of my best friends, Anthony, Becca and Daria, have put up with my incessant complaining and significant difference in lifestyle. Having them visit were my favorite times to explore and show off Chicago, all while blowing off steam and getting re-energized. My NY and MA families have been a motivational cornerstone in my life and I work hard solely to make them proud. My mom, specifically, is the hardest working person on the planet (the only one who tops Beyoncé) and without her serving as a role model throughout my life, I certainly wouldn't push myself as far as I do with the confidence she instilled in me to conquer absolutely anything I set my mind to.

Without a doubt, I'm sure I have missed thanking important people in my life by name. Please know that I achieved this accomplishment with you and for you and I can't wait to share what I've passionately and painstakingly worked on for the past five years.

ABSTRACT

Movement requires energy which is translated into force generated at specific locations at the organismal and cellular level. Energy production and consumption are tightly regulated to ensure efficiency by metabolic reprogramming. However, the pathways that ensure frugal use of energy remain largely unexplored. I investigate this relationship between metabolism and motility in endothelial cells which line blood vessels, are highly motile, and dictate vascular health. Direct linking cell motility which is spatially heterogeneous to cell metabolism is technically challenging but biologically important. Here, I developed single-cell metabolic imaging to measure glycolysis in individual endothelial cells using genetically-encoded biosensors capable of deciphering metabolic heterogeneity at subcellular resolution. I show that cellular glycolysis fuels endothelial activation, migration and contraction and that the high lactate production sites co-localize with active cytoskeletal remodeling within an endothelial cell. Mechanistically, RhoA induces endothelial glycolysis for the phosphorylation of cofilin and myosin light chain in order to reorganize the cytoskeleton and thus control cell motility; RhoA activation triggers a glycolytic burst through the translocation of the glucose transporter SLC2A3/GLUT3 to fuel the cellular contractile machinery, as demonstrated across multiple endothelial cell types. Altogether, this method provided data that indicates that Rho-GTPase signaling coordinates energetic metabolism with cytoskeleton remodeling to regulate the motility of single endothelial cells.

CHAPTER ONE

GENERAL INTRODUCTION

1.1 Motivation and short summary

At the organismal level, we generally understand that movement requires energy, such as in running. The carbohydrates that we take in through our diet is metabolized by our body to create glucose, which is the major fuel source for cells. Glucose is then further metabolized by cells to generate energy and when we run, this energy (in the form of ATP) is used by our contracting muscles to generate forces within our legs and arms that will propel us forward. Our brains will inform our leg muscles to move the corresponding bones forcefully in a forward direction, pressing into the ground to run. In this way, organismal movement is a multi-component transfer of energy, which occurs at a cellular level as well. Cells must migrate, contract and spread, throughout their lives in order to get where they need to be (Trepat, Chen, and Jacobson 2012): Immune cells must surveil the body looking for and eliminating harmful pathogens, neurons must migrate to connect and wire together, and endothelial cells must contract to regulate the semi-permeable vascular barrier, for example. However, aberrant cellular motility can result in complex pathologies including atherosclerosis, where the blood vessels become too permeable and consequently harden at specific locations, chronic inflammation, where immune cells over-infiltrate tissue, and cancer metastasis, where tumor cells migrate to new locations in the body and proliferate, among others. Therefore, understanding how cell movement is coordinated with energy production would be useful not only for understanding basic cell mechanics but also for the development of therapeutics against motility-related diseases.

Cell motility requires that energy production and consumption are tightly regulated to ensure efficiency by metabolic reprogramming. However, the pathways that ensure frugal use of energy remain largely unexplored. I investigate this relationship between metabolism and motility in endothelial cells which line blood vessels, are highly motile, and dictate vascular health.

Cell movement requires the reorganization of the cytoskeleton which is energy demanding. The cytoskeleton can be considered as the musculoskeletal system of individual cells and is comprised of stiff actin filaments and actin-binding molecules that regulate the length and number of filaments. Once stimulated to move, such as through the activation of RhoA, endothelial cells will dramatically change its morphology through cytoskeleton remodeling, all of which requires high energy phosphates or ATP and occurs in the cytoplasm. ATP production from glucose occurs within the cell through two major metabolic pathways, glycolysis and oxidative phosphorylation. Glycolysis produces less ATP than oxidative phosphorylation but occurs in the cytoplasm. If energy production and demand are coordinated spatially, ATP-dependent cellular processes would not be diffusion limited. Therefore, it would be possible that glycolysis could be stimulated in order to produce local ATP stores for cytoskeletal remodeling.

Endothelial cells have been previously shown to preferentially use glycolysis for energy production but how they tune the rate and location to ensure efficiency remains unknown. Bulk measurements have revealed that 1) endothelial cells preferentially utilize glycolysis for fueling migration(Kim et al. 2017), 2) endothelial cells are dynamically regulated by shear stress (D. Wu et al. 2017; Feng et al. 2017; Doddaballapur et al. 2015), and 3) endothelial motilities are tightly regulated by the Rho family of small GTPases (Geerten P. van Nieuw Amerongen et al. 2003). However, mechanistic coupling of motility to energy in typically heterogeneous cell populations

requires simultaneous information at the single-cell level. Therefore, there is a critical need for developing single-cell metabolic measurements which can inform new mechanisms by linking cell motility phenotypes to energy production in the same cell. Furthermore, measuring energy production in spatially disparate subcellular structures of a single cell is expected to have mechanistic significance in cell biology since most cells dynamically regulate their metabolic programs as a result of nutrient availability, anabolic requirements, and energy demand (some example include: Karmaus et al. 2019, 17; van Heerden et al. 2014; Hensley et al. 2016).

In order to study the regulation of energy that fuels these dramatic and heterogeneous morphological changes, I developed, with my colleague, an experimental and analytical pipeline utilizing deep-learning enabled image analysis of a genetically-encoded metabolic probe of lactate to uncover new biological links between cell motility and glycolytic rate with single- and sub-cellular resolution. This Förster resonance energy transfer (FRET) image-based approach uses deep learning (Van Valen et al. 2016; Ronneberger, Fischer, and Brox 2015) to rapidly quantify the intracellular glycolytic metabolites including lactate, glucose, pyruvate, and ATP in single endothelial cells, thus linking metabolic states to key endothelial motile phenotypes including adaptation to shear stress, migration, and contraction. A strong correlation between morphology and glycolytic rate at the single-cell level was identified, which was further confirmed by the subcellular distribution of high glycolytic rates at sites of active actin turnover. Our single-cell metabolic measurements discovered that the activation of GTPase RhoA triggers a glycolytic burst essential for the endothelial contractile machinery. I further discovered that glucose transporter SLC2A3/GLUT3 controls the RhoA-induced endothelial glycolysis and subsequent contraction. These results highlight the significance of single-cell metabolic analyses in their ability to uncover a new paradigm of small GTPase-dependent coupling of energy production to cell mobility.

Altogether, these data show that cells regulate glycolysis to meet local bioenergetic demand to ultimately fuel their physiological functions.

1.2 Endothelial cell motility: signaling, structure, and energetic demand

Endothelial cells are highly motile. They align and elongate in response to hemodynamics (Peter F. Davies et al. 2013), must migrate during angiogenesis or wound closure (Geerten P. van Nieuw Amerongen et al. 2003), and contract in order to regulate the barrier integrity of the vasculature (G. P. van Nieuw Amerongen, Vermeer, and van Hinsbergh 2000). Each of these processes are similar in that they involve drastic and heterogeneous morphological and positional changes: the shear stress that endothelial cells experience in the vasculature will vary depending on location and will dictate cell shape, the speed of a cell will differ throughout a migrating cell population, the displacement of cell edges will vary within a single cell during contraction. However, how individual cells or parts of a cell are able to use energy selectively in response to energy demand remain unknown.

Within blood vessels, there are local changes in blood flow speed which enforce a shear stress tangential to the direction flow on endothelial cells lining the lumen (Dai et al. 2004). These shear forces dictate the activation state of the endothelial cells. This change in flow is accompanied by a decrease in oxygen, both of which serves as a signal to the cells to migrate and grow to form new vessels. However, too much activation of the endothelium can result in increased permeability and formation of pathogenic plaques. Atherosclerosis has a focal nature, where atheromas occur at bifurcations in the vasculature where there is disturbed flow. Additionally, cells that are subjected to low shear stress, or disturbed flow, have increased glycolysis in comparison to cells subjected to high shear stress, or unidirectional flow (D. Wu et al. 2017). Glycolysis is upregulated

due to the decrease in oxygen, as glycolysis does not require oxygen for ATP production whereas mitochondrial creation of ATP does. However, glycolysis also produces lactate, which could serve as an angiocrine or autocrine signaling molecule. For example, endothelial derived lactate can be taken up by macrophages, polarizing them to be M2-like and promote tissue repair and growth (J. Zhang et al. 2020). Lactate can also be used as a substrate for histone lactylation, influencing chromatin architecture and subsequently gene expression (D. Zhang et al. 2019). Therefore, understanding how glycolysis is preferentially utilized and regulated in response to hemodynamics would be useful for better understanding cardiovascular homeostasis. Additionally, cells under high shear stress will align and elongate but under slow shear stress, remain in a cobblestone pattern (P. F. Davies 1995). Whether or not these features, shear stress, shape, and glycolysis, are correlated remains to be evaluated. Given the pathogenic nature of an overactivated endothelium, understanding how energetic metabolism relates to cell position and activation within the vasculature could be useful for therapeutic purposes.

Cell migration during angiogenesis or wound closure and paracellular barrier maintenance requires the coordination of the cytoskeleton and energetic metabolism. The cytoskeleton is comprised of globular (G-actin) that can polymerize into filamentous (F-actin), a process which requires ATP. The cytoskeleton is constantly remodeled during migration to form subcellular structures including stress fibers, lamellipodia, and filipodia, all to propel the cell forward (Blanchoin et al. 2014). During barrier maintenance when the endothelium will allow the passage of cells, nutrients, and waste products, the endothelial cell will form stress fibers to anchor and pull the edges inward, thus contracting. This remodeling is mediated in part by the small family of Rho GTPases including RhoA which will activate the contractile machinery (G. P. van Nieuw Amerongen et al. 2000; 2000). RhoA will signal through Rho-associated kinase 1 (ROCK1) to

downstream kinases that will activate cofilin (CFL), or actin depolymerizing factor (ADF), and myosin light chain (MLC), through phosphorylation. Cofilin works to break down or recycle actin filaments but when phosphorylated, CFL becomes inactive, thus filaments will continue to grow and remain intact. Phosphorylation allows MLC to bind to actin fibers and actively pull on them, causing the cell to contract and form intercellular gaps in the endothelial monolayer. These events require the use of high energy phosphates which include ATP, produced through energetic metabolic pathways. However, how the signaling events that lead to both the activation of contractile machinery and metabolism to meet the ATP demand remains to be elucidated.

1.3 Energetic metabolism: overview and methods

Cell movement requires energy in the form of ATP which can be produced by cellular glycolysis or oxidative phosphorylation (OXPHOS). Glycolysis is a series of cytosolic reactions that generate pyruvate from glucose. Pyruvate can be imported into the mitochondria where it is converted to enter the tricarboxylic acid cycle (TCA) which then produces NADH and $FADH_2$ that can be used in the electron transport chain (ETC) to generate ATP through OXPHOS. Alternatively, pyruvate can be converted to lactate, regenerating NAD^+ which is consumed during the production of pyruvate from glucose (glycolysis). This pyruvate to lactate reaction allows cells to metabolize glucose, generate small amounts of ATP in a mitochondria-independent manner, and produce intermediates for biosynthetic pathways, all within the cytosol. OXPHOS generates much more ATP from the same input of glucose but requires molecular oxygen. Consequently, in a hypoxic environment, aerobic glycolysis will predominate as the functioning metabolic program. However, anaerobic glycolysis can also occur in the presence of oxygen depending on the cell's energetic demands.

The Warburg effect was first described in cancer cells where glycolysis is utilized despite the presence of oxygen, which has been shown to occur in healthy cells as well including endothelial cells and T cells (Koppenol, Bounds, and Dang 2011; De Bock et al. 2013; Ma et al. 2019). One reason a cell may preferentially utilize one pathway over another is that several intermediates are formed throughout glycolysis and TCA reactions that can be used in different biosynthetic pathways. Therefore, it is important to think of metabolism as not only a means of producing energy in the form of ATP, but also as a means to produce precursors for anabolic reactions. Mitochondria are often referred to as the "powerhouse" of the cell because of its ability to produce massive amounts of ATP in comparison to glycolysis. This is due to the structure of the mitochondria where membrane-encapsulation creates compartmentalized enzymes and substrates that speeds up consecutive reactions@. However, glycolysis occurs in the cytoplasm where many ATP-demanding reactions are necessary. Therefore, there is accumulating evidence that suggests the organization of glycolytic enzymes into "membrane-less organelles" within the cytosol that could produce ATP or other metabolites that then can be used locally, thus providing an efficient "metabolon". Evidence includes that 1) glycolytic enzymes including PFKFB3 (6-Phosphofructo-2-Kinase/Fructose-2,6-Biphosphatase 3) and PFK1 have been shown to be located near organelles or subcellular structures that require their usage (De Bock et al. 2013; Almacellas et al. 2019), 2) some glycolytic enzyme activity can be regulated by the binding of actin, thus turning on and off dependent on changes in subcellular structure (Hu et al. 2016; Park et al. 2020), and 3) some glycolytic enzymes are able to polymerize and have similar sequences to cytoskeletal proteins, indicating glycolytic enzymes may have served as a structural precursor to the cytoskeleton (Pollard and Goldman 2018; Norris et al. 2013). In order to add evidence that suggests

glycolysis is organized within the cell to provide a local pool of ATP, one would need a method that could measure glycolysis with subcellular spatial resolution which as of recently, did not exist.

The gold standard methods in metabolism involve bulk metabolism-interrogating technologies that can either measure metabolite flux (isotope tracing) or concentration (metabolomics) but not both (Jang, Chen, and Rabinowitz 2018). The Seahorse XF Analyzer measures the real-time extracellular acidification rate (ECAR) as a proxy for glycolysis, but is complicated to interpret (Mookerjee et al. 2015). Newer, promising mass spectrometry techniques can measure single cell metabolite concentration but cannot measure metabolic flux (L. Zhang and Vertes 2018). Furthermore, none of these techniques capture spatial information which is necessary for uncovering heterogeneity within a motile population. Genetically-encoded fluorescent metabolite sensing probes for analyzing cellular heterogeneity reap the advantages of live cell microscopy, where spatial and temporal information is retained but analysis remains a challenge (Morgan et al. 2016). Therefore, utilizing the rich temporal and spatial information inherent in imaging could be useful in determining the single-cell and subcellular rate of glycolysis in metabolically dynamic cells.

1.4 About this dissertation

In order to understand how cell motility is fueled, I examined (1) which energetic pathway was fueling motility, (2) whether or not this metabolic program correlated with heterogeneous motility, and (3) how these motile and metabolic differences are coordinated. Unfortunately, there are no current methods that could interrogate both motility and metabolism simultaneously and therefore I first developed a method to measure real-time single- and sub-cellular metabolism with spatial

resolution which is detailed in Chapter 2. In Chapter 3, I employ this method in order to determine if heterogeneous cell motility is related to the metabolic state of migratory and contractile endothelial cells. Building off the findings that motile cells are more glycolytic than stationary cells in Chapter 3, I explore the mechanism behind such rapid induction of glycolysis within contractile cells in Chapter 4. In Chapter 5, I look deeper within individual cells to see if the relationship between spatially heterogeneous motility and glycolysis is evident at the subcellular level, which could provide evidence for the existence of a glycolytic metabolon. Finally, I'll summarize the findings and future directions that emerged from this uncovered link between cell motility and energy production/consumption in Chapter 6. The data presented in this dissertation has been published and adapted from Wu & Harrison, et al. 2021 and Harrison & Wu et al. 2021. The extended protocol for performing the single-cell lactate production rate (LPR) can be found in Appendix I. Methods accompanying all data presented here appear in Appendix II. Altogether, I use my single- and subcellular LPR method to show that cells regulate glycolysis to meet local bioenergetic demand to ultimately fuel their physiological functions. These data not only further our understanding of cellular motility and energy regulation but will also, hopefully, lead to the development of therapeutics to treat or obviate complex diseases caused by aberrant cell migration.

CHAPTER TWO

LACTATE PRODUCTION RATE (LPR) IS A SINGLE-CELL MEASUREMENT OF GLYCOLYSIS

2.1 Introduction

Quantitative real-time measurements of single-cell metabolism is important in cell biology. Metabolic heterogeneity in endothelial cells dictates vascular activation and growth (D. Wu et al. 2017; Kim et al. 2017), during T-cell differentiation controls cell function in infection (Bantug et al. 2018; Karmaus et al. 2019), within tumors affects responses to anticancer treatments (Hensley et al. 2016), and among yeast cells results in distinct subpopulations in response to sudden changes of substrate availability (van Heerden et al. 2014), to name a few. The development of single-cell technologies have allowed for the understanding of heterogeneity within what we previously thought were homogenous populations and illuminated the importance of understanding how the non-uniformity within a population influences the aggregate (Z. Wang, Gerstein, and Snyder 2009; X. Tang et al. 2019). However, these technologies have largely focused at the transcriptomic or genetic level. Therefore, metabolic rate-dependent phenotypes have yet to be characterized at the single-cell level in real-time.

Cellular metabolism is inherently dynamic and heterogeneous, however current technologies including mass spectrometry and isotope tracing cannot simultaneously measure both metabolite flux and concentration while retaining spatial information (Jang, Chen, and Rabinowitz 2018; L. Zhang and Vertes 2018). Extracellular flux analysis measures the real-time extracellular acidification rate (ECAR), but ECAR is an indirect proxy for the glycolytic rate, making the

measurement difficult to interpret (Mookerjee et al. 2015). Spatiotemporal resolution can be achieved by recently developed genetically-encoded fluorescent metabolite sensors, but so far, analyses have not taken full advantage of the rich information inherent in images (Morgan et al. 2016).

To overcome the limitations of existing methods, we devised a single-cell metabolism quantification method to spatiotemporally monitor the real-time lactate concentration and glycolytic rate of individual cells (Figure 2.1). This method is demonstrated in two disparate cellular contexts: (1) human endothelial cells in response to HIF1α-dependent transcriptional upregulation of glycolysis and (2) T cells in response to artificial activation by PMA/ionomycin. To evaluate the lactate production rate (LPR) method's ability to distinguish authentic metabolically distinct subpopulations, I will measure LPR in endothelial cells in response to heterogeneous shear stress caused by differential flow.

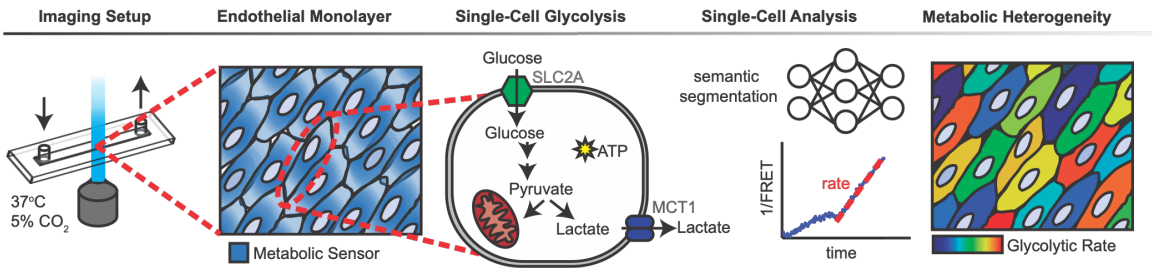


Figure 2.1: **Single-cell metabolism methodology.** Endothelial cells expressing FRET-based genetically encoded metabolite sensors including Laconic (San Martín et al. 2013) were plated into imaging chambers capable of fluid exchange with controlled temperature and CO_2. Once endothelial cells grew to form a monolayer, glycolytic metabolites including lactate were tracked to measure glycolysis using genetically encoded sensors. Within a cell, extracellular glucose taken up by glucose transporters (SLC2A/GLUT) is then converted to pyruvate and consumed by mitochondria or fermented into lactate and exported via MCT1. This utilization of glucose to form lactate via glycolysis will generate cytosolic ATP. Following imaging, deep learning enabled semantic segmentation was used for linking cells into a 1/FRET time series for quantification of intracellular lactate over time to reveal single-cell glycolysis which can be mapped back onto the endothelial cell population to reveal links between motility and metabolism.

2.2 Single-cell lactate production rate method and benchmarking

To study motile phenotypes of individual endothelial cells, I first devised a single-cell metabolism quantification method to monitor the lactate concentration and glycolytic rate of individual cells expressing a genetically encoded biosensor. Here we employ Laconic (San Martín et al. 2013), a Förster resonance energy transfer (FRET)-based lactate biosensor comprising of an mTFP/Venus FRET pair connected by a bacterial transcription factor LldR (Figure 2.2A). LldR binds lactate causing the FRET pair to change their intramolecular distance that leads to increased mTFP (acceptor)/Venus (donor) (or 1/FRET) signal. In this way, lactate concentrations are positively proportional to 1/FRET signals (Figure 2.2B). Laconic-expressing human endothelial cells were imaged, segmented using a semantic segmentation pipeline, and assembled into fluorescence traces under biochemical and/or biomechanical stimulations (Figure 2.1). This allowed us to monitor the terminal metabolite in glycolysis, lactate, in endothelial cells, thus directly revealing endothelial glycolytic reprogramming for energy production. Endothelial cells have interesting morphologies during cell elongation, migration, and contraction, which unfortunately cannot be fully captured by traditional cell segmentation methods. Therefore, a deep learning approach with U-nets (Ronneberger, Fischer, and Brox 2015; Van Valen et al. 2016) using custom code in MATLAB—written by my colleague, David Wu—was employed. This approach rapidly and reliably performed pixel-level classification of images and segmentation of single cells with Boundary F1 score (Csurka, Larlus, and Perronnin 2013) for identifying the cytoplasm > 90%, and class-specific cytoplasm accuracy, precision, recall, and Dice score > 80%, (Figure 2.2C, Table 1). Single-cell fluorescence following segmentation was highly correlated with ground-truth fluorescence (Figure 2.2D), indicating successful capture of individual cell signal and morphology.

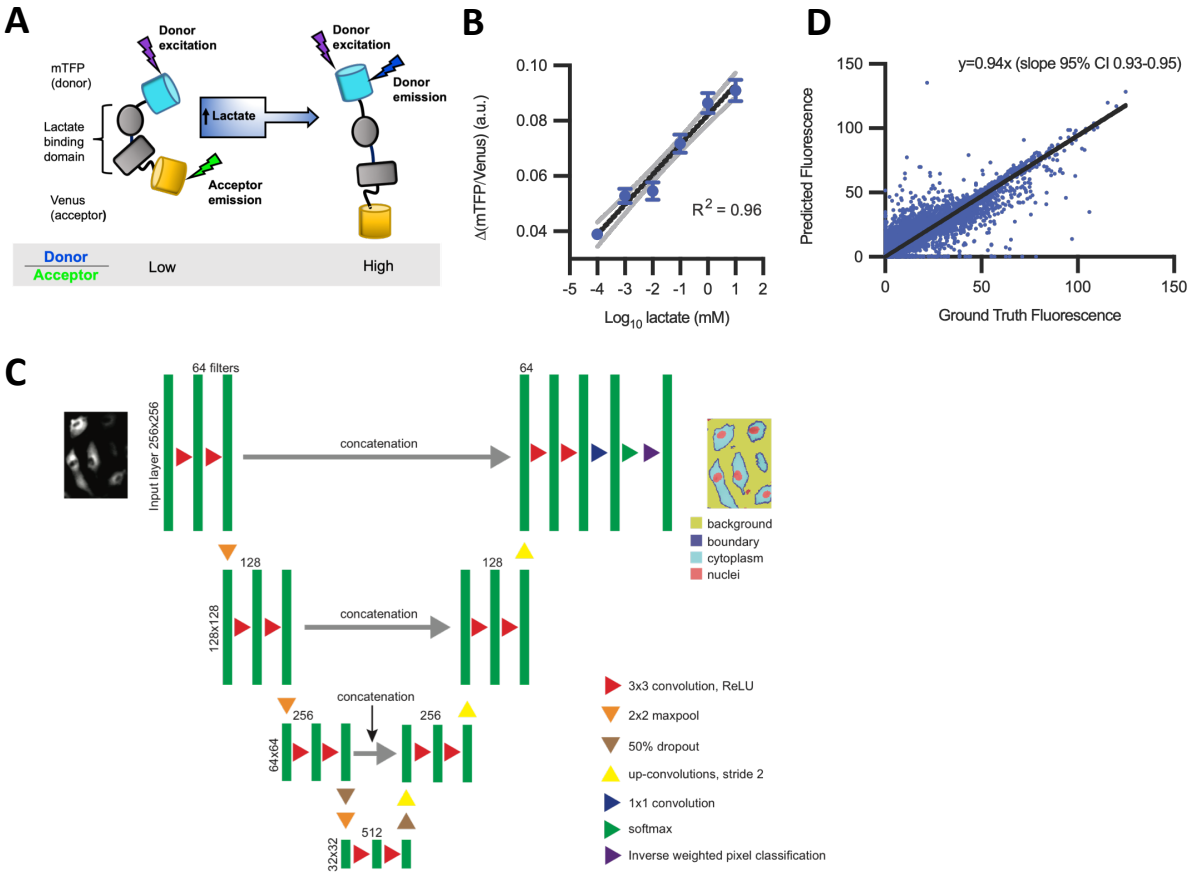


Figure 2.2: **Single-cell metabolic assay utilizes deep learning-enabled segmentation of a lactate-sensing probe.** (A) Laconic (San Martín et al. 2013) is comprised of a lactate binding domain flanked by two fluorophores capable of undergoing FRET. In the presence of low lactate, the donor (mTFP) and acceptor (Venus) fluorophores are in close enough proximity that the Donor/Acceptor emission ratio is low. In the presence of lactate, binding of lactate to the Lldr causes the FRET pair to increase in molecular distance, thus preventing FRET, resulting in increased donor/acceptor emission ratio. (B) mTFPVenus (or 1/FRET) change was linearly correlated over 6 orders of magnitude of log lactate (n = 287 cells; black line is semilog fit with $R^2 = 0.96$, gray dotted lines are 95% confidence interval); error bars are SEM. Standard deviation of regression coefficients for R^2 for (B) is 0.049. (C) Deep learning architecture for semantic segmentation, modified from Ronneberger et al (Ronneberger, Fischer, and Brox 2015). The U-Net consisted of a contracting path (encoder) and an expansive path (decoder). The contracting path consists of layers composed of two 3 × 3 convolutions, each followed by a rectified linear unit (ReLU) activation function. Each layer is followed by a 2 × 2 max pooling operation with a stride of two- which will double the number of feature channels being used. The convolutions start with 64 feature channels and 128 × 128 images and continue until they reach 512 channels and 16 × 16 images. In the expansive path, 2 × 2 up-convolutions (up sampling) of stride 2 to decrease by half the feature channels and increase the size of the image. The layers composed of 3 × 3 convolutions and ReLU are concatenated with the pair of layers in the contracting side, in order to reinclude the localization information. In the final layer, a 1 × 1 convolution layer is used to map the resulting 64-component feature channels vector to the 4 segmentation channels for background, boundary, cytoplasm, and nuclei. (D) Ground Truth Fluorescence vs. Predicted Fluorescence, as

Figure 2.2, continued: evaluated with deep-learning-enabled semantic segmentation. (n ~ 20,000 cells) Ground truth fluorescence was defined as signal inside the cell boundary.

Table 2.1: **Deep learning semantic segmentation evaluation metrics**

Matthew's Correlation Coefficient	0.85			
Global accuracy	0.84			
Class	*Background*	*Cytoplasm*	*Nuclei*	*Cell boundary*
Class specific accuracy	0.85	0.83	0.45	0.78
Standard deviation of accuracy	0.083	0.079	0.086	0.055
Boundary F1 score	0.96	0.95	0.75	0.94
Standard deviation of Boundary F1 score	0.05	0.047	0.079	0.071
Precision	0.85	0.83	0.45	0.78
Recall	0.97	0.84	0.31	0.38
Dice score	0.9	0.82	0.38	0.53
Standard Deviation of Dice Score	0.074	0.0659	0.064	0.064

To reliably measure and calibrate physiological levels of intracellular lactate and glycolysis using Laconic, intracellular lactate concentrations were controlled by permeabilizing human aortic endothelial cells (HAECs) and subjecting them to different concentrations of lactate. As shown in Figure 2.2B, the 1/FRET change is linear to 6 orders of magnitude of log lactate concentrations ($R^2 = 0.96$). However, lactate export is a dynamic process in live cells that is regulated by the concentration gradient between the extra- and intra-cellular compartments[10]. Thus, in order to measure the glycolytic rate of the cell, lactate export was blocked through inhibition of monocarboxylate transporter 1 (MCT1), the major lactate transporter in endothelial cells (Sonveaux et al. 2012). Upon MCT1 blockade by p-chloromercuribenzoic acid (pCMBA), there is a continuous increase of lactate in individual cells, the slope of which I defined as the lactate production rate (LPR) (Figure 2.3A), which reflects the overall glycolytic rate in a single endothelial cell. Furthermore, the single-cell LPR increased linearly, in agreement with bulk extracellular acidification measurements, as a function of extracellular glucose concentration

(Figure 2.3B). Employing a bootstrap algorithm simulating LPR, by drawing from ground truth fluorescence values and fitting slopes to the deep learning-measured fluorescence (Figure 2.2D), the absolute quantification error of LPR can be estimated to be 5% (see Methods, Figure 2.3C).

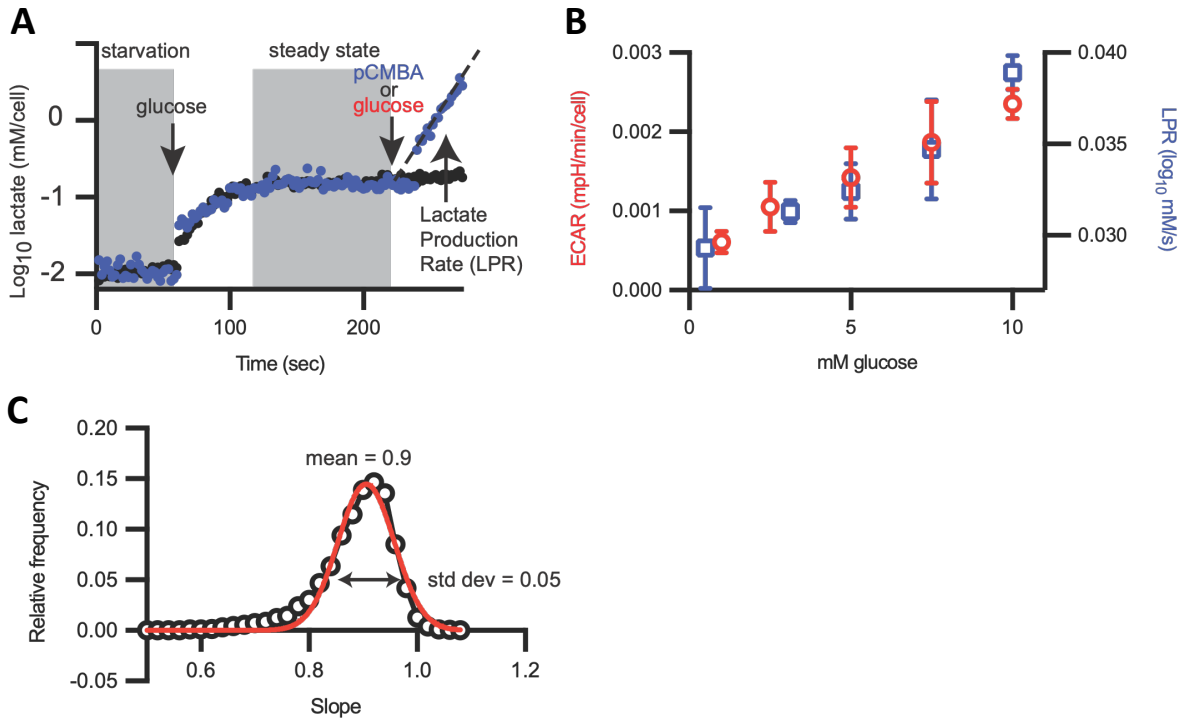


Figure 2.3: **The LPR assay reflects the glycolytic rate of individual cells.** (A) Single-cell trace of the LPR injection strategy. After starvation, glucose was injected and lactate levels rise within the cell before reaching a steady state where lactate production is masked by lactate export. MCT1 inhibitor pCMBA (blue dots) is then injected to monitor lactate accumulation. Without MCT1 blockade, the cellular lactate concentration remains at steady state (black dots). The slope (black dotted line, eye guide) of each cell is the lactate production rate (LPR), filtered for fitting with R^2 values ≥ 0.9. (B) Single-cell LPR and per cell ECAR vs extracellular glucose concentration (n = 7, 226, 43, 200, 206 cells for LPR left to right, n= 4, 3, 4, 3, 3 wells for ECAR left to right; error bars are SEM). (C) Frequency distribution of fluorescence slopes**.** Data from Figure 2.2D are randomly sampled 100 times and fitted to a line. This process is repeated 10,000 times and the distribution of fitted slopes was plotted (open black circles). The red line is a Gaussian fit with mean 0.9 and standard deviation of 0.05. Thus, the error in estimating slopes of fluorescence is approximately 0.05/0.9, or approximately 5%.

Consistently, the steady-state intracellular concentration of lactate measured by single-cell FRET was within the range estimated by bulk mass spectrometry (~0-1.6 mM) (Figure 2.4A). Corresponding to single-cell LPR, blockade of MCT1 with pCMBA (Halestrap 2013) also reduced

extracellular acidification in a bulk bioenergetics flux assay (Figure 2.4B). Additionally, intracellular lactate was able to be increased at the single-cell level with glucose or oligomycin stimulation, and inhibit lactate production by 2-deoxyglucose, like those used in an extracellular flux glycolysis stress test at the bulk level (Figure 2.4C).

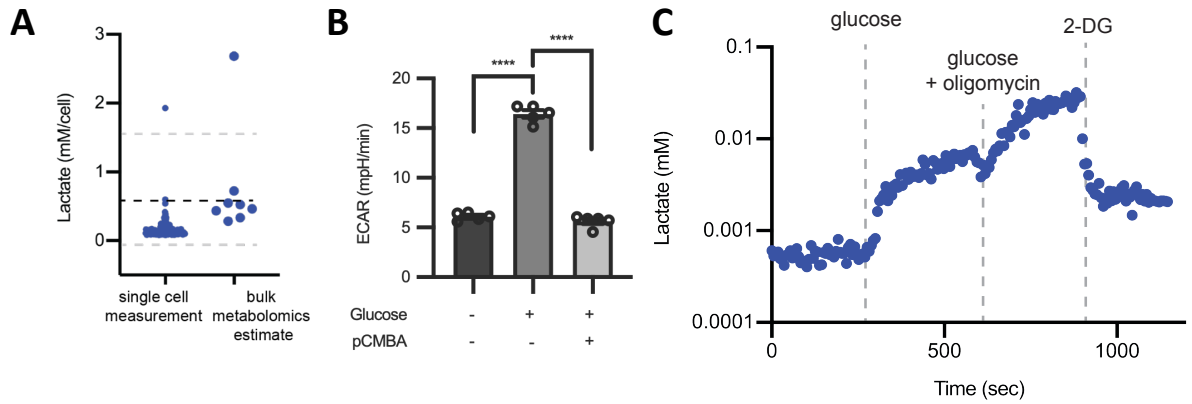


Figure 2.4: **Single-cell lactate levels mimic traditional metabolic measurements.** (A) Comparison of steady-state lactate levels (n = 167 cells) with metabolomics (n = 8). The dotted black line is the mean metabolomics (n = 8) estimate of intracellular lactate measured by mass spectrometry. Gray dotted lines are standard deviation. (B) Extracellular flux assay of HAECs treated with glucose then pCMBA (n = 5) using Seahorse; biological replicates, error bars are SEM, $p < 0.0001$ for both comparisons. (C) A single-cell glycolytic stress test using lactate FRET sensor. Cells were first starved in zero glucose buffer for 1 hour. Glucose addition increased intracellular lactate, which was further increased by adding oligomycin and glucose. Addition of 2-deoxyglucose (2-DG) blocked all glycolysis, causing intracellular lactate to drop. Statistical significance determined by one-way ANOVA followed by Bonferroni test (B).

2.3 Single-cell LPR of activated endothelial and T cells

To test the LPR's ability to distinguish heterogeneous glycolytic rates in cell populations, which is critical for differentiating subpopulations, I mimicked hypoxic conditions in endothelial cells by treating with dimethyloxalylglycine (DMOG). DMOG inhibits prolyl hydroxylase, thereby promoting the stabilization of transcription factor hypoxia inducible factor-1a (HIF-1a) which will increase expression of glycolytic genes(D. Wu et al. 2017). Single-cell LPR was elevated in DMOG-treated cells (Figure 2.5A), in agreement with an increase in ECAR measured in bulk

extracellular flux (Figure 2.5B). I next forced metabolic heterogeneity by mixing vehicle (DMSO)- or DMOG-treated cells that were previously labeled with either eBFP2 or mCherry fluorescent proteins, respectively (Figure 2.5C). By assessing the LPR of each cell and then de-mixing by color, this method distinguished authentic metabolic subpopulations.

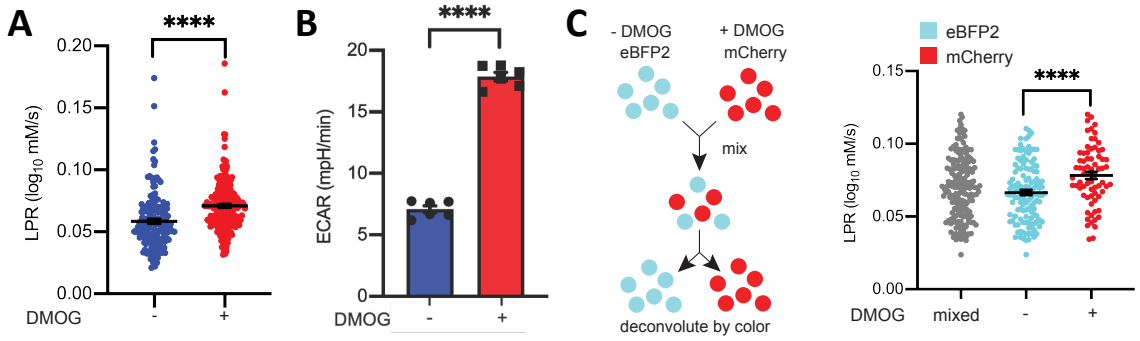


Figure 2.5: **LPR is able to distinguish metabolic subpopulations.** (A) LPR of vehicle DMSO ("-") or DMOG ("+") treated endothelial cells (n = 164 "-", 256 "+"; error bars were SEM, $p < 0.0001$). (B) Overnight treatment of endothelial cells with 500 μM DMOG increases ECAR measured by extracellular flux relative to DMSO-treated cells using Seahorse. (n = 11 combined biological and technical replicates for each condition; error bars are SEM, $p < 0.0001$). (C) eBFP2 or mCherry cells were treated with DMSO or DMOG, then mixed and imaged together; the LPR is then deconvoluted by color (n = 166 eBFP2, n = 79 mCherry; error bars are SEM, $p < 0.0001$). Error bars SEM. Statistical significance was determined by two-sided Welch's t-test.

In addition to lactate, we further employed other genetically encoded FRET-based sensors to measure key glycolytic metabolites including pyruvate (Martin and et al. 2014), glucose (Takanaga, Chaudhuri, and Frommer 2008), and ATP (Imamura 2009) to cross-validate these findings with DMOG (Figure 2.6A). Pyruvate production, glucose uptake, and ATP levels were all increased in DMOG-treated cells relative to DMSO control (Figure 2.6B-D). Monitoring other metabolites has the benefit of understanding bottlenecks or deficiencies at certain steps of glycolysis. However, pyruvate and glucose have alternative fates and ATP is not exclusively produced by glycolysis, whereas lactate is predominantly exported as waste or a signal. Therefore, lactate production is a more definitive surrogate for glycolysis. The similar increases in glucose, pyruvate, and ATP not only validated my primary results using the lactate sensor and LPR assay,

but also laid a solid foundation for the general application of this single-cell metabolism method across different metabolites.

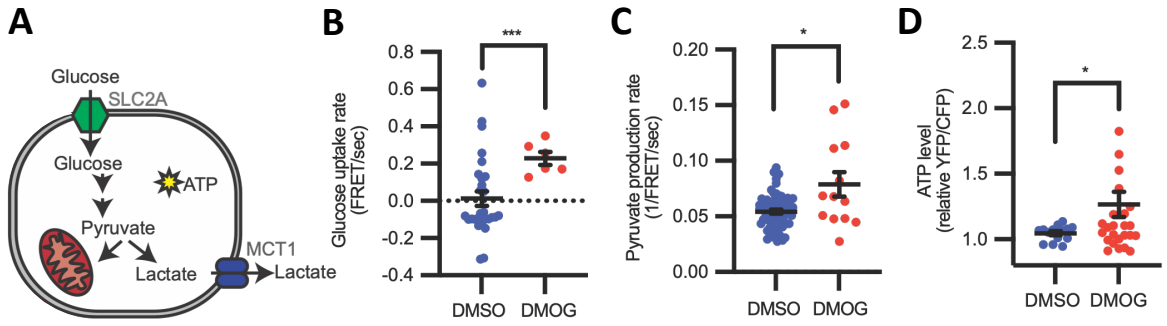


Figure 2.6: Additional glycolytic metabolites are measurably increased following DMOG stimulation. (A) Glucose is imported through SLC2A where it is metabolized through a series of reactions into pyruvate. Pyruvate will then be used by the mitochondria for oxidative phosphorylation or for fermentation into lactate, thus generating ATP. (B-D) Glucose uptake rate (B, n = 29, 6, p = 0.0005), Pyruvate production rate (C**,** n = 67, 13, p = 0.048), and ATP levels (D**,** n = 14, 29, p = 0.0323) in HAECs treated overnight with DMSO or DMOG measured using genetically encoded sensors. Error bar are SEM. Statistical significance determined by Welch's t-test.

Moreover, the broad application of this method to other cell types was demonstrated by detecting activation-induced metabolic reprogramming in T cells. The upregulation of glycolysis is required following T-cell recognition of antigen to mount an effective immune response (Menk et al. 2018). I first recapitulated that the FRET sensor quantifies the intracellular lactate concentrations in Jurkat T cells (Figure 2.7A, R^2=0.99). Next, Jurkat T cells were treated with phorbol myristate acetate (PMA)/ionomycin for 6 hours to stimulate protein kinase C, thereby initiating glycolysis (Windt et al. 2013, 8). Activation with PMA/ionomycin increased LPR (Figure 2.7B), consistent with bulk data measured by ECAR (Figure 2.7C), demonstrating the suitability of this single-cell metabolism method to measure single-cell metabolic rates in disparate cellular systems in response to diverse physiological stimuli.

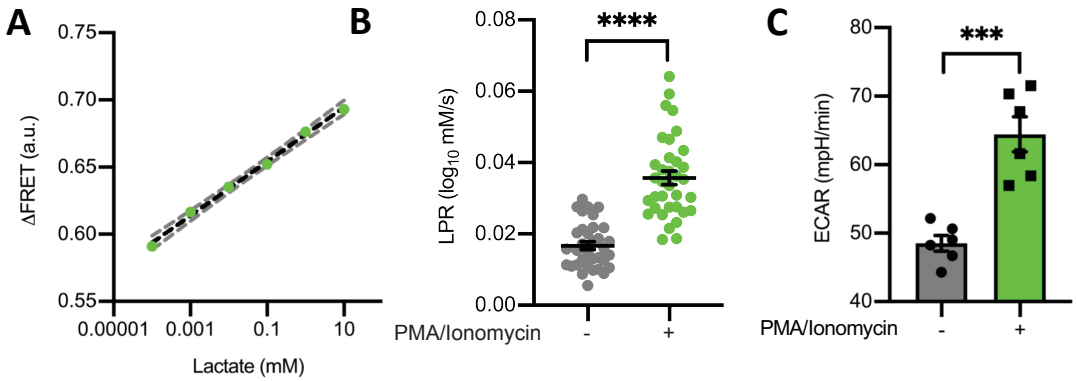


Figure 2.7: **Single-cell LPR can be extended to other metabolically dynamic cell types.** (A) Jurkat T cells clamped at 6 orders of magnitude of intracellular lactate concentrations compared to measured FRET values. Black line is semilog fit with RMSE 0.0545 and gray dotted lines are 95% confidence interval. (n = 5236, 5152, 5303, 5456, 5606, 5755 cells left to right; error bars are SEM.) (B) LPR of control or 6 hr PMA/Ionomycin stimulated Jurkat T cells (n = 34 control, 35 stimulated; error bars are SEM). (C) ECAR of PMA/Ionomycin stimulated Jurkat T cells (n = 6 both conditions). ****$p < 0.00005$ ***$p < 0.0005$. Statistical significance determined by Welch's t-test.

2.4 LPR distinguishes heterogeneous metabolic populations in response to flow

I next assessed single-cell glycolytic heterogeneity in a spatial context by exploiting the hemodynamic flow-dependent activation of endothelial cells, which are generally subject to different shear stresses depending on the local flow conditions in the vasculature (P. F. Davies 1995). Disturbed flow-induced cell activation leads to atherosclerosis at arterial branch points (P. F. Davies 1995), driven by low shear stress-induced endothelial glycolysis (D. Wu et al. 2017; Feng et al. 2017), and abrogated by high shear stress which is known to repress glycolysis (Doddaballapur et al. 2015) through reducing the expression of a key glycolytic enzyme, PFKFB3, in a transcription factor KLF2-dependent manner (Doddaballapur et al. 2015). However, the ability to study flow-induced metabolic changes has so far been limited to extracellular flux without spatial resolution[2].

Using a cone and plate device to generate spatially heterogeneous shear forces over microscopic distances (Figure 2.8A), I focused on an area at the flow boundary (indicated by endothelial elongation and alignment, Figure 2.8B) to determine force-dependent metabolic rates. As shown in Figure 2.8C, cells subjected to high shear stress had reduced LPR compared to those exposed to low shear stress, consistent with our lab's previously published bulk data as measured by ECAR(D. Wu et al. 2017). Metabolism was next linked to a morphological phenotype (flow-induced endothelial cell elongation) at the single-cell level. By analyzing endothelial cells exposed to shear stress, we found a direct association between force-induced cell morphology and glycolytic rate. By plotting the LPR and shear stress as a function of cell length, a negative correlation with LPR but a positive correlation with shear stress (Figure 2.8D) was found. To further demonstrate this relationship, these metrics were evaluated at higher (20×) magnification where I found cell length is strongly negatively correlated with LPR (Figure 2.8E,F). This result was partially caused by the presence of external forces (shear stress), which could change metabolic rates independent of cell morphology, though shorter cells within the high shear stress region exhibit higher LPR (Figure 2.8E).

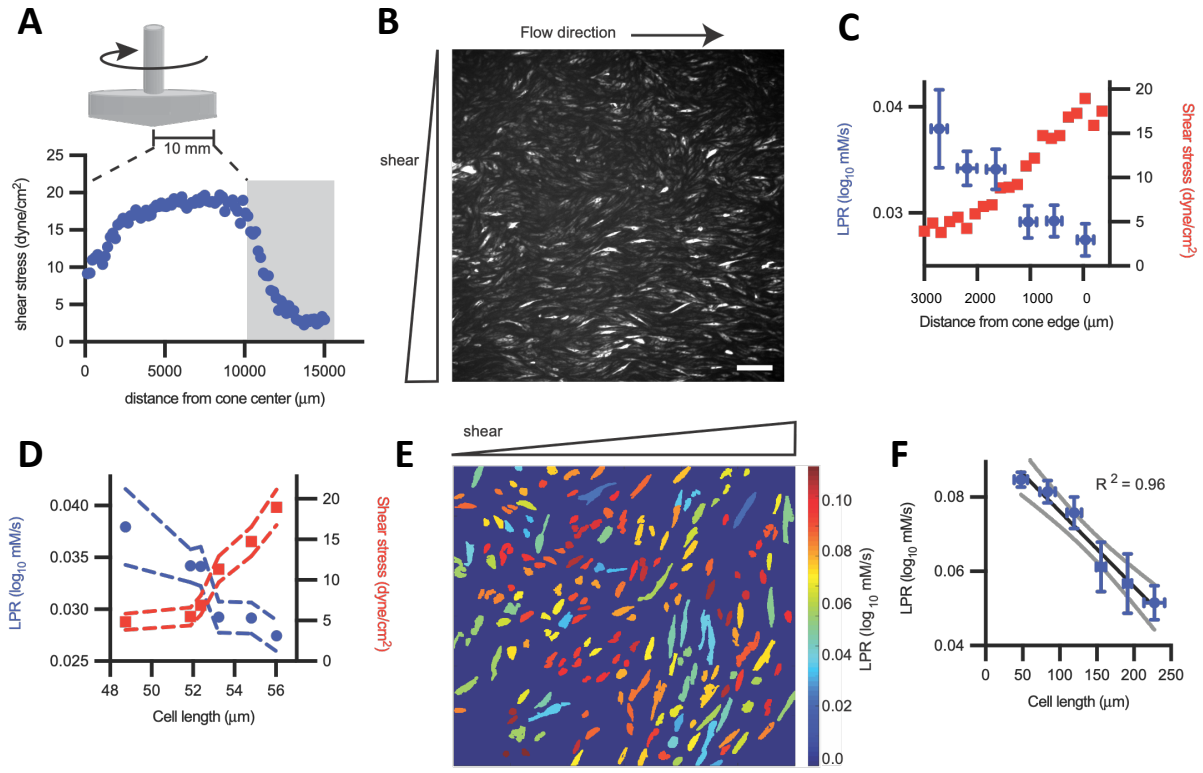


Figure 2.8: **Endothelial LPR in response to shear stress is heterogeneous.** (A) A cone and plate device was used to generate shear stress as measured by particle image velocimetry, with gray bar indicating area of interrogation. (B) The corresponding Laconic fluorescence image at the gray zone in (A). Scale bar = 165 μm (representative of n = 3 biological replicates). (C) LPR and shear stress vs distance from cone edge (n = 27, 47, 34, 34, 35, 33 left to right; error bars are SEM). (D) Replot of (C) with LPR and shear stress as a function of cell length, error bars are SEM. (E) The LPR of segmented endothelial cells subjected to flow (color from cold to hot indicated the increase of LPR in each cell). Scale bar = 44 μm. (F) Major axis cell length of endothelial cells E) plotted against measured LPR (cell number n = 103, 47, 18, 8, 8, 4 low to high cell length; error bars are SEM). Standard deviation of regression coefficients for R^2 for (F) is 0.074.

2.5 Conclusions and future directions

Though I measured cytosolic lactate levels to evaluate the level of glycolysis, lactate tracking could be used further to understand how glycolytic metabolites serve moonlighting functions. For example, lactate can be used in the nucleus for histone lactylation, thus epigenetically altering the cell state (D. Zhang et al. 2019). Additionally, we could track lactate production or export

specifically at the cell membrane to determine what proportion of lactate is being exported versus used internally. In order to study this further, I designed a nucleus-targeted Laconic through the addition of a nuclear localization sequence (NLS). In addition, I engineered the Laconic with the palmitoylation tag from GAP43 (Matsuda and Cepko 2007) or the myristoylation tag from Src (Rhee et al. 2006), which could drive member targeting. These sensors have been designed but not yet tested and would need extensive verifications and characterizations.

I developed an assay that can faithfully distinguish authentic metabolic subpopulations by tracking the terminal metabolite in glycolysis, lactate, using a genetically encoded FRET sensor. The ability to evaluate, in real-time, the glycolytic rate of individual cells will be necessary for evaluating the interesting but heterogeneous motile phenotypes of endothelial cells. The extended protocol for recapitulating the LPR assay in endothelial cells can be found in Appendix I. Though I found a strong correlation between cell shape and metabolic state, flow-induced changes in metabolism are largely caused by HIF1α-induced transcriptional changes. Therefore, in order to study the link between cell motility and glycolysis, I next investigated cell motility in real time in migrating and contractile cells.

CHAPTER THREE

ENDOTHELIAL CELL MOTILITIES ARE DRIVEN BY GLYCOLYSIS

3.1 Introduction

After finding that cells subjected to heterogeneous flow demonstrate differing cell morphologies and metabolic states, I sought to investigate endothelial cell motility further. Endothelial cells migrate during angiogenesis or wound closure. This process requires energy, involves dramatic changes in cell shape, and is dependent on RhoA/ROCK-1 remodeling of the actin cytoskeleton[5]. In typical wound assays, single-cell migrations are heterogeneous where some cells are motile while others remain stationary (Geerten P. van Nieuw Amerongen et al. 2003). Previously, it has been shown that endothelial cell migration requires glucose, whereas endothelial cell growth requires glutamine usage in oxidative phosphorylation (Kim et al. 2017; Diebold et al. 2019). However, it is not known whether individual migrating cells are more glycolytic than stationary cells, which could elucidate whether metabolism is a driver of heterogeneous cell migration in a disrupted cell monolayer.

Contraction is similarly energy demanding but whether glycolysis is used preferentially to fuel contractility is unknown. Additionally, these two processes have drastically different timescales: endothelial cells migrate over the course of hours but contraction happens within minutes. Though RhoA signaling has been shown to play a critical role in both motilities, whether or not RhoA coordinates glycolysis with cell morphological changes to induce mobility has yet to be tested. Therefore, I sought to measure single-cell LPR in migrating and contractile cells and further evaluate RhoA signaling in relation to glycolysis.

3.2 Migratory cells are more glycolytic than stationary cells

In order to evaluate whether glycolysis is important for migration, HAECs were given glucose which demonstrated that glucose utilization is important for migration. By treating with antimycin A, a mitochondrial complex III inhibitor, glucose consumption via the mitochondria was blocked and migration was not significantly altered, indicating glucose is necessary for migration but mitochondrial metabolism is dispensable for wound closure (Figure 3.1A). The results indicated that cell migration is driven by glycolysis. Consistently, HAECs treated with DMOG, which increases glycolytic capacity in a HIF-1a-dependent manner (Mole et al. 2003), enhanced migration and are able to close wounds faster than control (Figure 3.1B).

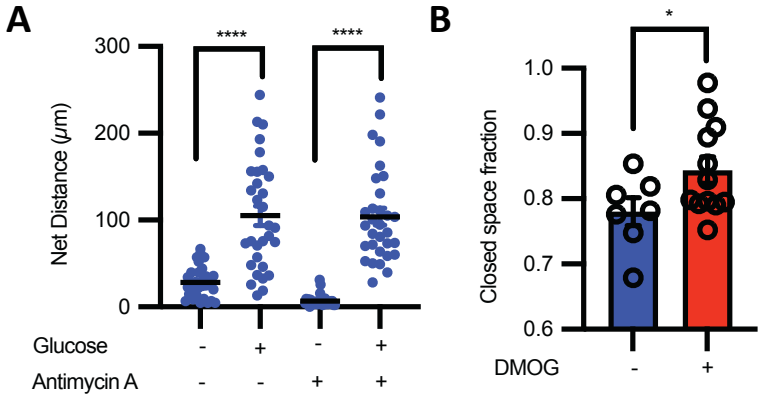


Figure 3.1: **Glucose consumption via glycolysis fuels migration.** (A) Migration distance of HAECs with or without glucose and with or without antimycin A (n = 31 cells each condition; error bars are SEM, $p < 0.0001$ for both pairs of conditions). (B) Migration scratch assay quantification with and without DMOG treatment (n = 7 and 12, respectively; error bars are SEM, $p = 0.0474$). Statistical significance was determined by two-sided Welch's t-test.

However, it remains unknown whether individual cells that migrated further were more glycolytic, as activation of HIF-1a by DMOG could turn on thousands of genes(D. Wu et al. 2017).

In order to elucidate whether cell glycolysis fuels individual cell motility, I applied single-cell metabolic assays to analyze migrating endothelial cells in a wound assay. By tracking individual cell migrations (Figure 3.2A) over the course of 12 hours, I confirmed that cells in the more stationary "tissue" migrated less than cells in the more migratory "wound", overall (Figure 3.2B). Migratory cells, defined as cells that traveled more than one cell length, were more glycolytic compared to stationary cells (Figure 3.2C). I further found that cell migration distance is positively correlated with cell glycolysis (Figure 3.2D), regardless of the final cell positions in the tissue or wound regions. These results suggest that the migration of endothelial cells is fueled by glycolysis, which is moreover proportional to work performed.

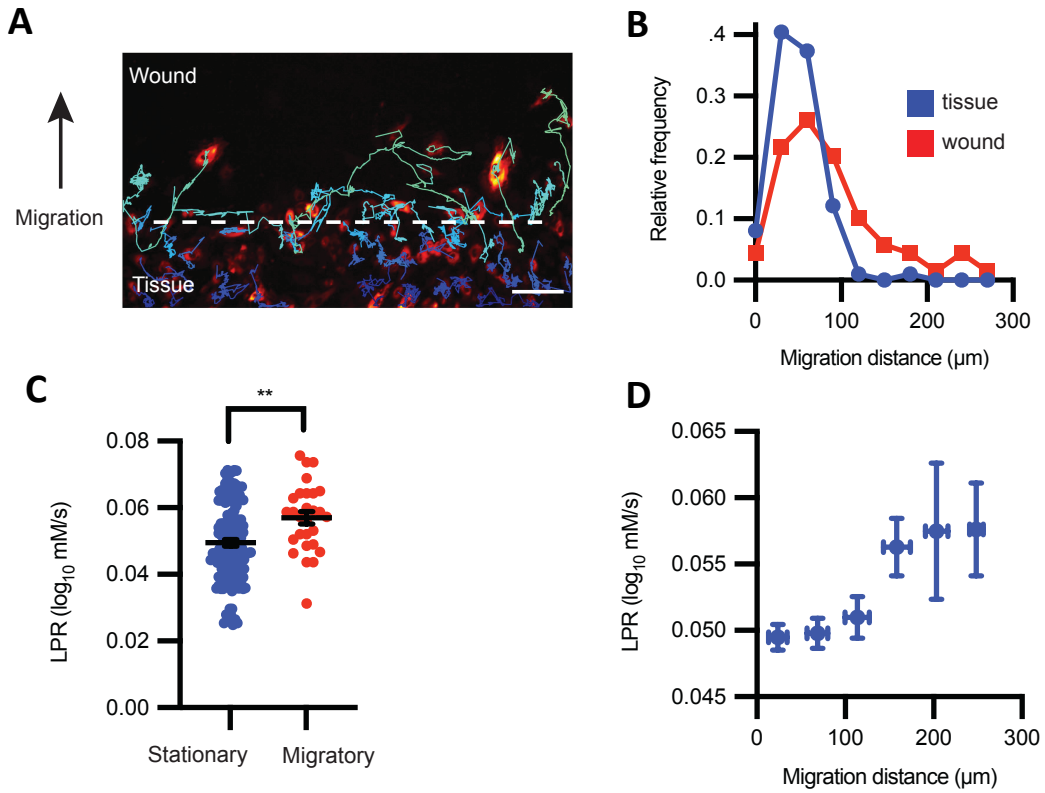


Figure 3.2: **Single-cell metabolism links migratory cell phenotypes to glycolytic states.** (A) Migrating endothelial cells (false color) were tracked for 48 hours following wound formation. Scale bar = 150 μm. (B) Frequency distribution of cell migration distance in the wound vs tissue.

Figure 3.2, continued: (C) The LPR of cells that migrated less than 50 μm compared to cells that migrated more than 200 μm (cell number n = 141 and 28, respectively; error bars are SEM, p = 0.0012). (D) The LPR change as a function of cell migrated distance (n = 114, 118, 42, 12, 8 from low to high migration distance; error bars are SEM). Statistical significance was determined by two-sided Welch's t-test.

3.3 RhoA stimulation triggers a glycolytic burst

Having shown that glycolysis fuels cell migration, I next quantified the glycolytic rate during cell contraction, a key motile endothelial process that occurs over a short timespan (minutes) and is thus independent of transcriptional control. Because GTPase RhoA activation is central to induce the contractile apparatus of endothelial cells within minutes (Fazal et al. 2009), I hypothesized that controlled RhoA agonism would induce a glycolytic burst to power cell contractions. RhoA activation or inactivation in HAECs was achieved by overexpressing constitutively active RhoA (RhoA-Q63L) or dominant negative RhoA (RhoA-T19N). As shown in Figure 3.3A, RhoA-Q63L (CA) increased single cell LPR compared to RhoA-T19N (DN). To remove possible batch effects, fluorescent protein eBFB2 was conjugated to RhoA-T19N and fluorescent protein mScarlet-i to RhoA-Q63L, followed by cell mixing and single-cell LPR measurements. Deconvolution by color showed significantly increased glycolysis in RhoA-activated (mScarlet-i positive) HAECs when compared to RhoA-inactivated (eBFP2 positive) cells (Figure 3.3B). Switching fluorescent labeling of RhoA-Q63L and RhoA-T19N had no effect on the results (Figure 3.3B).

Next, HAECs were treated with lysophosphatidic acid (LPA), a well-known RhoA agonist (G. P. van Nieuw Amerongen, Vermeer, and van Hinsbergh 2000) that induces contraction over minutes, which significantly increased single-cell LPR compared to untreated control (Figure 3.3C). Furthermore, treatment with thrombin, another serine protease that rapidly stimulates RhoA and subsequently RhoA kinase-1 (ROCK-1)(G. P. van Nieuw Amerongen et al. 2000) to produce contractions and barrier breakdown, significantly increased LPR in 7 minutes, which was largely

abrogated by the treatment of a specific ROCK-1 inhibitor, Y27632 (Figure 3.3D). Consistently, glucose uptake and ATP levels were also elevated shortly after thrombin treatment (Figure 3.3E). Thus, activation of GTPase RhoA causatively drives intracellular lactate production and glycolysis in single endothelial cells.

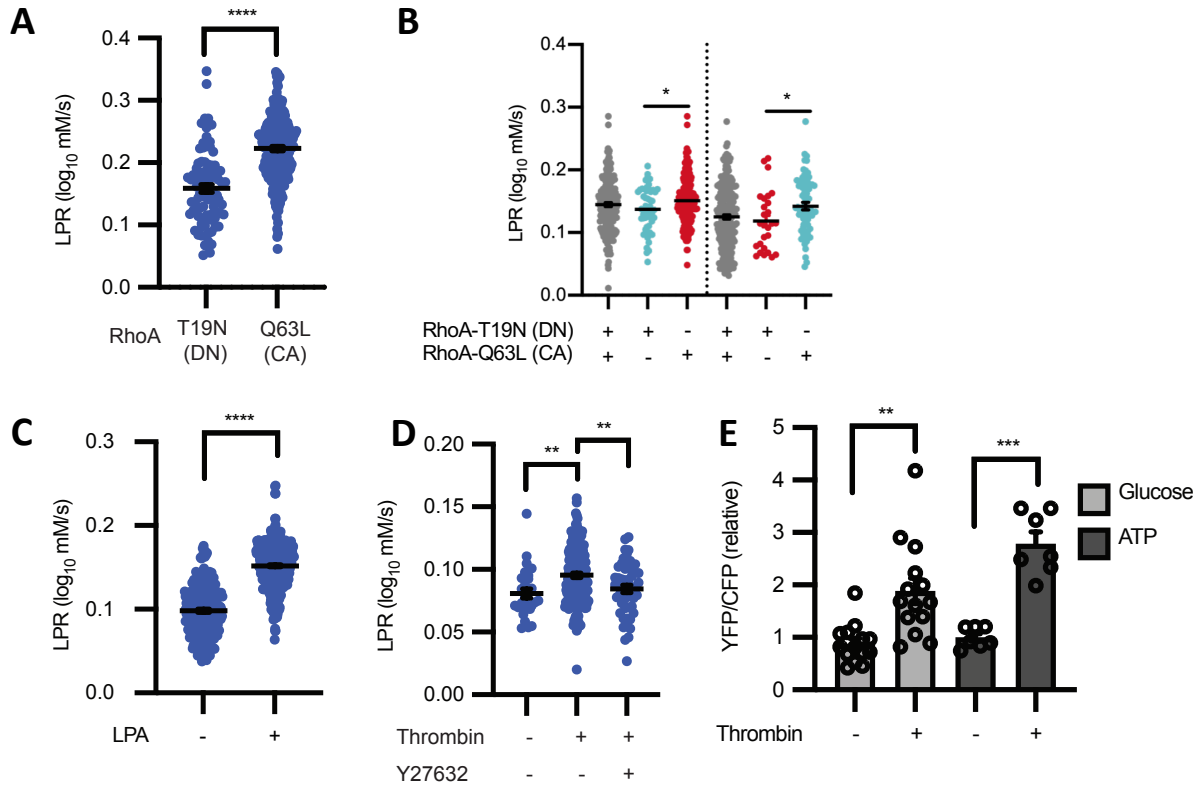


Figure 3.3: **Single-cell imaging of lactate production reveals RhoA drives endothelial cell glycolysis.** (A) LPR of HAECs transfected with either RhoA-T19N (dominant negative "DN" form) or RhoA-Q63L (constitutively active "CA" form). (n = 91, 250 respectively, $p < 0.0001$). (B) RhoA-Q63L transfected ECs have increased LPR compared to those transfected with RhoA-T19N after unmixing by color (n = 245, 52, 174, 235, 68, 27 from left to right, $p < 0.05$ for both). (C) LPR of HAECs treated with control (DMSO "-") or 10 μM of lysophosphatidic acid for 30 min. (n = 244 and 423 respectively, $p < 0.0001$). (D) Thrombin induced LPR (n = 171) compared to control (n = 28, $p = 0.0028$) which is suppressed with Y27632 (n = 51, $p = 0.0042$). (E) Glucose and ATP levels before and after treatment with thrombin measured by FRET (n = 14 cells glucose, $p = 0.0012$; n = 7 cells ATP, $p = 0.0001$). Error bars are SEM. Statistical significance was determined by two-sided Welch's t-test. Statistical significance determined by two-sided Welch's t-test (A-C, E) or by one-way ANOVA followed by Bonferroni test (D).

3.4 RhoA activates contractile machinery through glycolysis

Because the activity of RhoA-dependent kinases requires ATP and I found increased glycolysis and ATP levels within RhoA-stimulated cells, I hypothesized that the downstream functions of RhoA/ROCK-1 are dependent on glycolysis. RhoA/ROCK-1 activation causes rapid phosphorylation of cofilin (CFL) which enacts reorganization of the actin cytoskeleton from cortical actin to stress fibers (Fazal et al. 2009; Blanchoin et al. 2014). RhoA/ROCK-1 activity also causes phosphorylation of myosin light chain (MLC) which actively pulls on stress fibers, causing cell contractions and intercellular gaps in endothelial monolayers (failure of the endothelial paracellular barrier) as well as the reduction in monolayer impedance(Goddard and Iruela-Arispe 2013; Mehta and Malik 2006; Vandenbroucke et al. 2008). Phosphorylation of CFL and MLC occurs in 2-30 minutes with relaxation of the cell to its basal state after 1 hour as the stimulus is depleted (G. P. van Nieuw Amerongen et al. 2000; 2000). To test this hypothesis, we used hexokinase inhibitor 2-deoxyglucose (2-DG) to block glycolysis. Indeed, 2DG significantly reduced basal CFL and MLC phosphorylation in HAECs and moreover, completely blocked thrombin-induced phosphorylation of CFL and MLC (Figure 3.4A), demonstrating that RhoA/ROCK1 downstream effects are dependent on active glycolysis. Consistently, the degree of contraction, or change in monolayer impedance, was dependent on the concentration of glucose in the media, as measured by transendothelial electrical resistance (TEER) (Figure 3.4B). Concordantly, depleting endothelial glycolysis with 2-DG also prevented thrombin-induced barrier failure by TEER (Figure 3.4C). Furthermore, inhibition of ROCK-1 with Y27632 followed by thrombin treatment phenocopied pre-treatment with 2DG (Figure 3.4D). These data collectively demonstrated that RhoA/ROCK1-dependent glycolysis is required for the contractile machinery of endothelial cells.

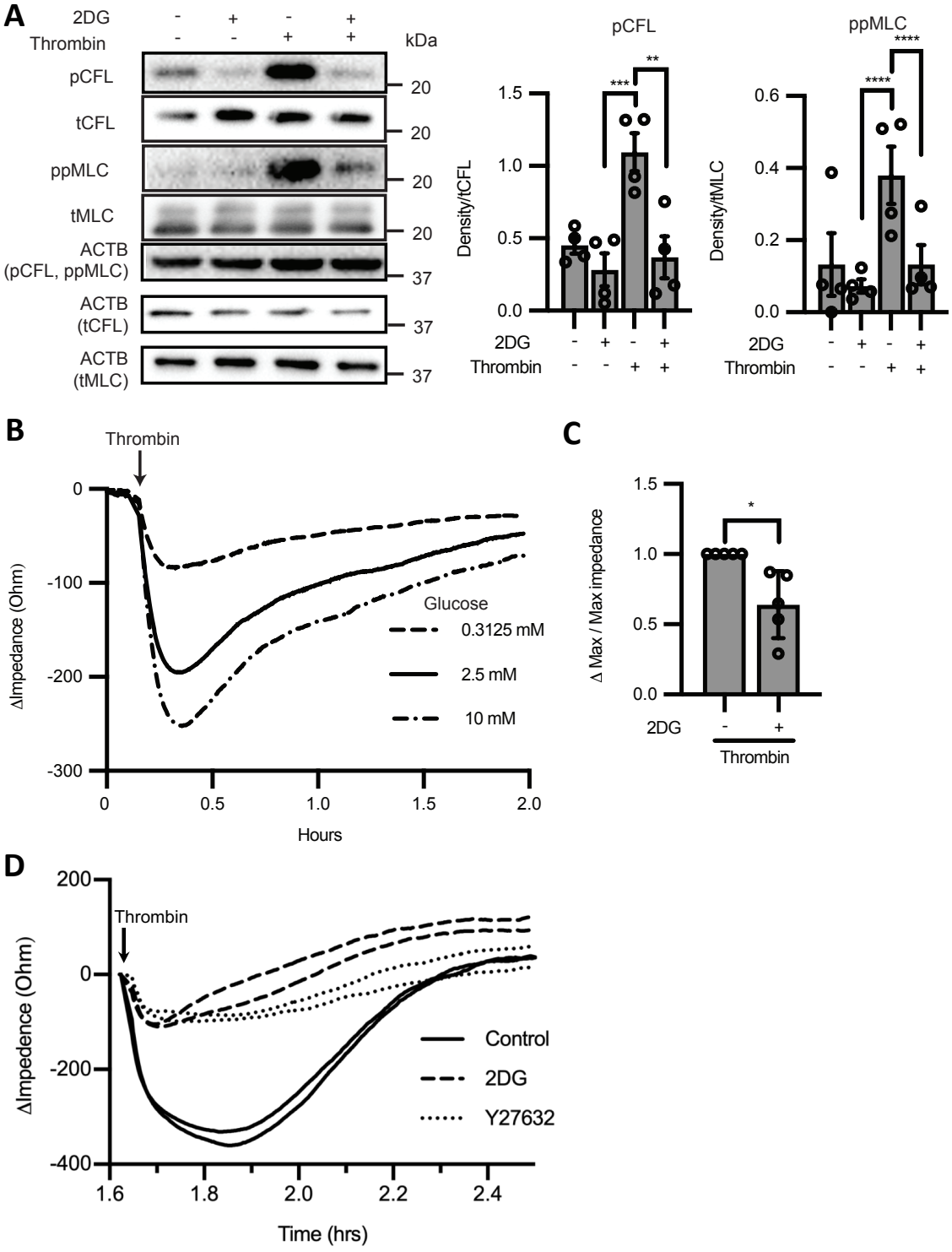


Figure 3.4: **Glycolysis is necessary for activation of contractile machinery.** (A) Western blot of 2DG pre-treatment in the presence or absence of thrombin and phosphorylation of cofilin and MLC (n = 4 biological replicates. For pCFL, p = 0.008 for thrombin vs. 2DG and p = 0.0038 for thrombin vs thrombin + 2DG. For ppMLC, p < 0.0001 for both thrombin vs 2DG and thrombin vs thrombin + 2DG). Loading control (ACTB) each protein denoted in parentheticals. (B) TEER trace of

Figure 3.4, continued: HAECs after thrombin treatment in different extracellular glucose conditions. (C) Inhibition of hexokinase with 2-DG reduces thrombin-induced permeability as measured by TEER (n = 5 each; biological replicates, p = 0.0283). (D) TEER measurement of HAECs after thrombin treatment, either pre-treated with Y27632 or 2DG compared to control (no Y27632 or 2DG). Statistical significance determined by two-sided Welch's t-test (C) or by one-way ANOVA followed by Bonferroni test (A). All error bars are SEM.

3.5 Conclusions and future directions

Using the single-cell LPR method, I found that migratory cells are more glycolytic than stationary cells and that the rate of glycolysis correlates with the speed of the migrating cell. Interestingly, inhibition of the mitochondria via antimycin A slightly but not significantly decreased cell wound closure. I attribute this to the fact that mitochondria support cell proliferation which occurs in conjunction with migration during wound healing. Though I found that cells in the tissue migrated less and were less glycolytic than cells in the wound, it would be interesting to evaluate how contact inhibition affects glycolysis. Perhaps the number of nearest neighbors or Notch signaling relates to the glycolytic rate. However, this would need to be further evaluated for confirmation.

Inducing contraction through RhoA agonism stimulates glycolysis which fuels the contractile machinery, specifically by providing high energy phosphates for the phosphorylation of CFL and MLC. However, actin polymerization additionally requires ATP and is necessary for extension of cell edges during migration. Therefore, it would be useful to evaluate how the increase in glycolysis could be serving actin remodeling beyond cofilin and myosin light chain. There is a period of active contraction and then relaxation following RhoA agonism where the endothelial cells extend to form an impenetrable monolayer. Whether glycolysis could be serving both contraction and re-stabilization of the barrier would require further investigation. Nevertheless, my findings that that RhoA triggers glycolysis and that the degree of contraction scales with

glucose concentration drove me to uncover the molecular mechanism by which RhoA stimulation could trigger glycolysis on a short timescale (minutes.)

CHAPTER FOUR

SLC2A3/GLUT3 CONTRIBUTES TO RHOA-TRIGGERED ENDOTHELIAL CELL CONTRACTION

4.1 Introduction

I next determined the molecular mechanisms by which RhoA induces glycolysis to stimulate endothelial contraction. Since the increase in glycolysis occurs over a short timespan (measured at 7 minutes) following RhoA activation (Figure 3.3C,D), uptake of glucose is increased following thrombin treatment (Figure 3.3E), and availability of glucose determines the degree of downstream phosphorylation and contraction (Figure 3.4C), it would be reasonable to investigate glucose uptake as potential step in RhoA-induced glycolysis.

4.2 Comparative SLC2A3/GLUT3 and SLC2A1/GLUT1 studies in endothelial cell contraction

Previous studies have shown that SLC2A1/GLUT1 is a major glucose transporter in endothelial cells: SLC2A1 contributes to the basal endothelial glycolytic capacity in the blood brain barrier (M. Tang et al. 2017) and pulmonary vasculature (Fessel et al. 2012), as well as to increased glycolysis stimulated by chronic (hours) exposure to hypoxia and disturbed flow in large arteries (D. Wu et al. 2017) I therefore first tested the role of SLC2A1. Unexpectedly, small interfering RNA (siRNA)-mediated SLC2A1 knockdown did not reduce thrombin-induced phosphorylation of CFL and MLC in HAECs (Figure 4.1A). At the same time, qRT-PCR analysis identified that SLC2A3 is the most abundant glucose transporter transcript in HAECs (Figure 4.1B). Our data showed that SLC2A3 knockdown reduced basal phosphorylation of CFL and MLC and

significantly abrogated thrombin-induced phosphorylation of CFL and MLC with three separate siRNAs (Figure 4.1C-E).

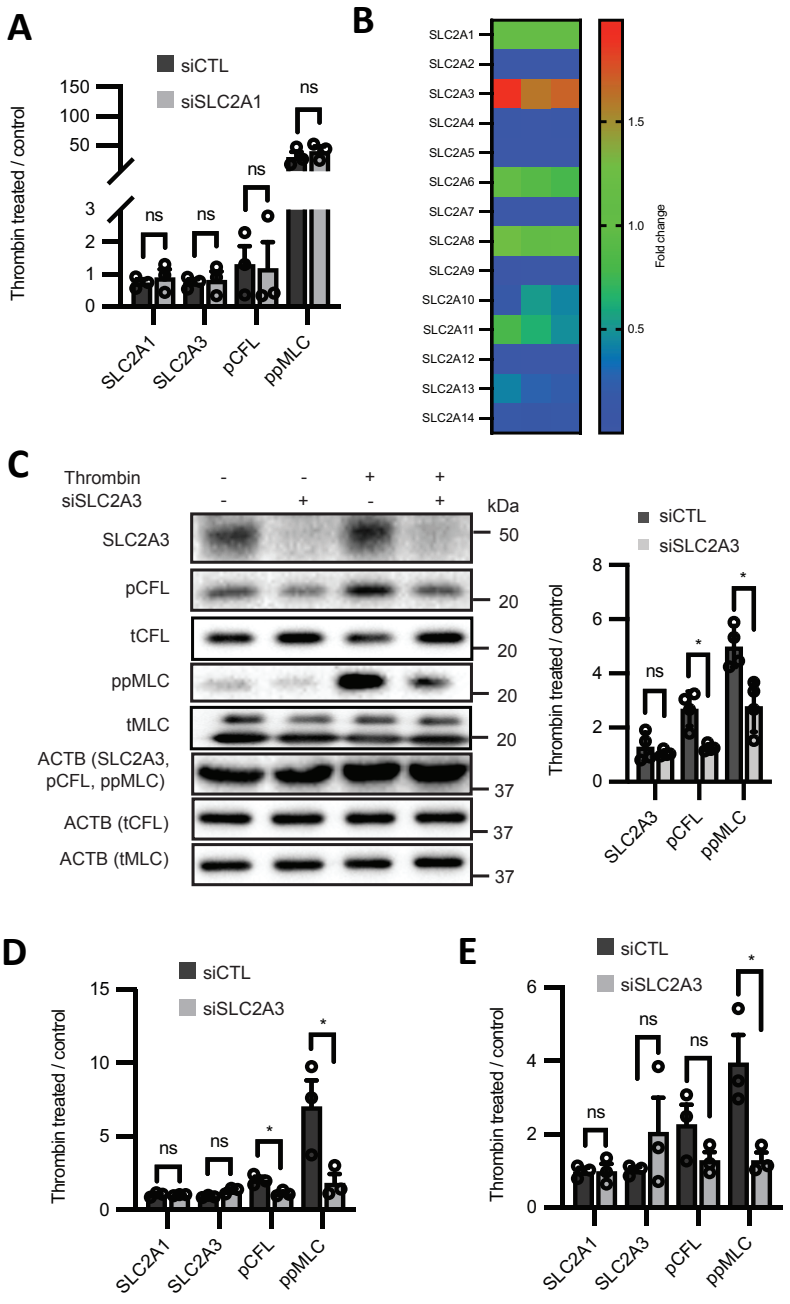


Figure 4.1: **Inhibition of SLC2A3 but not SLC2A1 reduces RhoA activation of contractile machinery** (A) Western blot of SLC2A1, SLC2A3, phospho-cofilin and phospho-MLC in the presence or absence of siRNA targeted towards SLC2A1 and thrombin treatment (n = 3 biological replicates). Loading control for each protein is ACTB unless specifically denoted in parentheticals. (B) Heatmap of glucose transporter expression relative to SLC2A1 in HAECs captured by qRT-

Figure 4.1, continued: PCR (n = 3 biological replicates) (C) Western blot of phospho-cofilin and phospho-MLC in the presence or absence of siRNA targeted towards SLC2A3 and thrombin treatment (n = 4 all; biological replicates, p = 0.0140 for pCFL and p = 0.0233 for ppMLC). Loading control (ACTB) for each protein denoted in parentheticals. (D-E) Western blot of SLC2A1, SLC2A3, phospho-cofilin and phospho-MLC in the presence or absence of two distinct siRNA (separate from the one used in C) targeted towards SLC2A3 and thrombin treatment (n = 3 biological replicates. For D, p = 0.0190 for pCFL and 0.0490 for ppMLC. For E, p = 0.0272 for ppMLC.). Loading control for each protein is ACTB unless specifically denoted in parentheticals. Statistical significance determined by multiple unpaired two-tailed t-test with multiple comparisons adjustment by the Holm-Šídák method. All error bars are SEM.

Although SLC2A3 knockdown had no effect on basal endothelial glycolysis, it largely abolished the thrombin-induced glycolytic burst, as detected by single-cell LPR (Figure 4.2A). In direct comparison, SLC2A1 knockdown led to a measurable decrease in LPR after thrombin stimulation but this decrease was far less than that of SLC2A3 knockdown (Figure 4.2B). Consistently, knockdown of SLC2A3 abrogated the thrombin-induced increase in glucose uptake (Figure 4.2C). The increase in ATP levels that follow RhoA stimulation were similarly diminished by SLC2A3 knockdown (Figure 4.2D).

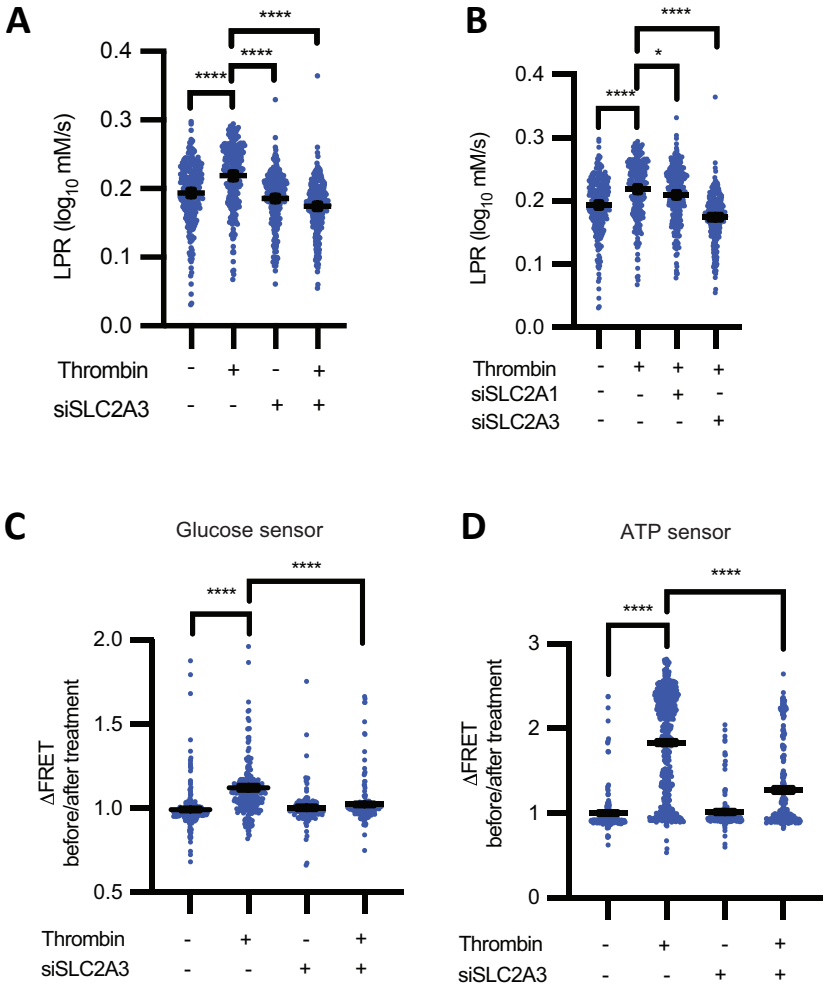


Figure 4.2: **SLC2A3 knockdown prevents RhoA-induced glycolysis.** (A) LPR of siRNA targeted towards SLC2A3 or control with and without thrombin treatment (n = 277, 263, 275, 278 from left to right, $p < 0.0001$ for all comparisons). (B) Single-cell LPR of HAECs treated with thrombin in the presence of siSLC2A1 or siSLC2A3 (n = 277 for thrombin vs. control, n = 281 for thrombin vs. thrombin + siSLC2A1, and n = 278 for thrombin vs. thrombin + siSLC2A3, $p < 0.0001$, $p = 0.0384$, $p < 0.0001$, respectively.). (C) Glucose and (D) ATP levels in single-cells in the presence or absence of SLC2A3 knockdown and thrombin treatment (C: n = 248, 248, 108, 190 from left to right, $p < 0.0001$ for all comparisons; D: 190, 598, 150, 287 from left to right, $p < 0.0001$ for all comparisons). Statistical significance determined by one-way ANOVA followed by Bonferroni test. All error bars are SEM.

4.3 GLUT3 is translocated to the membrane during contraction to upregulate glycolysis

Because the glycolytic burst could not be attributed to SLC2A3 transcriptional regulation given the acute response (measured within 7 minutes), it is possible that SLC2A3 is regulated post-transcriptionally by RhoA/ROCK-1. In highly-glycolytic platelets where SLC2A3 is enriched, thrombin (a potent platelet activator) can stimulate SLC2A3 plasma membrane translocation (Sorbara et al. 1997). To test this hypothesis in endothelial cells, immunofluorescence imaging of SLC2A3 in thrombin-treated HAECs was performed. Using total internal reflection fluorescence (TIRF) microscopy, which selectively illuminates membrane fluorophores close to the cover slip (within ~100 nm)(Sasmal et al. 2016; 2020), Significantly increased intensity of SLC2A3 in granules near the plasma membrane of single HAECs were detected following thrombin stimulation; such accumulation of SLC2A3 were abrogated by ROCK inhibitor Y27632, further suggesting the involvement of Rho/ROCK signaling pathway (Figure 4.3A). In agreement with the SLC2A3-dependent glycolytic burst and phosphorylation of CFL and MLC, thrombin-induced endothelial contraction was significantly abrogated by SLC2A3 knockdown, demonstrated by increased monolayer impedance by TEER (Figure 4.3B,C) and reduced intercellular gap size (gap size index, Figure 4.3D-E), although the number of gaps was unchanged (gap index, Figure 4.3D,F)(Fraccaroli et al. 2015).

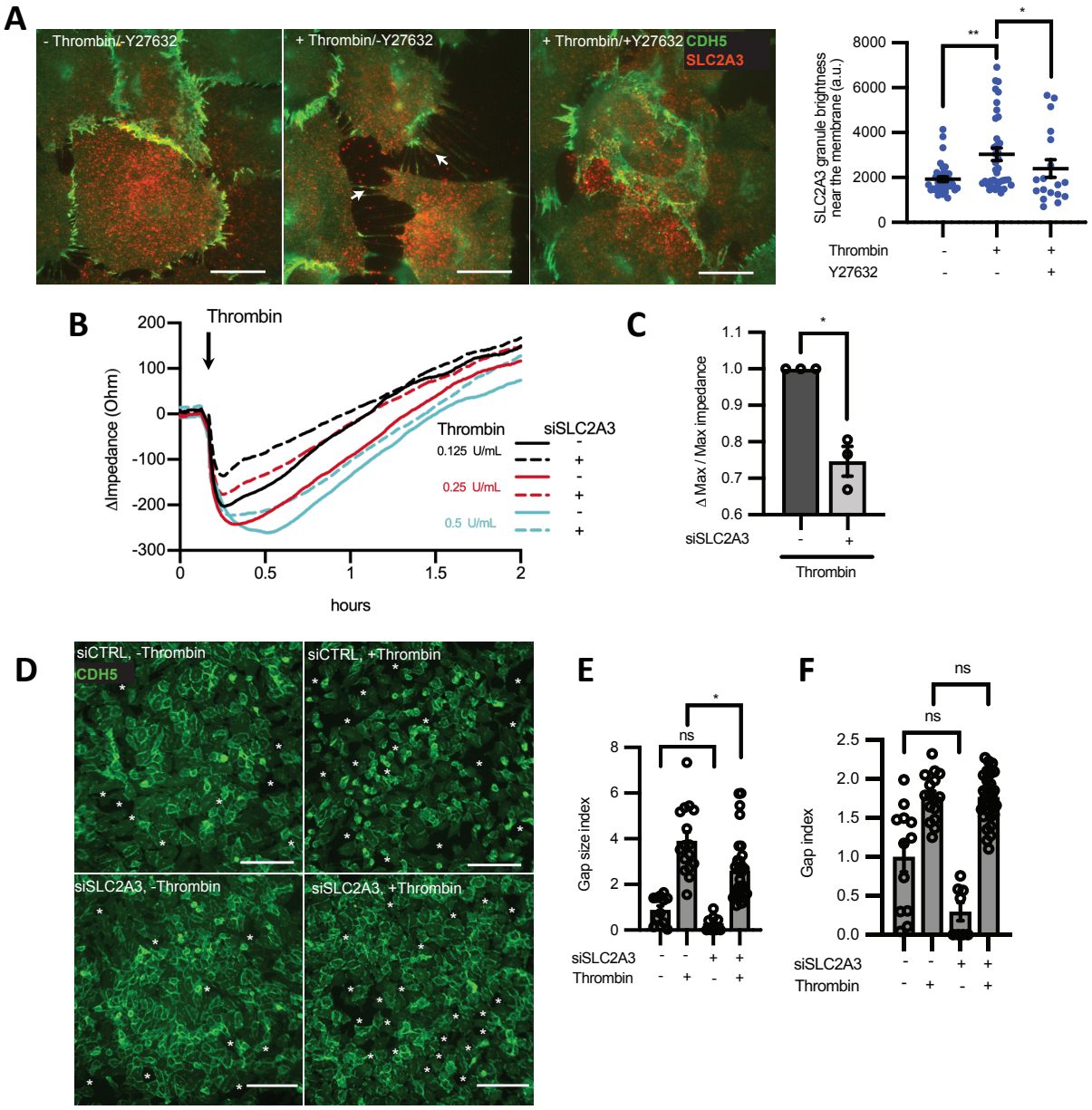


Figure 4.3: **SLC2A3 localization to the membrane contributes to contraction.** (A) Representative immunofluorescence of membrane markers CDH5 and SLC2A3 in thrombin treated cells causes SLC2A3 granule localization to membrane spikes, which is inhibited by Y27632, by TIRF microscopy. Scale bar = 5 μm. (A, right) Quantification of SLC2A3 granule brightness near the membrane of (A, left) (a.u. = arbitrary units, n = 36, 36, 17 images from left to right. p = 0.003 for thrombin vs. control, and p = 0.0499 for thrombin vs thrombin + Y27632). (B) TEER traces from variable doses of thrombin treatment in the presence of siSLC2A3. (C) TEER measurement of thrombin-induced permeability changes in the presence or absence of siRNA targeted towards SLC2A3 (n = 4; biological replicates, p = 0.0248). (D) Representative immunofluorescence of CDH5 and intercellular gaps in HAECs treated with control or siRNA targeted towards SLC2A3 followed by thrombin treatment. (E-F) Quantification of gap size (E) and number of gaps (F) from (D) (n = 12, 16, 8, 32 images from left to right, p = 0.0184). Scale

Figure 4.3, continued: bar = 150 μm. Statistical significance determined by two-sided Welch's t-test (C) or by one-way ANOVA followed by Bonferroni test (A, E-F). All error bars are SEM.

Reasoning that SLC2A3 knockdown creates a bottleneck at glucose uptake for glycolysis-dependent contraction, I investigated whether bypassing this glucose uptake limitation could partially rescue contraction. Indeed, increasing the amount of extracellular glucose increased gap size and gap number, which was blunted by SLC2A3 knockdown (Figure 4.4A). Treatment with oligomycin, which will divert all intracellular glucose to be utilized via glycolysis, partially rescued contraction (gap size index), but did not change gap number, under SLC2A3 knockdown (Figure 4.4B).

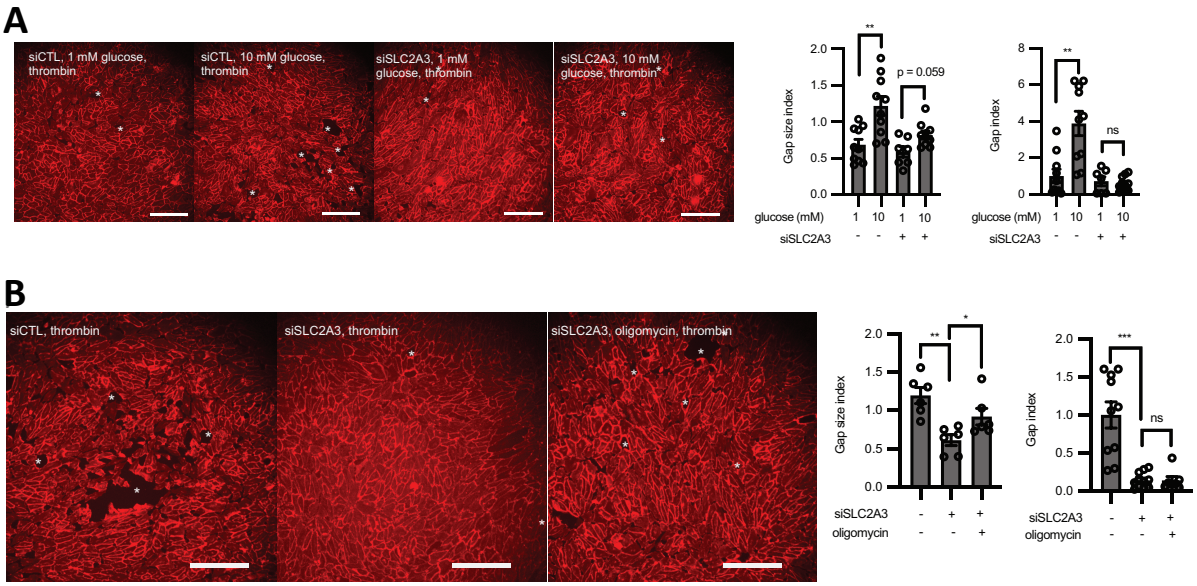


Figure 4.4: **Contraction under SLC2A3 knockdown is partially rescued by increasing glucose availability.** (A-B) Representative images of HAECs treated with siSLC2A3 or control with varying concentrations of glucose (A) or with oligomycin (B) in the presence of thrombin. Red color is CDH5. Gap size index and gap index quantification of images (A), n = 10, 10, 7, 8 from left to right, p = 0.022 for gap size index and p = 0.0019; (B), n = 6 for gap size index, p = 0.0013 for siSLC2A3 vs control and p = 0.040 for siSLC2A3 vs. siSLC2A3 + oligomycin, and n = 10, 11, 7 from left to right for gap index, p < 0.0001). White stars highlight gaps in the monolayer. Scale bars = 250 μm. Statistical significance determined by one-way ANOVA followed by Bonferroni test. All error bars are SEM.

4.4 SLC2A3/GLUT3-dependent contraction is conserved across multiple endothelial cell types

In order to understand the generalizability of SLC2A3/GLUT3's role in aiding RhoA-stimulated contraction in endothelial cells, I tested whether SLC2A3 knockdown would affect the contractile machinery and ultimately, contraction, in two other human endothelial cells: human umbilical endothelial cells (HUVECs) and human lung microvascular cells (HMVEC). Indeed, thrombin-induced phosphorylation of CFL and MLC were also significantly abrogated by SLC2A3 knockdown in HUVECs (Figure 4.5A) and HMVECs (Figure 4.5B). Thrombin-induced HUVEC contractions (as measured by cell size, Figure 4.5C) and HMVEC contractions (as measured by intercellular gaps, Figure 4.5D) were also significantly reduced by SLC2A3, indicating this pathway is conserved across multiple endothelial cell types.

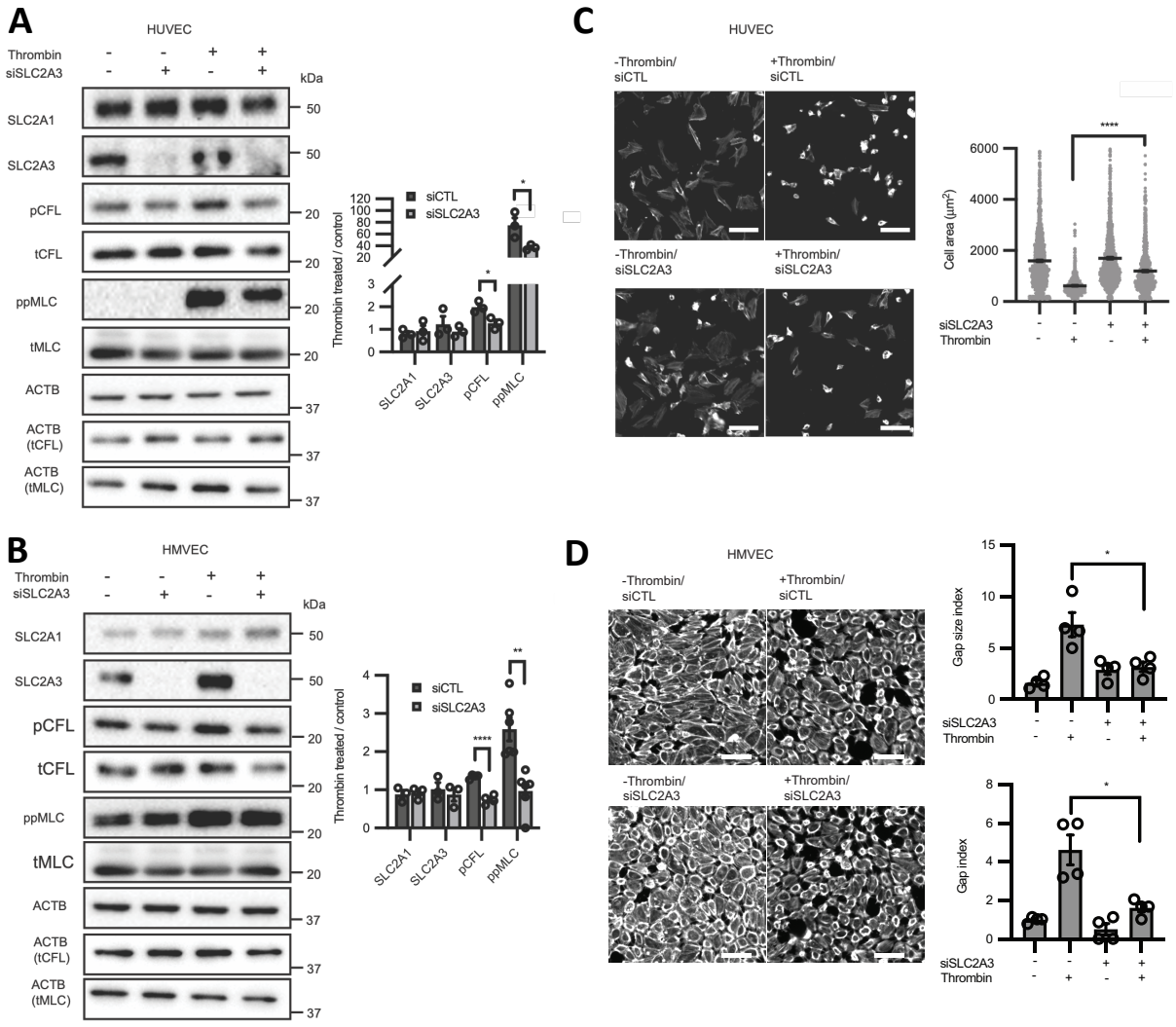


Figure 4.5: **SLC2A3 inhibition abrogates thrombin-induced phosphorylation of CFL and MLC and contraction across multiple endothelial cell types.** (A-B) Western blot analysis of glucose transporter expression, phosphorylated CFL, and phosphorylated MLC, in human umbilical vein endothelial cells (HUVEC, A, n = 3; biological replicates, p = 0.0257 for pCFL and 0.0414 or ppMLC) and human microvascular endothelial cells (HMVEC, B, n = 3 for SLC2A1, SLC2A3, n = 4 for CFL and n = 5 for MLC; biological replicates, p < 0.001 for pCFL and p = 0.0014 for ppMLC). Loading control for each protein is ACTB unless specifically denoted in parentheticals. (C) Representative images and cell size of contractile HUVECs subjected to thrombin stimulation in the absence or presence of SLC2A3 knockdown. (n = 1375, 1279, 760, 1162 from left to right, p < 0.0001) (D) Representative images, gap size index, and gap index of contractile HMVECs subjected to thrombin stimulation in the absence or presence of SLC2A3 knockdown. Representative images are phalloidin. (n = 4 biological replicates, p = 0.0171 for gap size index and p = 0.0262 for gap index) Statistical significance determined by two-sided Welch's t-test. All error bars are SEM.

4.5 SLC2A3/GLUT3 endothelial overexpression *in vivo* increases vascular leak

The functional role of SLC2A3 in endothelial glycolysis and contraction is largely unknown but after finding its contribution to contraction in multiple human endothelial cell types, I wanted to evaluate conservation of this pathway *in vivo* utilizing mice. In order to explore the *in vivo* relevance of SLC2A3 in barrier regulation, the expression profile of Slc2a1 and Slc2a3 in primary endothelial cells from different organs in mice must be evaluated. Gene Expression Omnibus datasets (GEOD) were downloaded from EndoDB, a database of curated endothelial transcriptomics datasets (Khan and et al. 2019) . As shown in Figure 4.6A, Slc2a3 has expression levels similar to Slc2a1 across multiple organs (normalized to Slc2a1). With the help of my colleagues who are trained in animal studies, we next overexpressed SLC2A3 under the endothelial-specific CDH5/VE-cadherin promoter and evaluated vascular leak in mouse aortas. Mouse aortas, because to their intrinsic curvature, exhibit RhoA activation due to hemodynamic shear forces (Yao et al. 2018). We employed a delivery system which integrates polyethylenimine (PEI) nanoparticles and plasmids with the endothelial-specific CDH5/VE-cadherin promoter. Intravenous injection of CDH5-driven, mScarlet-i-expressing plasmids resulted in mScarlet-i fluorescence in arterial endothelium, highlighted by co-localization with ve-cadh (which marks endothelium) adjacent to the lumen, but not the underlying media and adventitia (yellow signal in merge panel, Figure 4.6B), demonstrating endothelial-specific overexpression in mice. The same approach using CDH5-driven, SLC2A3-expresssing plasmids led to SLC2A3 overexpression in aortic endothelium but not in the media and adventitia in mice, measured by quantitative real-time PCR (Figure 4.6C).

To demonstrate functional relevance of SLC2A3, mice were injected with PEI nanoparticles containing CDH5-SLC2A3 or CDH5-Ctrl plasmids 24 hours prior to sacrifice. 1

hour prior to sacrifice, Evans blue dye was injected retro-orbitally. Evans blue dye binds to albumin and transits the endothelial barrier in a paracellular fashion under conditions of diminished tight and adherent junctions and quantitatively measures the leakiness of mouse aortas(Yao et al. 2018). Endothelial overexpression of SLC2A3 results in leakiness of aorta as quantified by Evans blue spectroscopy (OD 620), normalized to aorta weight after dye extraction (Figure 4.6D). This experiment suggests that SLC2A3 regulates the endothelial barrier *in vivo*.

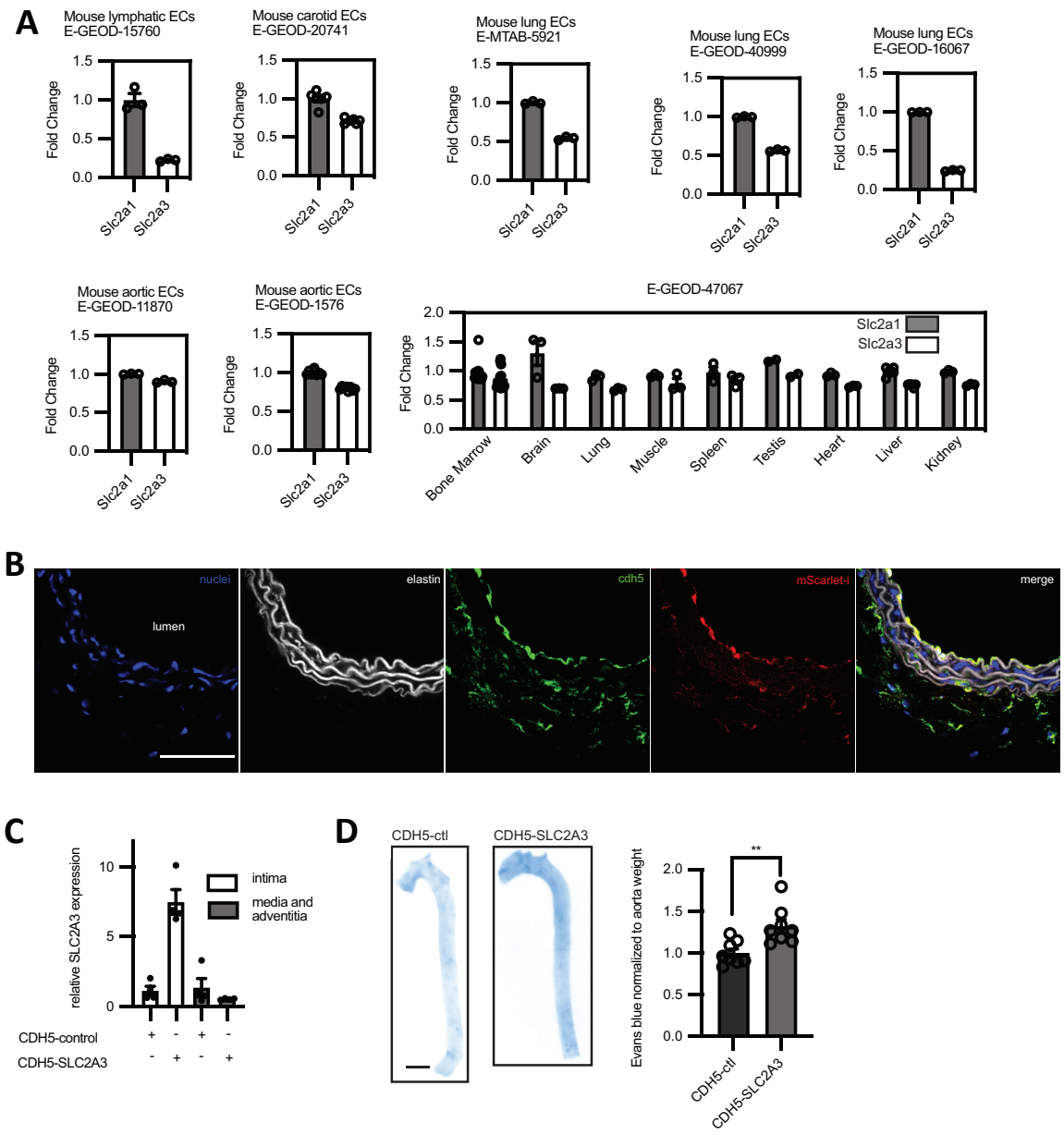


Figure 4.6: ***In vivo* overexpression of SLC2A3 increases vascular leak.** (A) GEO datasets of primary endothelial mouse cells comparing Slc2a1 and Slc2a3 from different organs. Fold change indicates that data are normalized to Slc2a1 except for E-GEOD-47067 which was normalized to average of Slc2a1 in all tissues. Only controls of experiments in the GEO datasets were used in these analyses. (n = 3 independent biological replicates for each condition for E-GEOD-15760; n = 6 independent biological replicates for each condition for E-GEOD-20741; n = 3 independent biological replicates for each condition for E-MTAB-5921; n = 3 independent biological replicates for each condition for E-GEOD-40999; n = 3 independent biological replicates for each condition for E-GEOD-11870; n = 3 independent biological replicates for each condition for E-GEOD-1576; n = 3 independent biological replicates for condition in each organ for E-GEOD-47067) (B) Immunofluorescence of an arterial section demonstrating enhanced mScarlet-i fluorescence (red) colocalized with ve-cadh (green) which marks the endothelium next to the lumen (yellow, merge)

Figure 4.6, continued: (Scale bar, 500 mm, representative of n = 4 mice). (C) SLC2A3 expressing plasmid uses an endothelial specific CDH5 promoter. SLC2A3 is detected by qRT-PCR of the intima of the mouse aorta, and far less than in the media and adventitia. (n = 4 independent biological replicates, p = 0.0030) (D) Evans blue (OD 620 nm) quantification of mouse aortas, normalized by weight. (n = 8 independent biological replicates for each condition, p = 0.0050). Statistical significance was determined by two-sided Welch's t-test. All error bars are SEM.

4.6 Conclusions and future directions

I found that RhoA is able to induce a glycolytic burst to power contractions through the translocation of SLC2A3 and that this mechanism is conserved across multiple endothelial cell types. How exactly RhoA is able to induce this translocation of SLC2A3 remains to be explored, especially since it most likely involves the recruitment of the cytoskeleton. Future experiments could include evaluating if SLC2A3 exists in submembrane vesicles or caveolae. Interestingly, SLC2A3 has been reported to have a higher K_D for glucose in comparison to SLC2A1 and therefore could serve as a mechanism for rapid glucose uptake in the face of energetic demand. Additionally, we were able to test the *in vivo* relevance of SLC2A3 in barrier leak by overexpression but future experiments could make use of mouse models of lung injury by LPS and further genetic perturbation, ideally by knocking out GLUT3. This would give us more insight into the contribution of SLC2A3 to vascular disease, which I expand upon in section 6.4. Collectively, these results demonstrated the importance of SLC2A3 on fueling RhoA/ROCK-1 signaling through downstream phosphorylation and its importance in both *in vitro* and *in vivo* barrier function.

CHAPTER FIVE

RHOA COORDINATES SUBCELLULAR GLYCOLYSIS WITH CYTOSKELETAL REMODELLING

5.1 Introduction

At the single-cell level, I found that morphology is linked to glycolysis (Chapter 2), heterogeneous glycolysis fuels migration (Chapter 3), and that RhoA activation induces endothelial glycolysis and contraction within minutes partially through SLC2A3 (Chapter 4). Contraction requires drastic changes in morphology that is heterogeneous even at the subcellular scale: some edges contract or displace whereas some edges remain stationary. Additionally, the idea that glycolysis is organized subcellularly as a "metabolon" either through glycolytic enzyme location or activation is accumulating evidence. Given this evidence, I hypothesized that glycolysis would be non-uniform at the subcellular scale in order to selectively power structural changes where necessary. Therefore, I sought to evaluate how glycolysis relates to morphological changes within individual endothelial cells with subcellular resolution.

5.2 Subcellular LPR is spatially heterogeneous and overlaps with actin remodeling

Reasoning that actin remodeling is dependent on high-energy phosphates, localized changes in actin could potentially be correlated with glycolytic activity at the subcellular spatial scale. To test this hypothesis, I again stimulated actin remodeling with a RhoA agonist thrombin. By co-expressing Laconic and Lifeact-RFP (Riedl et al. 2008) (an F-actin label) in endothelial cells, I measured LPR and actin remodeling in single endothelial cells with subcellular resolution at 40× magnification (Figure 5.1A). Lifeact signal increases and shimmers at the edges of thrombin-induced contracting cells, indicating active actin remodeling. In order to visualize actin

remodeling, the maximum intensity projection of the difference in Lifeact signals in the 7 minutes following thrombin addition prior to performing the LPR assay was computed (Figure 5.1A, difference image). The LPR image was captured by performing pixel-wise calculation of the slope of the FRET signal after addition of pCMBA (Figure 5.1A, LPR). As shown in the merged image, the LPR signal was spatially correlated with the Lifeact difference image (Figure 5.1A, "LPR+difference" and "LPR+difference+nucleus"). The Lifeact difference and LPR images together demonstrated enhancement of signals on the contracting edge and center of the cell. To quantify the correlation, the degree of overlap using Manders' overlap coefficient (MOC) and Pearson's correlation coefficient (PCC) were calculated. MOC can be useful in determining colocalization of signals but PCC takes into account variance, meaning two signals' ability to scale with each other. Thrombin-stimulated cells showed much higher levels of correlation between subcellular LPR and Lifeact than those of non-stimulated cells (Figure 5.1B). This correlation was diminished by inhibition of ROCK (Y-27632), actin polymerization (Latrunculin B), and myosin II (para-amino-Blebbistatin) (Figure 5.1B). After showing that disruption of the cytoskeleton destroys the overlap of signals, I reasoned that inhibiting RhoA-stimulated glycolysis by inhibiting SLC2A3 should have a similar effect. Indeed, SLC2A3 knockdown reduced the correlation between Lifeact difference and LPR after thrombin treatment, indicating RhoA-dependent SLC2A3 activity is necessary for the co-occurrence of subcellular glycolysis and actin remodeling (Figure 5.1C).

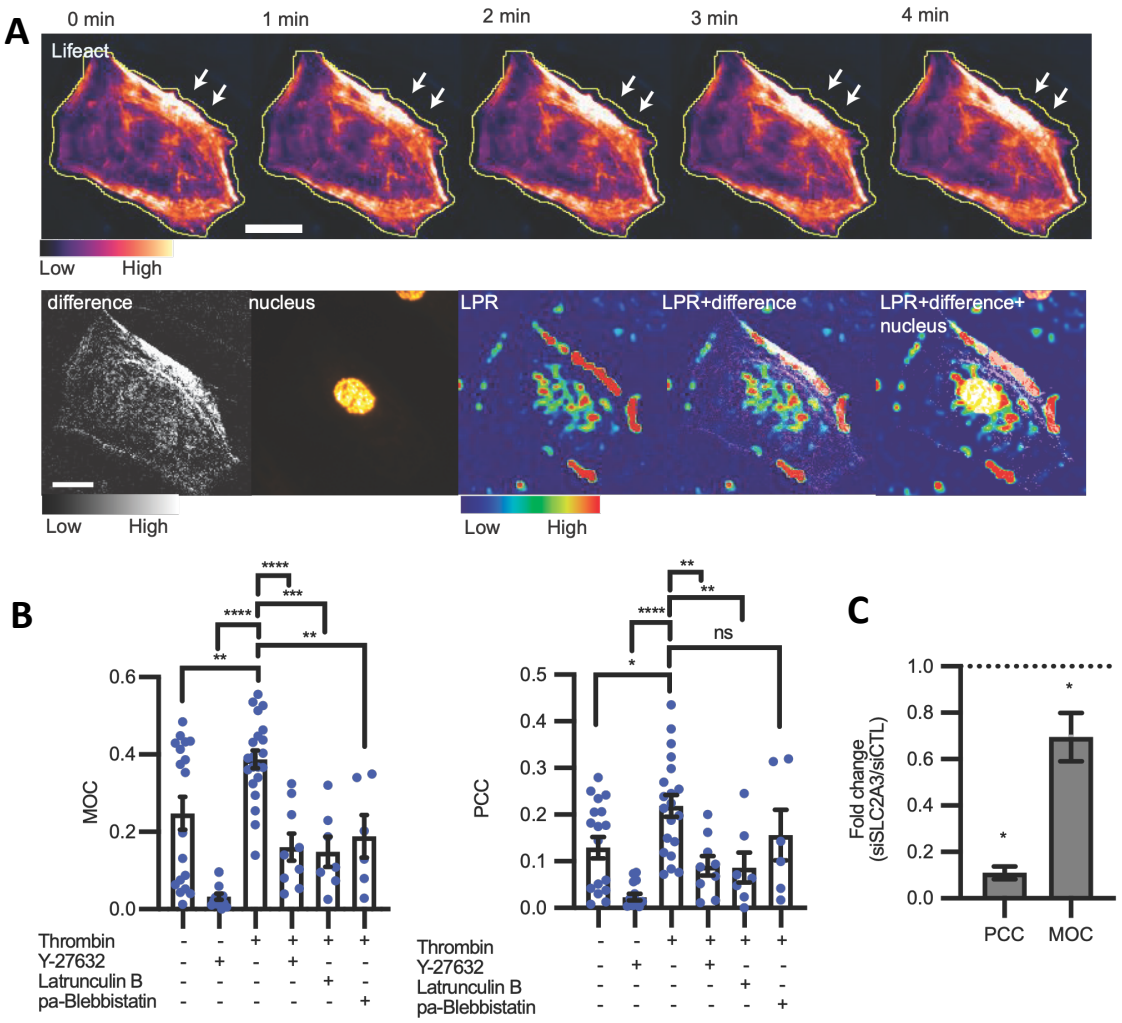


Figure 5.1: **Subcellular distribution of LPR colocalizes with actin remodeling in contractile cells.** (A) Representative montage of endothelial cell actin structure, as labeled with Lifeact-RFP, where the yellow line indicates original cell edge and white arrows point to contractile edge after treatment with thrombin (n = 14 biological replicates, 3 separate experiments). Maximum projection of change in actin structure (difference), nucleus, per pixel LPR map (LPR), and merges. Scale bar = 30 μm. (B) MOC and PCC of unstimulated or stimulated cells in the presence of ROCK inhibitor (Y-27632), actin polymerization inhibitor (Latrunculin B), and myosin II inhibitor (paBlebbistatin: para-aminoblebbistatin), error bars are SEM. (n = 15, 14, 20, 9, 7, 6 from left to right. Thrombin vs. control, $p = 0.0035$; vs. Y27632, $p < 0.0001$; vs. thrombin + Y27632, $p < 0.0001$; vs. thrombin + latrunculin B. $p = 0.0002$; vs. thrombin + para-aminoblebbistatin, $p = 0.0040$). (C) Fold change of PCC or MOC of thrombin treated cells under SLC2A3 knockdown compared to siCTRL, all error bars are SEM. (n = 14 for both, $p = 0.0317$ for PCC, $p = 0.0151$ for MOC). Statistical significance was determined by one-way ANOVA followed by Bonferroni test (B) or by two-sided Welch's t-test (C).

Similarly, subcellular glycolysis using Laconic was assessed in migrating endothelial cells. Here, the Lifeact difference image was computed for the 10 minutes prior to performing the LPR assay (Figure 5.2A, difference image). In migrating HAECs, LPR and Lifeact difference were significantly correlated, compared to control (performed by randomizing the LPR images 10,000 times and computing the MOC or PCC) (Figure 5.2B). These results indicate spatial cytoskeletal remodeling and glycolysis are correlated in multiple types of endothelial motilities.

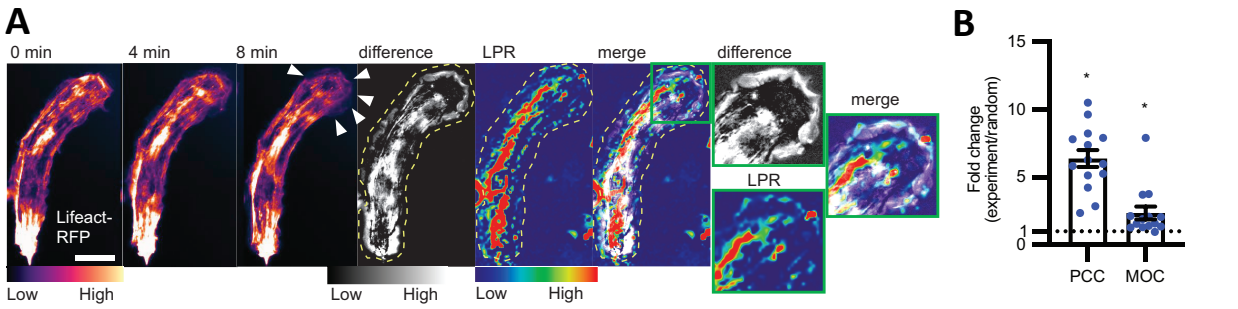


Figure 5.2: **Subcellular distribution of LPR colocalizes with actin remodeling in migratory cells.** (A) Montage of actin timelapse in a migratory endothelial cell; maximum projection of change in actin structure (Lifeact difference image, obtained by sequential subtraction of preceding 10 images, taken 1 minute apart, followed by maximum intensity projection of the absolute value of the differences), per pixel LPR map (LPR), Lifeact difference and LPR overlap ("difference+LPR", merge), scale bar = 20 µm. White arrows in montage indicate cell spreading. Green outline shows enhanced LPR near the regions of cell spreading. Representative of n = 14 cells, 3 separate experiments. (B) Pearson's correlation coefficient (PCC) and Manders' overlap coefficient (MOC) of Lifeact difference and LPR, compared to random. The random PCC/MOC is calculated by randomizing the LPR image and computing with the Lifeact difference image. Fold change of experimental PCC/MOC over randomized is shown. (n = 14). Error bars are SEM, p = 0.014 for PCC and p = 0.0489 for MOC. Statistical significance determined by two-sided Welch's t-test.

5.3 Subcellular distribution of LPR and RhoA activity are similar

Since activation of RhoA is required for the correlation between LPR and actin remodeling to occur, I next wanted to determine whether subcellular LPR was spatially related to RhoA activity. RhoA activity was evaluated using a FRET-based biosensor RhoA-Flare (Pertz et al. 2006) in single contractile endothelial cells. The design of RhoA-Flare is as follows: RhoA is attached to a

fragment of Rhotekin, a protein that will only bind activated or GTP-bound RhoA but not inactive or GDP-bound RhoA. Two fluorescence proteins capable of undergoing FRET are in the same chain between RhoA and Rhotekin such that the FRET will be altered by activated RhoA binding to Rhotekin. Unfortunately, the FRET pair used by RhoA-Flare is CFP/YFP which spectrally overlaps with mTFP/Venus, the FRET pair used by Laconic. Therefore, I could only evaluate RhoA activity and LPR in separate cells, then relate their subcellular pattern of activation based on location. There was enhanced RhoA activity and increased LPR co-located in similar areas following thrombin stimulation: the center of the cells (Figure 5.4A) as well as along the edges of the contractile aspects of the cell (Figure 5.4A-C, Figure 5.5). In contrast, where the cell edge did not move, there was no FRET (RhoA activity) (Figure 5.5G). Edges with persistent contraction consistently demonstrated high RhoA-Flare FRET (Figure 5.5C,H). The similar distribution of RhoA activity and LPR was further confirmed by comparing stationary edges vs contractile edges across multiple cells, averaged together (Figure 5.4D-E). This data revealed that the non-uniform localized distribution of metabolism correlates with cytoskeleton remodeling at the subcellular level. These results further showed co-localization between LPR and RhoA activities, suggesting that an endothelial cell generates energy using glycolysis to drive actin remodeling through GTPase RhoA.

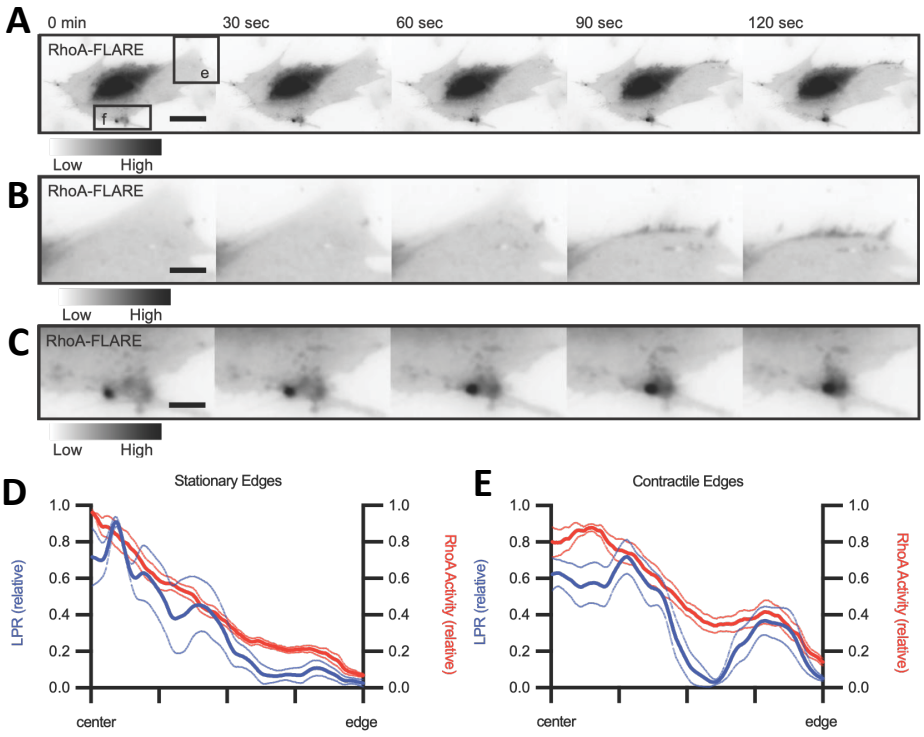


Figure 5.3: **Subcellular RhoA activity and LPR are spatially similar.** (A) RhoA activity measured by RhoA-FLARE in a contracting endothelial cell (scale bar = 15 μm). (B-C) Regions (B) and (C) from (A) demonstrate high RhoA activity in areas of active contraction (scale bar = 4.5 μm) (A-C representative of n = 9 cells, 3 biological replicates). (D-E) Normalized LPR and RhoA activity distribution from cell center to edge of non-contractile/stationary edges (D) and contractile/motile edges (E) stimulated with thrombin. (LPR stationary, n = 4; RhoA stationary, n = 6; LPR contract, n = 8; RhoA contract, n = 9). Dotted lines are standard deviation.

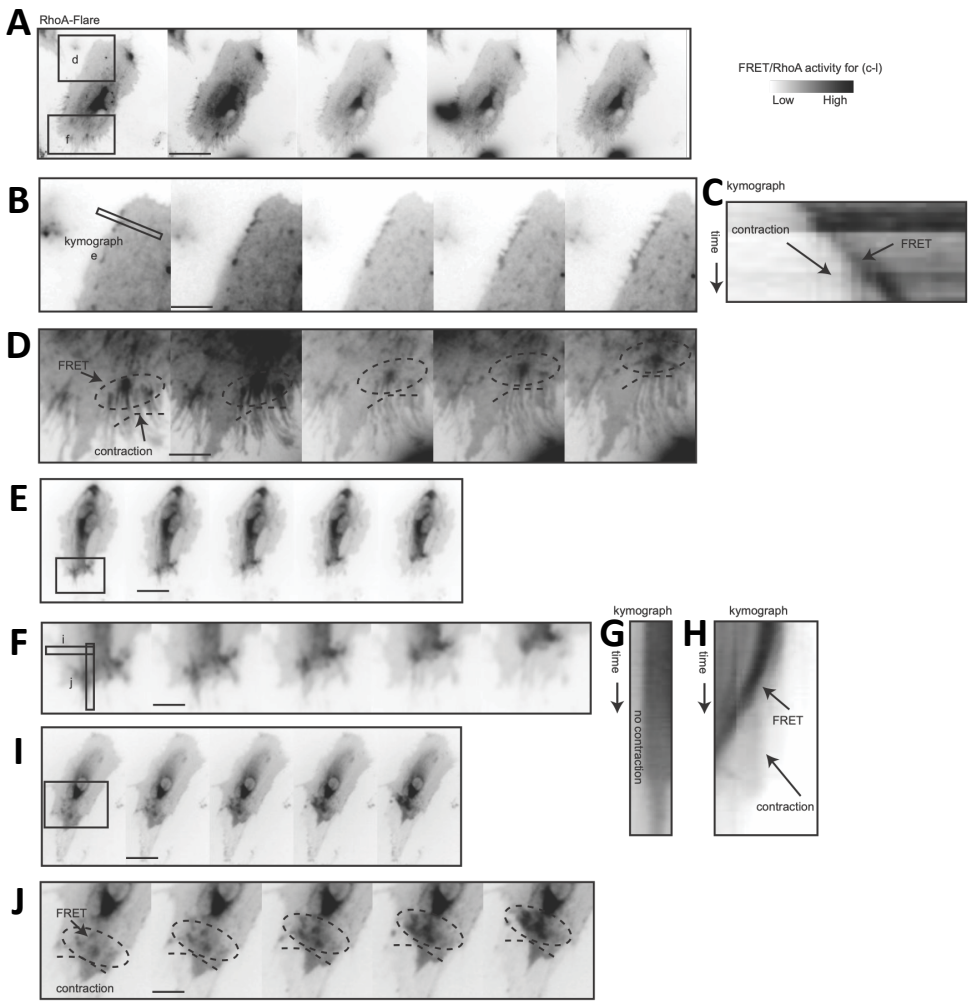


Figure 5.4: **RhoA activity is highest at the center of cells and contractile cell edges.** (A-J) RhoA activity measured by RhoA-FLARE in contractile endothelial cells. Representative data of total n = 9 cells in 3 replicates. (Scale bar = 16 μm in A, E, I. Scale bar = 7 μm in B, D, F, J). B,D, regions of contractile cell from (A) showing RhoA membrane activity. Circle in (D) notes moving RhoA activity. (C) kymograph showing contractile edge from (B) and increasing RhoA activity over time. (F) region of contractile cell from (E) showing increased RhoA membrane activity. G-H, kymograph showing non-contractile edge (G) without RhoA increase and contractile edge (H) from (F) and increasing RhoA activity over time. (J), region of contractile cell from (I) showing RhoA membrane activity. Dotted ellipses notes highlight increasing RhoA activity along with active contraction.

5.4 Conclusions and future directions

Altogether, my single-cell metabolic assays revealed molecular mechanisms that RhoA/ROCK-1 activates SLC2A3 translocation to trigger a glycolytic burst to power the endothelial contractile apparatus across multiple endothelial types (Figure 5.5). Furthermore, subcellular analysis of LPR revealed the non-uniform, localized distribution of glycolysis at site of actin turnover and RhoA activity, indicating RhoA signaling coordinates energy production through glycolysis with energy consumption through cytoskeletal remodeling to control cell motility. However, several steps within this mechanism warrant further investigation such as: How does glycolysis affect the activity of kinases and actin bundling proteins that are downstream of RhoA? How exactly are the glucose transporters translocated? Are the glycolytic enzymes located near sites of higher LPR? Ultimately, probing this mechanism deeper would help our understanding of motile phenotypes in normal conditions but could also elucidate molecular targets under pathogenic conditions, such as in barrier dysregulation.

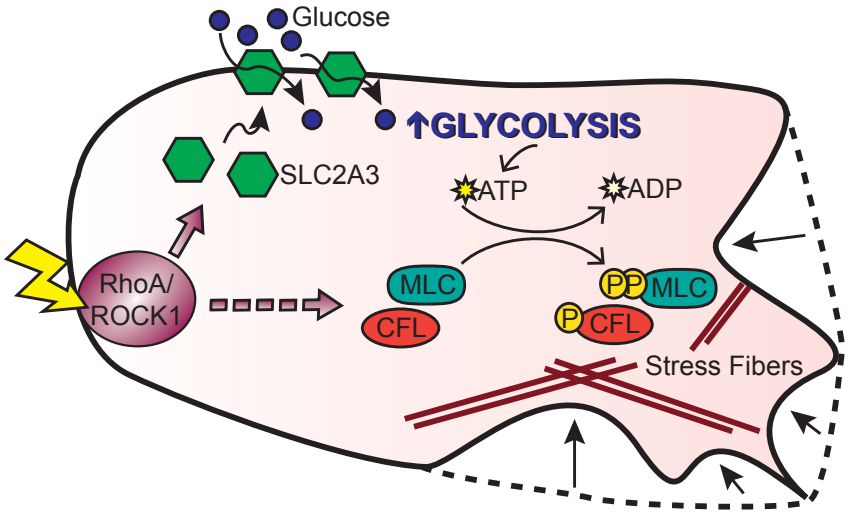


Figure 5.5: **Proposed mechanism of RhoA regulating glycolysis and contraction.** Agonism of RhoA/ROCK1 stimulates SLC2A3 translocation to the membrane to increase intracellular

Figure 5.5, continued: glycolysis, thereby providing the substrate for phosphorylation of downstream targets (MLC and CFL), resulting in stress fiber formation and, ultimately, contraction.

CHAPTER SIX

CONCLUSIONS AND PERSPECTIVES

6.1 Introduction

Cell movement is spatially heterogeneous and requires energy. How energy is produced and consumed in order to fuel heterogeneous motility is unknown. However, most studies measure cell metabolism using bulk assays. Reprogrammed metabolic rates to support different cellular functions has rightfully gained attention but experimental methods to directly evaluate heterogeneous populations remain in infancy. To decipher the metabolic states of individual cells, I used a FRET-based metabolic imaging method to measure single-cell metabolism with subcellular resolution. This single-cell metabolism method is complementary to existing ensemble metabolic assays and broadly applicable to different cell types. With this method, I was able to investigate the underlying molecular mechanisms of glycolysis in endothelial cells. This method enabled us to link heterogeneous glycolytic states to GTPase RhoA-activated phenotypes across variable time scales (low shear stress: days, migration: hours, and contraction: minutes) in individual endothelial cells. This method also allowed us to explore spatially heterogeneous metabolism and motility within individual cells. Given the feasibility, reproducibility, and robustness of this approach, it should have widespread applications to study metabolic support of single-cell functions in cell biology.

Though these findings described here further our understanding of the coordination of cellular motility with energy production/consumption, they also leave us with interesting observations and future directions. Therefore, I will detail future lines of investigation that I think warrant research effort given my findings. These include (1) further evaluation of

mechanotransduction and the metabolon, (2) cell motility and regulation of glycolysis in additional cell types such as T cells, (3) the evaluation of lactate as a mechanism for cellular memory through histone lactylation, and (4) SLC2A3's role in the development or treatment of vascular endothelium pathologies.

6.2 Mechanotransduction and the metabolon

In addition to identifying single-cell metabolic heterogeneity, I found non-uniform distributions of glycolytic rates within single motile cells, specifically at sites of actin turnover and RhoA activity. RhoA-coupled glycolysis and contractile machinery demonstrated here also support an emerging paradigm that cellular metabolism and cytoskeleton architecture are intimately coordinated in an "energetic metabolon" (Menard, Maughan, and Vigoreaux 2014). Unlike mitochondria, which have encapsulated the enzymes necessary for rapid and high-throughput ATP generation, glycolysis occurs within the cytoplasm. Therefore, the cell could be organizing glycolysis to be rapidly inducible at sites of high energy demand. These results suggest that an endothelial cell is energetically frugal and samples the environment for energetic precursors only when necessary: here, the cell employs RhoA/ROCK-1 to couple energy production with acute energy-consuming responses such as cytoskeletal remodeling to enable contraction. This could be functionally essential, as the continued presence of high energy phosphates in a cell may make controlling enzymatic phosphorylation difficult. Thus, having a local, segregated pool of transmembrane receptors may enable digital-like spatial control of phosphorylation (J. Huang et al. 2013). Co-localization of glycolytic enzymes with energetic demand could provide an efficient way for the cell to not only temporally determine when energy is produced, but spatially control where energy

is consumed, preventing futile reactions, avoiding energy over-production, and overcoming diffusion limitation.

"Glycolytic metabolons" have been suggested in endothelial cells, with increased ATP in in the perinuclear cytosol and lamellipodial ruffles (De Bock et al. 2013), and evidence that glycolytic enzymes bind to the actin cytoskeleton (Masters 1984). Here, using single-cell metabolic assays, I directly visualized the highly localized, enriched lactate production in subcellular endothelial edges and perinuclear sites, providing evidence to functionally support the "glycolytic metabolon" theory. Though we found the induction of the contractile machinery via RhoA to be the endpoint of glycolysis, ATP is required for more molecular alterations that affect cellular motility. Most importantly, actin filament assembly itself requires ATP but we were unable to effectively dissect this relationship.

Furthermore, the cytoskeleton could itself be regulating glycolysis perhaps as a mechanism to overcome diffusion. For example, aldolase binding to actin regulates its activity and glycolytic enzymes can form multimeric complexes perhaps through the association to the cytoskeleton (Hu et al. 2016; Norris et al. 2013). Additionally, Park et al. found that the softness of substrates can decrease cellular glycolysis through actin-dependent release of TRIM21 which labels PFK, a glycolytic enzyme, for degradation (Park et al. 2020). Such subcellular regulation and distribution of glycolysis would overcome diffusion limitations in energetically demanding processes. Though glucose could be taken up and diffused evenly throughout the cell, the enzymes that convert it into usable energy could be located and regulated at sites specifically where ATP demand is high and ATP usage is rapid. Additionally, cytoskeletal regulation of glycolysis would be beneficial for cells seeking suitable environments. In the absence of oxygen, cells could still use glycolysis to provide the ATP necessary for the cell to relocate to a region with adequate nutrients without the

usage of the mitochondria. However, further studies linking the subcellular glycolytic rate and distribution of glycolytic machinery are needed to strengthen and validate this theory.

Future investigation of subcellular endothelial glycolysis would benefit from tracing high energy phosphates from where they are produced, to sites where they are consumed. For instance, FRET biosensors can be further engineered to target the plasma membrane, specific organelles, or the cytoskeleton. Additionally, future studies could incorporate LPR with assays that can measure force generation such as traction force microscopy to see whether or not glycolysis is used specifically for generating the forceful pushes necessary for cell movement. Altogether, understanding how glycolysis is regulated subcellularly would aid in our understanding of why specific cell types prefer to use cytoplasmic glycolysis over mitochondrial oxidative phosphorylation for ATP production. Given that many cell types including cancer cells and immune cells exhibit this Warburg effect, investigation of the energetic metabolon could have far-reaching implications in cell biology and disease.

6.3 Motility and glycolysis in other cell types

Our method was demonstrated in both endothelial cells and T cells due to their glycolytic and motile nature. However, the RhoA-triggered glycolytic burst and demonstrated glycolytic heterogeneity was only found in endothelial cells. Certainly, understanding the interplay between glycolysis and motility in cell types such as cancer cells during metastasis and neurons during brain development would provide fruitful results. However, I will describe specific questions in T cells, which demonstrate strong similarities to endothelial cells and have already been successfully employed in the single-cell LPR assay. In T cells, there are many interesting questions regarding

how metabolism supports cellular function (Harrison, Fang, and Huang 2019) but I will describe two major contexts in which glycolysis warrants further study: T cell activation and differentiation.

It is well established that lymphocyte activation is a mechanosensitive process. Following engagement of a TCR to a pMHC, intracellular signaling occurs that leads to the formation of an immunological synapse at the point of contact including phosphorylation events. The synapse promotes strong adhesion and cytoskeletal polarization towards the APC while excluding inhibitor molecules. F-actin dynamics apply the forces that are required for the activation of mechanosensitive receptors. TCR microclusters assemble to the center of the synapse at the tips of actin-rich protrusive surfaces by retrograde F-actin flow at the periphery. These protrusions promote signaling by enabling the T cell to penetrate the APC glycocalyx and bring its TCRs closer to its pMHC ligands(G. P. van Nieuw Amerongen, Vermeer, and van Hinsbergh 2000). Additionally, glycolysis is upregulated immediately after T cell activation, temporally similar to how RhoA induces a glycolytic burst in endothelial cells. Because cytoskeleton remodeling requires energy and some metabolic enzymes contain putative actin-binding domains, a synergistic role between metabolic reprogramming and cytoskeleton remodeling in T cell activation and differentiation becomes apparent. Similar to the contractile machinery in endothelial cells, Rho GTPases drive cytoskeletal remodeling in activated cells and phosphorylation events are required for downstream signaling. Perhaps glycolysis could be induced following cell activation to support cytoskeletal remodeling as well as downstream signaling. However, the directionality and molecular players of this mechanism must be uncovered for further elucidation.

T cells will also change their dominant metabolic program depending on the final fate and function of the differentiated T cell (Karmaus et al. 2019; Bantug et al. 2018). Naïve T cells remain in a quiescent metabolic state since they do not need energy for clonal proliferation or cytokine

production. Without the need to induce anabolic pathways for the *de novo* generation of DNA, lipids and proteins, naïve T cells mainly maximize energy production through OXPHOS (Almeida et al. 2016). Upon antigen recognition, however, naïve T cells become highly proliferative and differentiate into Teff cells, requiring a new metabolic program that supports division and biosynthesis. Activated T cells engage aerobic glycolysis to increase the availability of glycolytic precursors for biosynthetic reactions such as protein, nucleotide and lipid synthesis (Menk et al. 2018). Moreover, most enzymes involved in glycolysis can enter the nucleus where they can exert alternative roles affecting the transcription and stability of factors associated with cell proliferation. Regulatory T cells, however, are less glycolytic and rely instead on Fatty Acid Oxidation (FAO) and OXPHOS, resembling the naïve T cell phenotype. Furthermore, transcription factors involved in metabolism play a role in T cell differentiation (R. Wang et al. 2011; Song et al. 2016). It is possible that cell activation which stimulates glycolysis drives cells towards an effector phenotype. This is further evidenced by the finding that glycolysis is induced rapidly following activation, is highest in effector T cells, and is shown to be increased in exhausted T cells, which are effector T cell that lose their ability to mount an effective immune response. Therefore, modulating the metabolic program of a T cell could potentially drive it towards one cell fate versus another or prevent unwanted T-cell exhaustion. However, the mechanism by which metabolism drives differentiation or genetic remodeling requires further exploration.

6.4 Lactate as an epigenetic regulator

Cellular lactate is the terminal metabolite of glycolysis that is often exported as a waste product but it could also be used by the cell in order to change gene expression. Recently, it has been shown that histones can be modified by lactylation in order to epigenetically modify the architecture of

DNA, thus changing gene expression in a heritable way (D. Zhang et al. 2019). Here, lactate production was found to be highest at the cell edge and center of contractile cells. Though I attribute this to energy demand at locations of high RhoA activity, one could hypothesize that lactate could also be produced locally for usage for other cellular processes such as histone lactylation within the nucleus (D. Zhang et al. 2019).

Perhaps the increase of local glycolysis could act as a signal for the cell to adapt to a changing environment, thus imprinting acute stimuli into cellular memory. It is possible that glycolysis could somehow be perpetuating glycolysis or motility pathways through this mechanism. Imagine a cell that has to contract or migrate once, it might induce rapid glycolysis to fuel that quick action, but what if this acute stimulus turned chronic? It's possible that the induction of glycolysis multiple times or for a sustained period could create enough lactate that serves as a signal to the cell to change the expression of genes. In order to test this, Laconic can be modified to be targeted to the nucleus so that lactate can be tracked intranuclearly over time and correlate this with changes in gene expression or genetic architecture. By understanding how lactate can be used by cells, glycolysis can be further recognized as an important metabolic pathway not just for energy production, but genetic fate determination as well.

6.5 SLC2A3 in human health

Integrating this single-cell metabolic method with classic molecular and functional analyses also allowed us to discover the causal role of RhoA in stimulating a SLC2A3-dependent glycolytic burst necessary for endothelial contraction. Although it is commonly recognized that SLC2A1/GLUT1 is a major glucose transporter in endothelial cells across diverse vascular beds

and contributes to basal glycolysis under chronic transcriptional activation (D. Wu et al. 2017; M. Tang et al. 2017; Fessel et al. 2012; Y. Huang et al. 2012), these results revealed the critical role of SLC2A3/GLUT3 in triggering a metabolic burst, defined by a quick increase in glucose uptake, glycolysis, and ATP level. ATP budget and nutrient availability plays an important role in cellular decision making, including certain endothelial behaviors (Diebold et al. 2019; Wilhelm and et al. 2016; Kuo, Lee, and Sessa 2017; Yu et al. 2017). Using this mechanism, a single endothelial cell can augment its glycolytic potential even further with SLC2A3 transmembrane recruitment during acute stimuli in cellular processes requiring an immediate energy burst. We also demonstrated that vascular leak was increased in an endothelial overexpression model of SLC2A3 *in vivo*. In highly-glycolytic platelets where SLC2A3 is enriched, thrombin (a potent platelet activator) can stimulate SLC2A3 plasma membrane translocation (Sorbara et al. 1997), suggesting a conserved molecular function. Exactly how RhoA/ROCK-1 causes transmembrane expression of SLC2A3 certainly requires further exploration. However, investigation of SLC2A3's role in regulating vascular pathophysiology could bolster the case that modulating signal transduction by interfering with cellular energetics could be a fruitful path to novel pharmacotherapeutics in vascular pathologies (R.-T. Huang et al. 2017). For example, does SLC2A3 play a role in the development of atherosclerotic plaques, where endothelial activation, glycolysis, and permeability are increased? Could SLC2A3 be selectively induced for vascular remodeling in ischemic tissue? The physiological role of endothelial SLC2A3 in vascular homeostasis and disease *in vivo* deserves future investigation.

6.6 Conclusions

All cells must move but their motile behaviors are inherently heterogenous. This heterogeneity could be caused by differences in a cell's ability to transfer energy produced metabolically and used mechanically. Therefore, I investigated how spatially heterogeneous endothelial motilities can be fueled by energetic metabolism by developing a single-cell imaging assay to measure glycolysis with subcellular resolution. I demonstrated that endothelial migration and contraction, critical endothelial phenotypes, were driven by glycolysis at the single-cell and subcellular levels. I found energy-demanding cytoskeletal remodeling to be conducted by RhoA through SLC2A3-mediated glucose uptake and glycolysis. Through the investigation of how cells fuel movement, I made the following overarching conclusions (Figure 6.1):

1. Metabolic heterogeneity is measurable by the development of single-cell LPR assay in endothelial cells subjected to heterogeneous shear stress.
2. Single-cell glycolysis fuels heterogeneous cell migration in migratory and contractile cells
3. RhoA triggers a glycolytic burst through GLUT3/SLC2A3 to power endothelial cell contraction
4. Non-uniform subcellular glycolysis overlaps with cytoskeletal remodeling and RhoA activity

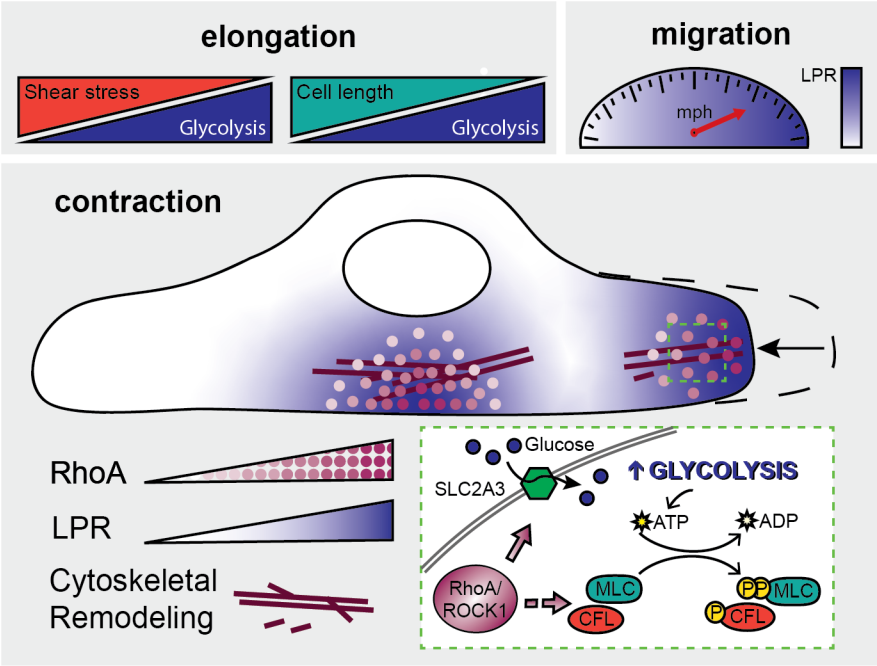


Figure 6.1: **Non-uniform single-cell and subcellular glycolysis fuels heterogeneous motility.** Metabolic heterogeneity was measurable by the development of the lactate production rate (LPR) assay. LPR measurements reveal negative correlations between shear stress and glycolysis in addition to cell length and glycolysis in endothelial cells subjected to heterogeneous flow rates. Single-cell LPR and speed of migratory cells are positively correlated. Within individual contractile cells, (1) RhoA activity and LPR are highest at the center and contractile edges and (2) cytoskeletal remodeling and LPR overlap. Mechanistically, RhoA induces a glycolytic burst through the translocation of SLC2A3 to increase glucose uptake, glycolysis, and induction of the contractile machinery (ppMLC and pCFL).

Altogether, these single-cell metabolic assays and mechanistic findings demonstrated the critical interplay between signaling, metabolism, and motility in dictating non-uniform phenotypes of individual endothelial cells. The data provided here suggest that energetic metabolism plays an integral part in cellular motility and that the two are tightly coordinated to ensure efficiency. These results aid in our understanding of basic cell biology but also could potentially serve as directions for future development of therapeutics to target pathologies with aberrant cellular motility or metabolism.

APPENDIX I:

SINGLE-CELL LACTATE PRODUCTION RATE PROTOCOL

A.I.1 Summary

The metabolic processes of individual cells are inherently heterogeneous, so there is a critical need for methods that can measure single-cell metabolism in real time. Here we describe deep-learning enabled image analyses of a genetically-encoded lactate-sensing probe which can accurately quantify spatiotemporal metabolite levels and glycolytic rates at the single-cell level. This method not only reliably discriminates between metabolically diverse subpopulations in multiple cell types, but can also directly link single-cell metabolism to functional phenotype by integrating spatial information, genetic or pharmacological perturbations, and real-time metabolic states. Major obstacles include successful expression of the sensor and adequate cell segmentation accurate permitting calibration and discrimination of intracellular lactate concentration in a high throughput fashion, which is the focus of the protocol.

For complete details on the use and execution of this protocol, please refer to Wu & Harrison et al. (2021).

A.I.2 Before you begin

This protocol involves imaging of endothelial cells expressing a genetically encoded sensor for lactate, Laconic (San Martín et al., 2013), within Ibidi imaging chambers capable of fluid exchange. Laconic is composed of a bacterially-derived lactate binding region flanked by two fluorophores, mTFP and Venus, capable of undergoing fluorescence resonance energy transfer (FRET). In the presence of lactate, the fluorophores will increase in molecular distance, thus reducing FRET. Prior to evaluating the lactate production rate, the sensor, imaging chamber, microscope, and computer for analysis must be set up.

Prepare Laconic for genetic introduction to cells

Timing: 1-4 weeks

Note: Laconic can be introduced to cells using a variety of transfection methods. We found adenoviral transduction into human aortic endothelial cells (HAEC) resulted in reliably homogenous expression and minimal cell death but have also used mRNA transfection in both primary cells and cell lines. See Figure A.I.1 for comparison of expression via these methods. For generating FRET control proteins, please see "Additional Controls."

1. For adenoviral transduction:
    a. Acquire Laconic plasmid from Addgene (#44238)
    b. Entrust Vector Biolabs to create Ad5 adenoviral Laconic from the Addgene plasmid (Link to manufacturer's services)
2. For mRNA production:
    a. Generate template for *in vitro* transcription via PCR using the T7-F and BGH-R primers (see Key Resources Table) and protocol listed in Table 1 and NEB Q5 Polymerase
    b. Purify PCR product using QIAquick PCR Purification Kit (Link to manufacturer's protocol)

Note: PCRs can be checked by running on a 1% agarose gel for the correct amplicon size (2403 bp).

    c. Using the PCR-generated template from 2b, create mRNA using mMESSAGE mMACHINE™ T7 ULTRA Transcription Kit (Link to manufacturer's protocol)
    d. After cleaning and eluting mRNA, aliquot (100 ng/µL) and store at -80 °C for minimal degradation. (Link to manufacturer's protocol)

- When eluting mRNA, preheat the elution solution to 95 °C and elute three times from one column using MEGAclear Transcription Cleanup Kit.
- Measure the concentration of the mRNA with a spectrophotometer, such as a BioTek Cytation 3 instrument using 2 µL of sample.
- Concentration of the mRNA can be adjusted with the supplied elution buffer.
- The lithium chloride precipitation method in the mMESSAGE mMACHINE™ T7 ULTRA Transcription Kit is also sufficient.

Alternative: In addition to Vector Biolabs, adenoviruses can be generated in house (Link to useful protocol) and is reviewed in (Danthinne and Imperiale 2000). The University of Iowa has a viral vector core facility (Link to website). Other commercial sources are also available such as Vigene Biosciences (Link to manufacturer's service) and abm (Link to manufacturer's service).

Note: Create mRNA transcripts for mTFP and Venus separately (the FRET pair in Laconic) for testing fluorescence bleed through in the filter sets in the microscope (see "Additional Controls" section).

Culturing human aortic endothelial cells (HAECs)

1. Culture HAECs in a 37 °C, 5% CO2 with humidity incubator. HAECs are suitable to use after they have been passaged at least once.
    e. Pipette 10 mL of EGM2 complete media into a T75 flask and let warm in incubator.
    f. Rapidly defrost HAECs in a 37 °C water bath, shaking.
    g. Immediately after defrosting, spray the cryo-tube with 70% ethanol and wipe off. In a sterile hood with laminar flow, pipette cells into the pre-warmed T75 flask. Wash the inside of the cryo-tube with media, aspirate, and pipette into T75 flask.
    h. After 4 hours and after cells have adhered to flask, aspirate media and add new, 37 °C warmed complete media (to get rid of DMSO).
    i. Change media on HAECs every 2-3 days. Split when 80% confluent (see section on plating cells below for further instructions).

Set-up of Ibidi imaging chambers

Timing: 1 hour

Ibidi imaging chambers are capable of fluid exchange which will be critical for establishing the calibration curve so that you are able to convert fluorescent values to lactate concentrations. See Figure A.I.2 for assembly.

1. Measure tubing length so that it can be used in your microscope set-up

a. Ideally, your microscope will have a chamber for controlling heat, humidity, and CO_2. In order to have fluid exchange without disturbing the chamber, the tubing should be long enough to reach outside of the chamber. The plastic versions of the Ibidi chambers are permeable to gas.

b. Test the volume of tubing you have by injecting a known amount of liquid through the line, then measuring how much comes out the other end. This will be important for determining the amount of solution you'll need to inject for thorough washing.

2. Assemble waste/output tubing

a. Attach one set of tubing to one elbow male connectors

3. Assemble input/injection tubing

a. Attach other set of tubing to one elbow male connector on left side

b. Attach female connector on opposite side

c. In-line injection port can be attached to female connector

d. Rinse thoroughly with 70% ethanol and PBS using syringes

4. Tubing can be saved for multiple experiments as long as the assembled apparatus is rinsed thoroughly with 70% ethanol and PBS between samples

Ensure optical set-up works with Laconic

Laconic is comprised of a bacterial lactate binding domain (LldR) flanked by two fluorophores capable of undergoing Fluorescence resonance energy transfer (FRET). As lactate concentration increases, the FRET ratio between the two fluorophores (mTFP and Venus) is reduced (San Martín et al., 2013~~)~~. Acquire filter sets that allow for excitation of mTFP and allow for emission in both the donor (mTFP) and acceptor (Venus) channels. Additional sets should be acquired for nuclei and membrane labeling (Hoechst and VE-CADH, respectively) but could also be used for multiplexed imaging.

This experiment requires a standard inverted microscope with either a stage top incubator on top or enclosure. Our heated, humidified, and CO2 controlled incubator was home built, but commercial ones are available – we recommend Okolab (Link to manufacturer's website) or Ibidi (Link to manufacturer's website). No special modifications to the microscope are necessary except for the incubator conditions and automated filter wheel; thus, any inverted microscope could in theory work. We suggest also having a computer-controlled shutter for automatically shuttering the emission light in between frame acquisitions to reduce photobleaching. For acquiring the

emission in two channels, an automated emission filter wheel must be used (see Key Resources). We used an epi-illumination metal halide light source. However, an LED light source should also be sufficient. Micro-manager was used to control the automated shutter and filter wheel through a controller, as well as camera.

- Olympus IX-71 epifluorescence microscope with a 10× 0.25 numerical aperture (NA) air objective and Prior automated emission filter wheel and excitation shutter. We chose a 10× objective for maximal data acquisition while still being able to segment the cells. Furthermore, the high depth of field allowed us to capture the fluorescence of the entire cell.
- FRET filter sets were from Semrock: excitation 438/24, mTFP emission 483/32, Venus emission 542/27, and dichroic FF458-Di02.
- Blue (Hoechst) and red (TRITC) filter sets for visualizing Hoechst stain and VE-CADH were from Semrock: Hoechst excitation 387/50, Hoechst emission, 447/60, Hoechst dichroic FF409-Di03, TRITC excitation 543/22, TRITC emission 593/40, TRITC dichroic FF562-Di03.
- Illumination: EXFO X-Cite metal halide light source
- Camera: Photometrics Prime95B. CMOS camera with high sensitivity, dynamic range, as well as speed. The protocol will likely work with other cameras – integration times may vary.

Alternative: Instead of using an automated emission filter wheel, split emission systems such as the Optisplit II by Cairn (Link to Manufacturer's website) can be employed for simultaneous acquisition of both emission channels, although this will change the downstream analysis considerably.

Critical: Filter sets with very little bleed through are necessary to avoid misinterpretation of FRET. For instance, the excitation in the mTFP channel should minimally excite Venus. The filter sets specified in this protocol minimize bleedthrough using the excitation light source specified; inclusion of bleedthrough did not change the calculation of FRET. Changing the light source may change the bleedthrough characteristics (see "Additional Controls").

Optional: Additional filter sets such as those used for TRITC, are not necessary but increase the potential for multiplexed imaging.

Deep learning computer

For training of the segmentation network, a computer outfitted with GPUs will drastically improve training time and segmentation. The computer should also have enough RAM for holding batches of images in memory when performing training. A minimum of 64 GB of memory is recommended. A CPU that has multiple cores is also critical for downstream analysis. For a quick comparison of CPUs check Geekbench.com. Pcpartpicker.com also has useful guides and compatibility charts for parts for building one's own computer, as the pricing and availability of

PC parts rapidly evolves. Computers sufficient to perform relatively quick computations are also available from retailers such as Lamda Labs, Bizon Tech, or Nvidia.

- We used 2 NVIDIA GeForce 1080 Ti and 1 NVIDIA Titan V GPUs.
- Our CPU is an AMD Ryzen Threadripper 12-core processor running at 3.50 GHz built in 2018.

Alternative: It is possible to perform deep learning on cloud computing servers readily available in large Universities or private providers such as Amazon Web Services. The code in this document assumes that computation is occurring locally on a Windows PC.

A.I.3 Key Resources Table

REAGENT or RESOURCE	SOURCE	IDENTIFIER
Antibodies		
Human VE-Cadherin/CDH5 (D87F2) XP® Rabbit mAb	Cell Signaling	Cat#2500S; RRID# AB_10839118
Alexa Flour 488 Goat Anti-Rabbit IgG	Life Technologies	Cat#A11034; RRID# AB_2576217
Alexa Flour 594 Goat Anti-Mouse IgG	Life Technologies	Cat#A11037; RRID# AB_2534095
Bacterial and Virus Strains		
Adenovirus-Laconic	This paper, generated by Vector Biolabs	https://www.vectorbiolabs.com/adenovirus-construction-service/
Chemicals, Peptides, and Recombinant Proteins		
Dimethyloxalylglycine (DMOG)	Sigma-Aldrich	Cat#D3695
4-chloromercuribenzoic acid (pCMBA)	Sigma-Aldrich	Cat#C5913
Phloretin	Sigma-Aldrich	Cat#P7912
Nigericin	Tocris	Cat#4312
Glucose	Sigma-Aldrich	Cat#G8270
Sodium Lactate	Sigma-Aldrich	Cat#L7022-5G
Rotenone	Sigma-Aldrich	Cat#R8875

Sodium Chloride (NaCl)	Sigma-Aldrich	Cat#S3014-25KG
Potassium Chloride (KCl)	Sigma-Aldrich	Cat#P9333-500G
HEPES (solid)	Thermo Fisher Scientific	Cat#BP310-500
HEPES (solution)	Thermo Fisher Scientific	Cat#15630080
Calcium Chloride ($CaCl_2$)	Sigma-Aldrich	Cat#C8106
Magnesium Sulfate (MgSO4)	Sigma-Aldrich	Cat# M7506
Sodium Bicarbonate ($NaHCO_3$)	Sigma-Aldrich	Cat#S5761-500G
NEB Q5 Master Mix	New England Biolabs	Cat#M0492S
mMESSAGE mMACHINE™ T7 ULTRA Transcription Kit	Thermo Fisher Scientific	Cat# AM1344
QIAquick PCR Purification Kit	Qiagen	Cat#28104
MEGAclear™ Transcription Clean-Up Kit	Thermo Fisher Scientific	Cat# AM1908
Phosphate buffered saline (PBS), pH 7.4, without Ca^{++} or Mg^{++}	Invitrogen	Cat#10010
Dulbecco's Phosphate buffer saline (DPBS) with Ca^{++} or Mg^{++}	Invitrogen	Cat#14040
TrypLE express	Gibco	Cat#12605010
Fluorobrite DMEM	Thermo Fisher Scientific	Cat#A1896601
Opti-MEM	Life Technologies	Cat#31985-070
DMEM high glucose	Invitrogen	Cat#NP0366
GeneJammer Transfection Reagent	Agilent	Cat#204130
MessengerMax	Thermo Fisher Scientific	Cat#LMRNA003
EGM2 complete media	Lonza	Cat#CC4176 and CC3156

Paraformaldehyde, 32%	Electron Microscopy Sciences	Cat#15710
Triton-X 100	Sigma-Aldrich	Cat#X100-100ML
Bovine serum albumin	Sigma-Aldrich	Cat#A2153
Tris-buffered saline (TBS), 10x	Sigma-Aldrich	Cat#T5912
Tween-20	Sigma-Aldrich	Cat#P9416
Mounting medium	Thermo Fisher	Cat#P36965
Hoechst33342	Invitrogen	Cat#H3570
Deposited Data		
Sample data (Wu, D. & Harrison, D. et al., 2021)	Zenodo.org	DOI:10.5281/zenodo.4638059
Ground truth sample data set and sample network (Harrison, D. & Wu, D. et al., 2021)	Zenodo.org	DOI:10.5281/zenodo.4898134
Experimental Models: Cell Lines		
Human Aortic Endothelial Cells (HAECs)	Lonza	Cat#CC-2535
Oligonucleotides		
T7-F, TAATACGACTCACTATAGGG	IDT	N/A
BGH-R, TAGAAGGCACAGTCGAGG	IDT	N/A
mTFPr, TTAGGTACCAGATCTCTTGTA	IDT	N/A
T7-Venus, TTAATATAATACGACTCACTATAGGGACGATTCGATGAAGATCAG	IDT	N/A
Recombinant DNA		
Laconic (San Martín et al., 2013)	Addgene	Cat#4423
Software and Algorithms		
CellProfiler 3.1.8 #(Carpenter et al., 2006)	Broad Institute	https://cellprofiler.org/
MATLAB R2018b, including Deep learning toolbox	MathWorks	https://www.mathworks.com/products/deep-learning.html
Prism 8	Graphpad	https://www.graphpad.com/scientific-software/prism/
MicroManager	Vale Lab, UCSF	https://micro-manager.org/
MATLAB code and scripts	This paper	https://github.com/wulab-code/STAR_methods
Instruments		
Spectrophotometer	BioTek Cytation 3	CYT3MF

Olympus IX-71 epifluorescence microscope	Olympus	N/A
Objective (10x Plan C Achromat, NA 0.25)	Olympus	N/A
Excitation filter 438/24	Semrock	FF02-438/24-25
mTFP emission 483/32	Semrock	FF01-483/32-25
Venus emission 542/27	Semrock	FF01-542/27-25
FRET dichroic FF458-Di02	Semrock	FF458-Di02-25x36
Hoechst excitation 387/50	Semrock	FF01-387/11-25
Hoechst emission, 447/60	Semrock	FF02-447/60-25
Hoechst dichroic FF409-Di03	Semrock	FF409-Di03-25x36
TRITC excitation 534/22	Semrock	FF01-543/22-25
TRITC emission 593/40	Semrock	FF01-593/40-25
TRITC dichroic FF562-Di03	Semrock	FF562-Di03-25x36
Prime 95B	Photometrics	N/A
EXFO X-Cite 120Q	Excelitas	010-00157
Controller for shutter and filter wheel	Prior	ProscanIII
Automated excitation shutter	Prior	HF202HT
Automated emission filter wheel	Prior	HF108IX3
Other		
µ-Slide VI Luer, Ibidi imaging chambers	Ibidi	Cat#80606
5 m Silicone Tubing 0.8 mm ID	Ibidi	Cat#10841
50 Elbow Luer Connector Male	Ibidi	Cat#10802
25 Luer Lock Connector Female	Ibidi	Cat#10825
In-line Luer Injection Port	Ibidi	Cat#10820
BD Needle 25g 0.62in	Thermo Fisher Scientific	Cat#10777-019
1 mL Syringes	Thermo Fisher Scientific	Cat#14-829-45
10 mL Syringe	Thermo Fisher Scientific	Cat#14-955-459

A.I.4 Materials and equipment

Stock solutions (all filter sterilized)

- pCMBA (MCT inhibitor), 500 mM in DMSO, store at -20°C
- Phloretin (alternative MCT inhibitor for pCMBA), 100 mM in DMSO, store at -20°C

- Glucose, 1 M in ddH_2O, store at 4°C long term or room temperature short term
- Nigericin, 10 mM in absolute ethanol, store at -20°C
- Rotenone, 2.5 mM in DMSO, store at -20°C
- Sodium Lactate, 1 M in water, store at room temperature

Additional Solutions

- TBST. Dilute 10x TBS into ddH2O, and add 0.1% Tween-20, mix thoroughly. Store at room temperature.
- Paraformaldehyde, 4%. Dilute stock (32%) into PBS, pH 7.4 to make 4% solution before use. Can be frozen for up to 12 months.
- Blocking buffer: TBST with 3% BSA. Store at 4°C for 6 months.
- Viral Media: DMEM high glucose with 10mM HEPES. Store at 4°C for 6 months.

Intracellular Buffer (ICB)

Reagent	**Final Concentration (mM)**
NaCl	10 mM
KCl	130 mM
HEPES	1.25 mM
ddH_2O	n/a

Filter sterilize and store at room temperature.

Extracellular Buffer (ECB)

Reagent	**Final Concentration (mM)**
NaCl	112 mM
KCl	5 mM
$CaCl_2$	1.25 mM
$MgSO_4$	1.25 mM
HEPES	10 mM
$NaHCO_3$	24 mM
ddH_2O	n/a

pH to 7.4, filter sterilize, and store at room temperature.

Alternatives: Phloretin can be used in place of pCMBA for MCT blockade, see troubleshooting. Trypsin can be used instead of TrypLE.

Optional: Any software can be used to generate figures from analyzed data but we use Prism 8.

A.I.5 Step-by-step method details

Introduce Laconic genetically - Day 1

Timing: 1-1.4 hours with overnight incubation

In order to have cells expressing Laconic at highest levels, introduce Laconic adenovirus vector (ad-Lac) 2 days prior to imaging.

1. Plating cells
    a. Aspirate media from T75 containing HAEC that is ~80-100% confluent and wash flask with warmed, sterile 5 mL PBS and aspirate.
    b. Add 1mL TrypLE and incubate in 37 °C, 5% CO2 with humidity incubator for 1-2 min.
    c. Check cells under microscope. If cells have become rounded, tap flask gently 10-20 times so that they come off. If cells have not become rounded, wait 1 min. Do not exceed 3 min total. Aim for ~80% of cells to detach.
    d. Add 5 mL EGM2 complete media to flask, washing the bottom of the flask to remove any adherent cells.
    e. Aspirate cells and spin at 100 g, 5 min at room temperature.
    f. Aspirate supernatant and resuspend cells in 1mL of EGM2 complete media.
    g. Count cells.
    h. Seed cells into wells so that there are ~200,000 cells/well (in 12 well plate) with enough time before transduction for the cells to adhere (1 day for human aortic endothelial cells).
2. Prepare reagents
    a. Warm Viral Media and complete media in 37 °C water bath
    b. Defrost adenovirus Laconic stock from -80 °C on ice
3. Prepare transduction master mix for half culture volume (500 µL for 12 well)
    a. Multiplicity of infection (MOI) = Plaque forming units (PFU) of virus used for infection / number of cells. We recommend starting with a MOI of 50:1.
        i. E.g.: for a virus of 3.40E+10 pfu/mL to be used at 50:1 MOI used in 200,000 cells/12 well, use 0.29 µL virus and 1.5 µL GeneJammer in 500 µL viral media per well
    b. Make master mix if using multiple wells

c. Mix by gentle swirling/pipetting. Do not vortex.

4. Aspirate viral media and apply transduction mixture to each well
    a. Incubate for 1 hour in 37 °C at 5% CO_2
5. Remove viral media gently and replace with complete media
6. Incubate overnight at 37 °C, 5% CO2, humidified.
7. Visualize transfection efficiency on a fluorescence microscope (Figure A.I.1). Transfection efficiency can be roughly estimated by using a microscope and looking for signs of altered cell morphology which signals unhealthy cells. Every cell should be fluorescent with enough signal to obtain an accurate intracellular lactate calibration curve using a reasonable camera integration time (Figure A.I.3). Too much adenovirus (in our hands, 200:1 MOI) results in altered cell morphology and cell death.

Critical: Virus must be kept on ice to ensure transduction efficiency. Virus should be aliquoted appropriately so that each tube isn't thawed more than twice.

Critical: Anything containing virus must be used with caution according to BSL-2 guidelines. Disposables and solutions containing virus must be disposed of separately from other reagents in 10% bleach.

Note: GeneJammer is not necessary but will improve expression.

Note: Solution changes must be done gently following transduction as the cells are especially sensitive to lifting off the plate.

mRNA transfection of Laconic (Alternative to adenovirus)

Timing: 1 hour with overnight incubation

For mRNA transfection using Lipofectamine™ MessengerMax ™ reagent:

1. Prepare cells
    a. Seed adherent cells into wells so that there are ~200,000 cells/well (in 12 well plate) with enough time before transduction for the cells to adhere (1 day for human aortic endothelial cells). See above on plating cells for directions.
2. Prepare reagents
    a. Warm Opti-MEM and EGM2 complete media in 37 °C water bath
    b. Defrost mRNA stock from -80 °C on ice
3. Make master mix of lipofectamine MessengerMax reagent (Link to manufacturer's protocol)
    a. for 12 well plate: 50 µL total solution = 3 µL MessengerMax into 47 µL Opti-MEM.

b. Create master mix for multiple wells

c. Vortex master mix and incubate at room temperature for 10 min while you prepare mRNA mixes

4. Prepare mRNA solutions so that final concentration is 160 ng/cm^2

   a. For 4 cm^2 well (12 well), 50 µL solution = 7.1 µL mRNA (100 ng/cm^2) into 42.8 µL Opti-MEM

   b. Mix by triturating

5. Add Master mix of lipofectamine reagent to mRNA solutions in 1:1 volume ratio (50 µL:50 µL for 12 well)

   a. Mix by triturating

   b. Incubate at room temperature for 5 min

6. During incubation in step 5b, replace media in wells containing cells to 900 µL complete media total

7. Add 100 µL transfection solution to each well

8. Incubate overnight.

9. Visualize transfection efficiency on a fluorescence microscope (Figure A.I.1). In HAECs, mRNA transfection is noticeably less efficient than using adenovirus (Figure A.I.1) but still useable from a data acquisition standpoint. Too little mRNA and fluorescence is not enough, but too much mRNA causes cell death.

Critical: mRNA must be kept on ice to minimize mRNA degradation. mRNA should be aliquoted so that each aliquot isn't thawed more than twice.

Note: mRNA transfections can be further optimized for your cells by a dose titration. We typically try a range of 25-200 ng/cm^2.

Plate cells into imaging chambers - Day 2

Timing: 1 hour

For ease of solution switching, cells must be plated into Ibidi flow chambers. However, this environment is slightly hypoxic with a smaller volume than traditional cell culture plates so cells must have media changes every 24 hours (Figure A.I.2).

10. Warm PBS, TrypLE, and cell media in 37 °C water bath

11. For adherent cells, wash cells twice with PBS and remove by aspiration.

12. Add TrypLE to virally transduced cells (50 µL per 12-well), incubate for 2 min at 37 °C and 5% CO_2
    a. Check for adequate detachment after 1 min, can tap dish to mechanically dislodge cells
    b. When 80% cells have detached, halt trypsinization by adding at least 3× volume complete media
13. Spin cells down at 900 g at room temperature and resuspend to 75,000 cells/50 µL (for Ibidi 6-well plate) complete media
    a. Tip Ibidi plate and add 50 µL into the elevated port, pipetting as close to the plate as possible, to ensure the cells spread between ports, incubate for 20 min at room temperature in the sterile hood.
    c. Add 60 µL complete media to each port to prevent drying
14. Incubate overnight to ensure attachment

Critical: When plating cells, make sure the solution of suspended cells is adequately mixed. This will ensure the sample number of cells make it into each well and therefore the cells will be at the same density. We note changes in cell density may have an effect on their metabolism.

Prepare Injection Solutions - Day 3

Timing: 15 min

Pharmacological perturbation requires two solutions which must be made fresh before each experiment. Since Laconic measures glycolysis, it is important to block any mitochondrial consumption of pyruvate which is accomplished with rotenone. Nigericin is an ionophore used to clamp the intracellular pH.

15. Warm Fluorobrite media and ICB in 37 °C water bath.
16. Thaw stock solution of pCMBA and nigericin on ice.
17. Mix calibration curve solutions via dilution series (Table A.I.2; Example calibration curve, Figure A.I.3).
    a. Make 10 µM nigericin and 2 µM of rotenone in 10 mL of ICB
    b. Use stock solution of lactate to generate 2 mL of 10 mM lactate
    c. 10-fold Dilution series from 10 mM to 0.0001 mM (dilute 6x) with each solution at 1 mL final volume in ICB with rotenone and nigericin
18. Mix MCT blockade solution for LPR (lactate production rate) assay (Table 3)
    a. 500 µM pCMBA in Fluorobrite with glucose or ECB with glucose, 1 mL per well of cells
    b. Bring 1 mL of Fluorobrite or ECB per well to wash cells prior to imaging

Note: Calibration curve only needs to be performed once. When performing LPR calibration curve can be omitted (step 23).

Pause Point: Solutions can stay at room temperature for up to an hour.

Perform imaging of intracellular lactate or lactate production rate (LPR) – Day 3

Timing: 2-3 hours

Injection of solutions and data acquisition at the microscope. This section can be used with any data acquisition, including calibration curve of intracellular lactate and measurement of intracellular glycolysis (lactate production rate, LPR). Calibration curve only needs to be performed once.

19. Turn on light source, microscope, computer, imaging software (such as Micromanager), and additional controls such as stage, CO_2, and temperature. Wait at least 1 hour for the microscope to thermally stabilize.

20. Serum starve the cells in the Ibidi plate prior to imaging

    a. Warm imaging solution (Fluorobrite or ECB) to 37 °C

    b. Replace complete media in Ibidi plate containing cells with imaging solution

        i. On the left port of the Ibidi plate, remove 90 μL of media. To the right port, add 90 μL of imaging solution. Perform 3 exchanges in total to completely remove the complete media.

    c. Incubate for at least one hour prior to imaging at 37 °C

21. Wash the tubing with at least 5x volume with a 10 mL syringe filled with PBS then assemble imaging chamber.

    a. Connect input port before output port.

        i. After the final rinse, inject imaging solution (Tables 2 and 3) into the input line using a needle and 1 mL syringe through the in-line injection port, holding the male elbow connector end at the same height as the injection port in order to ensure the entire tubing contains imaging solution liquid before adding the cap (Figure A.I.2). Capping the input line to close the input port will prevent fluid from leaking out of the input line.

        ii. Fill the ports on the Ibidi plate with the imaging solution using a 200 μL pipette so that there is no air within the port.

        iii. Attach the input line first, press down firmly to ensure attachment. Then repeat attaching the output line.

    b. Ensure waste line is securely placed into waste container and that the input line is accessible without disturbing the imaging focus.

22. Set imaging parameters

    a. Exposure should be set to 100-200 ms at a frame rate of 1 frame/2 s in both donor and FRET channels to minimize photobleaching.

    b. Choose a representative field of view away from the injection port or multiple fields of view if you have stage control

23. Start imaging with injections

    a. Attach a 25g needle to a different 1 mL syringe, used for injecting drugs

        i. Pull liquid up into the syringe slowly to avoid bubble formation

        ii. Flick syringe as needed to eliminate bubbles

        iii. Use a different needle/syringe for each subsequent injection

    b. Start imaging. Pause image acquisition if necessary to inject each subsequent solution. We perform this action slowly (1 mL over 5 sec) to avoid cavitation and bubble formation. If doing the intracellular lactate calibration curve, perform those injections in increasing lactate concentration. Otherwise, follow the injection protocol for LPR. See Tables 2 and 3 for defined solutions.

    c. Acquire at least 2 min of data after each injection.

24. At the end of the assay, dispose of the cells unless using them for further analysis.

    d. Wash the tubing 3× with 10x volume using 70% ethanol

25. Transfer data and turn off imaging equipment

Critical: The complete media contains growth factors that can activate the cells, thus changing their metabolism. Therefore, cells must be starved for at least one and up to two hours prior to imaging.

Critical: Assembly requires attention to eliminating air bubbles. Additionally, if you connect the waste line first, you may pull liquid from the plate out, leaving the cells dry and the plate susceptible to bubble formation. If a bubble is injected into the imaging chamber, cells could be ripped off the plate.

Note: To prevent bubble formation, place Ibidi chamber and tubing in incubator for 10 min prior to starting injections to bring everything to the same temperature. Make sure all solutions are at 37 °C.

Note: Exposure time will be dependent on the expression level, light source strength, objective, and camera sensitivity. We suggest that the histogram of intensities fills at least ¼ the dynamic range of the camera.

Note: After each injection, check focus to ensure that there has not been any focus drift.

Troubleshooting: Low expression level of Laconic

Troubleshooting: Elongated cells

Troubleshooting: Injection causes cells to detach

Troubleshooting: Injection causes focus change

Pause Point: Data can be analyzed at any time.

Construct deep learning network for semantic segmentation

Timing: 3-7 days, depending on size of data set, computer memory and speed

For successful discrimination of metabolic subpopulations, accurate cell segmentation is critical. We therefore employed semantic segmentation for endothelial cells which have complex morphology. One increasingly powerful method for rapid segmentation is the use of artificial intelligence which has achieved human-level performance (Ronneberger et al., 2015). A subset of AI is deep learning, in which convolutional neural networks are used to perform recognition tasks, where many of the rules governing object assignment are hidden, as opposed to rule-based segmentation where all rules must be *a priori* explicitly laid out. For accurate Deep Learning to perform semantic segmentation, having a large ground truth dataset for network training is essential. A sample ground truth dataset can be downloaded at (Harrison, Devin et al., 2021), ground truth_v2.zip. Code for this section can be downloaded and followed along at: https://github.com/wulab-code/STAR_methods. Please open "code_testing_new.m" for sample code. Be sure all scripts are in the same directory to eliminate path issues.

26. Generate ground truth dataset: Try to make conditions of ground truth dataset as close to how data will be taken so that the AI can do the least amount of guessing. Transfect with Laconic as above on a glass substrate such as Ibidi 8-well or Labtek 8 well to facilitate high resolution microscopy. The goal here is to generate microscopy datasets that will be easily labeled as cell body (using transfected Laconic), cell boundaries (using VE-CADH antibody), nuclei (with Hoechst dye), and background.

    e. Fix cells: After cells have grown to confluency and are appropriately expressing Laconic, wash cells with PBS at 37°C once and immediately fix using 4% PFA for 10 min at room temperature.
    f. After fixation, wash with PBS 3×, 5 min each, on a rocking platform at room temperature.
    g. Wash 3× with PBS, 5 min each, shaking, room temperature.
    h. Block with blocking buffer for 30 min at room temperature, shaking
    i. Primary antibody overnight 1:100 VE-CADH in blocking buffer on a rocking platform at 4°C.
    j. Wash with PBS 3×, 5 min each, shaking, room temperature.
    k. Secondary antibody: 1:1000 goat anti-rabbit 549 for 1 hour in blocking buffer at room temperature, shaking
    l. Wash with PBS 3×, 5 min each, shaking, room temperature.
    m. Stain nucleus: treat samples with 1:1000 Hoechst dye in PBS for 10 min at room temperature, then rinse with PBS once.

Pause Point: After cells have been fixed, they can be stored at 4 °C in PBS for imaging later. If the chambers are properly sealed (plastic wrap works well) then cells can be imaged months later. Mounting media can be added as a preservative and cells can be stored at 4 °C for years.

n. Take images at same magnification / settings as experiment, as many as possible – green channel which will see Laconic and label cytoplasm, red channel which will image VE-CADH and the cell boundary and blue channel which will image Hoechst and hence the nucleus of the cell.

Troubleshooting: Too much intracellular labeling of VE-CADH

27. Label ground truth images: After generation of ground truth data set (Harrison, Devin et al., 2021) now we have to label all the pixels in the ground truth images. There are many ways to do this, including by manual inspection, or with custom image segmentation software. One highly accessible approach is to use free, open-source software such as CellProfiler (Carpenter et al., 2006). CellProfiler can use the nuclei as seeds for the cells then use the gradient of Laconic towards the cell edge as a marker for the boundary of the cell.

    a. Download CellProfiler (Key Resources Table) and load images according to your folder and file structure

    b. Calculate the illumination function for your microscope. Use "CorrectIlluminationCalculate" function. Select the input image and name the output image. Calculate the Background image and do not dilate the objects in the final averaged image. Select a block size which is larger than the object (a cell); in this case, 150 is sufficient. Do not rescale the illumination function. Calculate the function based for each image. Smooth the background image with a Gaussian function.

    c. Perform background correction on all images. Use the "CorrectIlluminationApply" function to perform background correction. Select the input images (these are your original images) and name the output image. Use the illumination function calculated in step 27b. The illumination function should be subtracted from the input image.

    d. Identify primary objects (nuclei). Use the "IdentifyPrimaryObjects" function. Select input image for Hoechst based images. Enter the typical diameter of the object in pixel units. Discard objects outside the diameter range; discard objects touching the border of the image. Use an adaptive thresholding strategy with Otsu thresholding method, with three-class thresholding. Assign pixels in the middle intensity range to the foreground. Threshold smoothing scale and correction factor can be modified but default settings work. Choose adaptive window of 50 and distinguish clumped objects by shape. Use propagation method to draw dividing lines between clumped objects. Automatically calculate the size of the smoothing filter for declumping, automatically calculate the minimum allowed distance between local maxima, and speed up by using a lower-resolution image to find local maxima. Fill holes in identified objects after both

thresholding and declumping. Typically, this will result in detection of nuclei that are bigger than what is perceived by the user.

e. Shrink the nuclei. Use the "ExpandOrShrinkObjects" function. Select the input object for nuclei and shrink the objects by a specified number of pixels. This has to be eyeballed, but 3 is sufficient.

f. Now identify the cell bodies. Use "IdentifySecondaryObjects." Select input image for Laconic based images, and select the shrunken nuclei as the input objects. Select propagation as the method to be used to identify secondary objects. Use an adaptive thresholding strategy with Otsu thresholding method, with three-class thresholding. Assign pixels in the middle intensity range to the foreground. Threshold smoothing scale and correction factor can be modified but default settings work. Choose adaptive window of 50 and regulation factor of 0.05. Fill holes in identified objects and do not discard objects touching the border of the image.

g. Now identify cytoplasm. Use "IdentifyTertiaryObjects." Select the cell body objects from step 27f. Select the smaller identified objects (shrunken nuclei). And do not shrink smaller objects prior to subtraction.

h. Fill objects. Now that the cytoplasm has been identified, use "FillObjects". This function will fill in any unmarked cytoplasm, using a minimum hole size of 54 and planewise fill.

i. To create cell boundaries, shrink the cytoplasm by 1 using the "ExpandOrShrinkObjects" function.

j. Shrink the nuclei by 1 pixel using the "ExpandOrShrinkObjects" function.

k. Now using the shrunken cytoplasm, identify the cytoplasm object by using "IdentifyTertiaryObjects."

l. Now using the shrunken nuclei, identify the nuclei object by using "IdentifyTertiaryObjects."

m. Now using the cytoplasm with nuclei, identify the cytoplasm object by using "IdentifyTertiaryObjects" and smaller object is new shrunken nuclei.

n. Convert the following objects to image using "ConvertObjectsToImage" function: Filled cytoplasm, cytoplasm with nuclei, cytoplasm outlier, shrunken nuclei, shrunken nuclei_1 and shrunken cytoplasm

o. Save images to disk as Portable Network Graphics (png) using "SaveImages" function. The rest of the protocol assumes that images are saved in png format.

28. Construct deep learning algorithm using the Deep Learning toolbox in MATLAB: MATLAB is advantageous in that minimal computer programming is required. Smallest feature size will determine how many convolutions you need to perform. The idea is to use deconvolutions to increase the receptive field for each neuron and then localize where the neurons fire using upconvolutions. Finally, an inverse weight function will be used to account for non-uniform distributions of the pixel classes (background pixels are usually overrepresented, compared to

boundary, cytoplasm, and nuclei, and could therefore bias the network). The first part will involve creating a datastore and using augmentation to increase the effective size of the dataset. The second part involves creating the segmentation network and assessing its performance.

a. Download and install latest version of MATLAB with Deep Learning toolbox. Download the scripts from GitHub (Link to code). Open sample code "code_testing_new.m" in MATLAB.

   i. Create a new script. All code referenced below are in "code_testing_new.m" . The code is either directly shown below or referenced by line number. For each new line in the script, there will be a double arrow ">>" and can be typed directly into the script

b. This script assumes you are on a Windows PC. In this example, the "basedir" is the location of the ground truth images with are .png format files. This script also assumes that you are using MATLAB 2018b although the script should be compatible with newer versions.

```
>>  clear
>> addpath('C:\Program Files\MATLAB\R2018b\examples\images\main')
>> basedir = 'D:\images\';
>> ground_truth = 'D:\images\groundtruth';
```

c. Define classes.

```
>> classNames = ["background","border","cell","nuclei"];
```

d. Randomize into training and validation datasets. Pick the fraction of images you wish to use for training (frac_training), which the computer is blinded to when performing validation and testing. The script automatically divides the remaining non-training images into validation and testing evenly. A good starting point is 70% of images devoted to training.

```
>> num_images = 1000; % number of ground truth images
>> frac_training = 0.7;
>> [training, validation, testing] = ...
randomize_images(num_images,frac_training);
```

e. Make and store training, validation, and testing datasets into different directories: one for the labeled images and one for the images themselves

```
>> divide_images(...
basedir,ground_truth,training,validation,testing);
```

f. Create image and pixel datastore for training and validation.

```
>> imds = imageDatastore(fullfile(basedir,'training'),  ...
   'FileExtensions',{'.png'});
```

```
>> classNames = ["background","border","cell","nuclei"];
>> pixelLabelIds = [0 1 2 3];
>> pxds = pixelLabelDatastore(fullfile(basedir, ...
   'training_label'),classNames,pixelLabelIds);
>> imds_validation =  imageDatastore(fullfile(basedir,   ...
    'validation'),'FileExtensions',{'.png'});
>> pxds_validation =  pixelLabelDatastore(fullfile(...
 basedir,'validation_label'),classNames,pixelLabelIds);
>> pximds_validation = pixelLabelImageDatastore(...
    imds_validation,pxds_validation);
```

g. Augmentation can be used to increase the amount of data available to the network. Define augmentation function.

```
>> augmenter = imageDataAugmenter('RandRotation',[-180 180],...
  'RandXReflection',true,...
  'RandYReflection',true,...
  'RandXShear',[0 10],...
  'RandYShear',[0 10]);
```

h. Define patch extraction datastore

```
>> patchds = randomPatchExtractionDatastore(... imds,pxds,128,'PatchesPerImage',256, ... 'DataAugmentation',augmenter);
>> patchds_validation = randomPatchExtractionDatastore(...
  imds_validation,pxds_validation,128,'PatchesPerImage',256);
```

i. Preview the augmented patches

```
>> minibatch = preview(patchds);
>> montage(minibatch.InputImage,'DisplayRange',[0 255])
```

j. Create inverse weighting function.

```
>> tbl = countEachLabel(pxds);
 >> totalNumberOfPixels = sum(tbl.PixelCount);
 >> frequency = tbl.PixelCount / totalNumberOfPixels;
 >> classWeights = 1./frequency;
```

k. Generate graph of the network (Figure A.I.4). “numFilters” determines the number of channels in the output of the convolutional layer. “filterSize” is the size of the local regions that are convoluted and should therefore be matched to the smallest feature which in our case is a few pixels. 3 is the smallest filter size.

Lines 43-174

l. Set options for the training. These are trial and error, but below are some starting points.

```
>> initialLearningRate = 0.05;
>> maxEpochs = 50;
>> minibatchSize = 16;
>> l2reg = 0.0001;
>> options = trainingOptions('sgdm',...
'InitialLearnRate', initialLearningRate, ...
'Momentum',0.99,...
'L2Regularization',l2reg,...
'MaxEpochs',maxEpochs,...
'MiniBatchSize',minibatchSize,...
'VerboseFrequency',20,...
'LearnRateSchedule','piecewise',...
'LearnRateDropFactor',0.1, ...
'LearnRateDropPeriod',20, ...
'Shuffle','every-epoch',...
'Plots','training-progress',...
'GradientThresholdMethod','l2norm',...
'CheckpointPath',fullfile(basedir,'checkpoint'),...
'GradientThreshold',0.05, ...
'Verbose',true, ...
'ExecutionEnvironment','multi-GPU');
```

m. Train algorithm and save the network (Figure A.I.5). This can take anywhere from overnight to 1 week depending on the speed of your computer. You should see the accuracy increase and the loss decrease as the training attempts to converge. Accuracy should be above 80% and loss should be below 1 to have acceptable results.

```
>> [net,info] = trainNetwork(patchds,lgraph2,options);
```

```
>> save network.mat net
```

Critical: We suggest imaging at least 20,000 cells for deep learning but any additional images will help. Only 70% of images will be used for training. The remaining 30% will be split evenly for validation and testing of the deep learning network.

Alternative: Although we did not specify in the Cellprofiler section (27), it is possible to use the VE-CADH signal as the boundary and the Laconic and Hoechst signal as markers for the cell body and nucleus when labeling cells for ground truth.

Note: If the computer runs out of memory, try reducing the minibatch size. If the learning rate is not fast enough, adjust the momentum, LearnRateDropFactor and LearnRatePeriod. While these are good starting points, this is entirely trial and error. Typically, the accuracy should increase almost immediately in an upward trajectory from 0 to 60% within one 50 iterations with slow improvement afterwards. While the speed of calculation depends ultimately on the amount, quality of data, and computer specifications, a typical run on a fast computer with 3 GPUs (c. 2018) takes 48 hours.

Alternative: It may be possible to use transfer learning using a published network to avoid creating one's own deep learning network.

Troubleshooting: Deep learning accuracy does not reach above 80%

Troubleshooting: MATLAB code has difficulty executing

Pause point. As this all takes place in a computer, resuming can happen at any time.

Semantic segmentation

Timing: [4 hours - days], depending on computer memory and speed, and size of dataset

29. Pre-processing images after imaging Laconic. Pre-processing images is important to remove imaging artifacts such as vignetting or uneven illumination, in order to have the best performance (assuming that the ground truth dataset is ideal). The network will likely perform well on unoptimized images as well. One can in theory test this under quantification and statistical analysis below. It is possible to take experiment images and process them first in Cellprofiler, but here we opt to use MATLAB so that everything is "one-click". The first step is to eliminate vignetting and uneven illumination, using a tophat filter. However, to specify filter properties, one needs to know the imaging properties of the microscope. Start a new script. Specify the camera and magnification parameters including pixel size (in real space). Specify the approximate size of a cell. A good rule of thumb is to make the tophat filter about 3× the size of a cell (Crocker and Grier, 1996). Specify the expected input image size for the network and bit depth. Make sure that the image size and bit depth are the same as that which was used in creating the deep learning network above (here, the image size was 1200x1200 and the bit depth was 8 bit).

```
>> pixel_size = 11e-6;
```

```
>> magnification = 10;
>> cellsize = 11e-6;
>> tophatw = 3*round(cellsize/(pixel_size/magnification));
>> h = fspecial('disk',tophatw);
>> thresh = 0;
        >> targetimsize = [1200 1200];
    >> targetbitsize = 8;
```

a. Resize image and use tophat to get rid of long wavelength intensity fluctuations where venusimage and tfpimage are the files of the Venus image and a tfp image, respectfully, although in principle it doesn't matter.

```
>> venusimage = 'venus.tif';
>> cfpimage = 'tfp.tif';
>> [venus_orig tfp_orig thresh_venus thresh_tfp] = ...
 resizetophatim(venusimage,tfpimage,...
 targetimsize,h,thresh,targetbitsize);
```

30. Perform semantic segmentation of images: It doesn't matter if you do it on the background corrected Venus image or mTFP image. Here it is done on the Venus image

a. Load the network:

```
>> segnet = load('network.mat');
```

b. Segment the image. It is much faster with a GPU than using a CPU.

```
>> output = semanticseg(venus_orig,segnet.net,...
  'ExecutionEnvironment','GPU');
```

Post-processing of images

Timing: [hours – overnight], depending on computer memory and speed, and size of dataset

31. Post-processing after semantic segmentation: The output is a categorical array (1-4). The segmentation needs to be cleaned up as artifacts can be introduced. This script filters out small cells and small nuclei and saves the output. Convert the output image to a labeled image (see Figure A.I.6 for example of original image, after semantic segmentation, and after additional post processing). See how well the segmented image compares to the original.

```
>>  [filtered_image filtered_nuclei] =   filter_network_output(output);
```

```
>> bw_filtered_image = bwlabel(filtered_image);
>> bw_filtered_nuclei = bwlabel(filtered_nuclei);
>> figure
>> output_im = double(output);
>> bw_im = double(bw_filtered_image);
>> venus_im = imread(venusimage);
>> J = imadjust(venus_im,stretchlim(venus_im),[]);
>> [X2]= output_im/max(output_im(:));
>> [X3]= bw_im/max(bw_im(:));
>> map = jet;
>> subplot(1,3,1)
>> imshow(J)
>> title('Contrast adjusted Venus image')
>> subplot(1,3,2)
>> imshow(X2,'Colormap',map)
>> title('Semantic segmentation')
>> subplot(1,3,3)
>> imshow(X3,'Colormap',map)
>> title('Additional filtering')
```

32. Decompose the segmented image into individual cells: The images have been segmented, but each pixel in each image is just now a number – 1-4 indicated background, cell boundary, cytoplasm, and nuclei. The cells have to be individually identified, which is the purpose of this part. Using parallel processing significantly speeds up the time required.

```
>> expand = 3; % target cell expansion
>> venusresize = imresize(imread(venusimage),targetimsize);
>> tfpresize = imresize(imread(tfpimage),targetimsize);
>> imdata = cell_decomposition(bw_filtered_image,...
   bw_filtered_nuclei,venusresize,tfpresize,expand);
```

33. Above, everything was done on one single image. Now we will put it into a loop using parallel processing. Place all variables that don't change outside the loop. We recommended that you use GPUs to do semantic segmentation first, then use regular CPUs (in parallel) for the rest.

Use the demo_images.zip located here (Harrison, Devin & Wu, David et al., 2021). Unzip them into a directory titled “demo_images”.

a. First loop the part that requires GPU

   Lines 227-248.

b. Next loop the part that requires CPU

   Lines 250-278.

Note: A sample data set (in addition to the one referenced explicitly in the code above) is located with corresponding figures at (Wu, D. & Harrison, D. et al., 2021) . We recommend using the dataset corresponding to Figure 1e. Sample 1 is control and sample 2 is with DMOG. Injections for pCMBA occur at frame 120.

Link cell trajectories

Timing: 15 min

34. Linking together cell trajectories: Now that all images have been segmented, the next task is to link the intensities of each cell into a trajectory which is accomplished below by creating a matrix of cell positions and finding the nearest cell in an adjacent image. Save the output.

```
>> input_directory = 'singlecell_output';
>> [venus tfp venus_bg tfp_bg linkage] = ...
        cell_linking(input_directory,targetimsize);
>> output_directory = 'singlecell_links';
>> mkdir(output_directory);
>> save(fullfile(output_directory,'linkvenus.mat'),'venus');
>> save(fullfile(output_directory,'linktfp.mat'),'tfp');
>> save(fullfile(output_directory,'linkvenusbg.mat'),'venus_bg');
>> save(fullfile(output_directory,'linktfpbg.mat'),'tfp_bg');
>> save(fullfile(output_directory,'linkage.mat'),'linkage');
```

Analysis of data

Timing: 30 min

Now that the experiment is complete, we need to analyze the data and calculate the rate of intracellular glycolysis or the lactate production rate (LPR). To obtain the LPR, calculate the slope of the mTFP/Venus signal (the lactate signal) over a 40 s trajectory and fit it against a linear model during the portion of the time the cells were exposed to MCT1 inhibitor according to the following equation (Equation 1):

35. Load the linked trajectories: At this point the segmented images in each channel (mTFP, Venus) have been linked through time in "linktfp.mat", "linkvenus.mat" which contains the mean intensity of the segmented cell in each respective channel. Background of the channels have been saved in "linktfpbg.mat" and "linkvenusbg.mat". These are loaded by selecting the appropriate directory and subdirectory containing the linked files:

```
>> load(fullfile(output_directory,'linktfp.mat'));

>> load(fullfile(output_directory,'linkvenus.mat'));

>> load(fullfile(output_directory,'linktfpbg.mat'));

>> load(fullfile(output_directory,'linkvenusbg.mat'));
```

36. Calculate the inverse FRET ratio. Inverse FRET ratio is calculated by dividing the mTFP by Venus, which were determined from the total cytoplasmic intensity. One can also check the background doesn't contribute significantly to the (inverse) FRET signal by calculating the FRET of the background. Each row of the "fret" or "fret_bg" matrix is the single cell inverse FRET ratio (Figure A.I.7).

```
>> fret = tfp./venus;

>> fret_bg = (tfp-tfp_bg)./(venus - venus_bg);
```

37. Load the image data and set the LPR calculation over 40 s: Next, we calculate the LPR by fitting the rate of increase in mTFP/Venus signal over 40 s specified by dist (here, dist = 20 since we took 1 frame every 2 s).

```
>> imdata = load(fullfile('singlecell_output', ...

[zerostr(5,0) '_data.mat'])); % load image data for the first image

>> dist = 20;
```

38. Calculate the LPR for each solution change. Iterate through the fret variable, which is a matrix containing in each row the average fret value of a cell, and in each column the fret value of that cell as a function of time. The signal is filtered with a median filter of width 5. We look for changes in solution that tells us when to start calculating the slope. Keep on looking for changes in solution until you have run out ("solution_changes", specified *a priori*). Fit the relevant data with a line and calculate the slope. Save this variable. In this example (from the demo images dataset), solutions were injected in frame 150 (glucose) and frame 300 (glucose and pCMBA).

```
>> solution_changes = [150 300];

>> clear slope gof_r2 cellsize cells
```

```
>> for i = 1:size(fret,1)
        mfret = medfilt1(fret(i,:),5);
        % find minimum point for each solution change
        for h = 1:length(solution_changes)
          if h ~= length(solution_changes)
            vec = mfret(solution_changes(h):solution_changes(h+1));
          else
            vec = mfret(solution_changes(h):length(mfret));
          end
          idx = find(vec == min(vec));
          if h == length(solution_changes)
            if length(mfret)-(solution_changes(h)+min(idx)) < dist
              idx = 1;
            end
          end
          x = solution_changes(h)+min(idx)-1;
          [fitobj gof] = fit((x:x+dist)',mfret(x:x+dist)','poly1');
          slope(i,h) = fitobj.p1;
          gof_r2(i,h) = gof.rsquare;
        end
      end
```

39. Now go through the fitted slopes and filter it for fit slopes that have an R^2 value that is high enough to ensure that the fit parameters correspond will with the data (specified by "filter" parameter). In our hands, R^2 values > 0.8 are sufficient. Here, the slope has been fit into another variable.

```
>> filter = 0.9;
>> slope_n(1).slope = [];
>> for m = 1:length(slope (1,:))
   c = 1; % counter
   for i = 1:size(slope,1)
```

```
        if gof_r2(i,m) > filter
            slope_n(m).slope(c) = slope(i,m);
            slope_n(m).r2(c) = gof_r2(i,m);
            slope_n(m).index(c) = i;
            c = c+1;
        end
    end
end
```

40. At this point, save the results in a file.

```
>> save results.mat slope_n
```

41. The LPR can be plotted either in MATLAB or another plotting program. The factor 0.01221 is the slope of the semilog change in lactate, as generated from the calibration curve (Figure A.I.3), divided by the inverse frame rate (Equation 1). Sample data for Laconic calibration can be downloaded from (Wu, David et al., 2021), FigureED1a. Injection times for different concentrations of lactate during calibration process are available here (Harrison, Devin et al., 2021).

```
>> glucose = slope_n(1).slope /0.01221);
>> lactate = slope_n(2).slope /0.01221);
```

42. Inspect a good trace (Figure A.I.7 demonstrates a single cell trace of 1/FRET):

```
>> plot(fret(slope_n(2).index(50),1:450),'k.')
>> text(150,0.6075,'\leftarrow Glucose injection')
>> text(300,0.6075,'\leftarrow pCMBA injection')
>> xlabel('Frame')
>> ylabel('1/FRET')
```

Optional: Instead of calculating LPR (step 37), one can also directly compute the intracellular lactate concentration if there is a permeabilization step used as a reference (as for determining the inverse FRET/lactate calibration).

Troubleshooting: Low number of useable FRET traces

A.I.6 Expected outcomes

This protocol allows the user to use deep learning to perform semantic segmentation of cells, dividing images of cells into nucleus, cytoplasm, cell boundary, and background. This data is all saved in .mat files on the hard drive and be easily used in other downstream applications or analysis. This deep learning strategy for segmentation can easily be applied to difference cell types. This method of semantic segmentation is agnostic to Laconic and can be used in different cell labeling situations.

Generally, users should expect to generate FRET traces for hundreds of cells per field of view. Each individual trace is a time-series record of intracellular FRET. After the microscope system is calibrated, it is possible to map the FRET values to obtain absolute values of intracellular lactate. With knowledge of when the different compounds were injected, users can also calculate the lactate production rate, or glycolytic rate of individual cells. This protocol can be easily adapted to inspect the cell morphology and correlate it to LPR, for example, or to use in different cell types.

Here, we specifically demonstrate the LPR of a sample of HAECs treated with 500 μm DMOG and with vehicle (DMSO) overnight (Wu et al., 2021). DMOG stimulates HIF-1a which increase glycolysis. LPR was calculated as above and exported to Prism (Figure A.I.8).

A.I.7 Quantification and statistical analysis

Network performance estimation

There are many ways to estimate the error in machine learning or deep learning networks. Errors can be calculated for each class and a composite score can be calculated. Each estimation or error has its own positives and negative attributes, as error estimation is ultimately a little bit subjective, as one needs to choose which statistics to focus on. Common estimates of errors include the Matthew's Correlation Coefficient, Global accuracy, Class specific accuracy, Boundary F1 score, precision, recall and the Dice score. Examples on how to calculate each below.

1. Save the network and run a test to see how accurate it is. It is important to only perform analysis on non-training data otherwise one will get artificially inflated scores. Calculate the global, class specific accuracy, and boundary F1 score.

   Lines 358-370.

2. Calculate standard deviation.

   Lines 380-414.

3. Calculate Matthews Correlation Coefficient where TP = true positive, TN = true negative, FP = false positive, FN = false negative.

Lines 372-377.

4. Calculate precision where TP = true positive, FP = false positive

Lines 419-422.

5. Calculate recall where TP = true positive, FN = false negative.

Lines 426-429.

6. Calculate the Dice score

Lines 434-449.

a. Calculate the mean Dice score for each class

Lines 451-454.

b. Calculate the standard deviation of the Dice score for each class

Lines 456-459.

Image segmentation error estimation

To estimate the error in deep learning assisted semantic segmentation, we first compute the error between ground truth fluorescence and segmented fluorescence. We use a test data set of cells expressing Laconic for which we have ground truth and segmented these images with the deep learning algorithm. Then using the same image analysis pipeline, we plot the cell fluorescence as estimated from deep learning networks against the ground truth cell fluorescence (n ~ 20,000 cells) (Figure A.I.9).

```
>> output_directory = 'network_test';
>> imds = imageDatastore(fullfile(basedir, 'testing'));
>> pxdsTruth = pixelLabelDatastore(fullfile(...
        basedir, 'testing_label'),classNames,pixelLabelIds);
>> pxdsResults = pixelLabelDatastore(output_directory, ...
        classNames,pixelLabelIds);
>> n_images = 65;
>> [cell_intensity_truth_total,cell_intensity_DL_total] =...
 evalTotalError(imds,pxdsTruth,pxdsResults,n_images,targetimsize);
>> save('error_estimation.mat', ...
        'cell_intensity_truth_total','cell_intensity_DL_total');
```

```
>> x = cell_intensity_truth_total';
>> y = cell_intensity_DL_total';
>> [fitobj gof] = fit(x,y,'poly1');
>> plot(cell_intensity_truth_total,cell_intensity_DL_total,'kx')
>> hold all
>> xax = linspace(min(cell_intensity_truth_total), ...
        max(cell_intensity_truth_total),100);
>> plot(xax,fitobj.p1*xax +fitobj.p2 ,'r-','LineWidth',2)
>> xlabel('Ground truth fluorescence')
>> ylabel('Computed fluorescence')
>> text(60,120,['y = ' num2str(fitobj.p1) ' + ' num2str(fitobj.p2)])
>> hold off
```

Total LPR error estimation

To calculate the total estimated error in LPR, from semantic segmentation to LPR slope calculation, we turn to Monte Carlo simulations of LPR (bootstrapping). Using a dataset which provides a real measure between ground truth and fluorescence, we generate a line by randomly sampling a ground truth fluorescence and its corresponding deep-learning generated fluorescence, 100 times. The slope of this line (ground truth vs. deep-learning) is then calculated by performing linear regression. This random sampling of fluorescence values, followed by slope calculation, simulates LPR calculation in real samples. The distribution of these bootstrapped slopes is plotted after repeating this 10,000 times, resulting in a Gaussian distribution of slopes (Figure A.I.10).

```
>> bootstrap_slope = [];
>> for i = 1:10000
    idx = randi([1 length(cell_intensity_truth_total)],1,100);
    x = cell_intensity_truth_total(idx);
    y = cell_intensity_DL_total(idx);
    fitobj = fit(x',y','poly1');
    bootstrap_slope(i) = fitobj.p1;
   end
>> h = histogram(slope);
```

```
>> x = ((h.BinEdges(2:end) - h.BinEdges(1:end-1))/2) + ...
        h.BinEdges(1:end-1);
>> y = h.Values;
>> [curve fitobj gof] = fit(x',y','gauss1');
>> histogram(slope)
>> hold all
>> plot(curve)
>> text(0.2,750,['y = ' num2str(curve.a1) ...
        '*exp(-((x-' num2str(curve.b1) ')/' num2str(curve.c1)')^2)'])
```

A.I.8 Additional controls

Estimation of bleed through in microscope filter sets

Bleed through in FRET occurs when excitation of the acceptor occurs at the wavelengths used to excite the donor, leading to acceptor emission that does not occur due to FRET (acceptor bleed through). Similarly, donor fluorescence can be detected in the acceptor channel (donor bleed through), artificially inflating FRET. A simple way to estimate degree of bleed through is to transfect cells with either mTFP or Venus without its pair and perform imaging as if imaging FRET. Then transfect cells with Laconic and image using the same parameters as those with mTFP and Venus alone. Compare the average signal level in minimal levels of lactate (maximal FRET) of each condition (mTFP alone, Venus alone, and Laconic).

1. To estimate the bleed through in the filter sets, create mRNA transcripts for mTFP and Venus separately (the FRET pair in Laconic).

2. Generate PCR templates for mTFP and Venus using Laconic plasmid.
   a. Generate template for *in vitro* transcription of mTFP via PCR using the T7-F and mTFPr primers (see Key Resources Table) and protocol listed in Table 1 and NEB Q5 Polymerase. The annealing temperature should be 60 °C and the extension time is 25 s.
   b. Generate template for *in vitro* transcription of Venus via PCR using the T7-Venus and BGH-R primers (see Key Resources Table) and protocol listed in Table 1 and NEB Q5 Polymerase. The annealing temperature should be 60 °C and the extension time is 25 s.
   c. Purify PCR products using QIAquick PCR Purification Kit (Link to manufacturer's protocol)

Note: PCRs can be checked by running on a 1% agarose gel for the correct amplicon size (853 bp for mTFP and 890 bp for Venus).

3. Create mRNA of mTFP and Venus

   a. Using the PCR-generated templates from 2c, create mRNA using mMESSAGE mMACHINE™ T7 ULTRA Transcription Kit (Link to manufacturer's protocol)

   b. After cleaning and eluting mRNA, aliquot (100 ng/µL) and store at -80 °C for minimal degradation. (Link to manufacturer's protocol)

4. Transfect cells with mTFP, Venus, and Laconic as in mRNA transfection of Laconic above.

5. Image each fluorophore using the FRET filter sets after starving cells in glucose free ECB for at least 1 hour.

6. Compare donor channel and acceptor channel for all three transfections. The amount of donor bleed through (imaging mTFP transfection alone in the acceptor channel) and acceptor bleed through (imaging Venus transfection alone in the acceptor channel) can be subtracted from the donor and acceptor channels imaged using Laconic. We found using the filter sets and illumination light source in this protocol that bleed through was not greater than 5% of the Laconic signal, thus not affecting the calculated FRET.

A.I.9 Limitations

Use of pCMBA will be toxic to the cells so if cells are needed following the assay, Phloretin can be used instead but should be washed out immediately following imaging. Injections of bubbles can ruin experiments. Segmentation can only be optimized by acquiring the right annotated training data. Environmentally controlled imaging chamber is ideal but not completely necessary—this would require careful attention to pH of buffers.

A.I.10 Troubleshooting

Problem 1: Low expression level of Laconic

When selecting a field of view for performing imaging, you may notice low expression or heterogeneous expression such that each field of view minimizes the number of usable cells or data points. Additionally, the exposure time may have to be increased in order to boost your signal.

Potential Solution: Dose titration of mRNA or virus

If expression levels are consistently low, we recommend dose titrating the mRNA or virus. If the expression levels are low for one or two experiments, consider changing aliquots. Both the Laconic mRNA and adenovirus must be kept at -80°C for storage and freeze-thawed no more than twice. Adequate signal must be present to achieve accurate measures of intracellular lactate level. This

can be tested by dose titration of mRNA or virus and performing intracellular lactate calibration (Figure A.I.3). Some heterogeneity in cellular fluorescence is expected but, in our experience, does not affect intracellular lactate measurement as long as there is enough signal to noise.

Problem 2: Low number of useable FRET traces

After processing imaging data with what appears to be hundreds of cells and adequate signal, only a few traces (out of hundreds) have the requisite R^2 for statistical testing.

Potential Solution: Ensure the ECB is at the correct pH

The pH of the ECB could change after sitting in the 37 C, 5% CO2 incubator for too long, since it is a bicarbonate based buffering system. Store ECB in an open container in a 37 C, 5% CO2 incubator for an hour in a small volume then measure pH. If the pH has changed substantially, make sure that the experiment is performed before this occurred. Alternatively, use Fluorobrite DMEM.

Problem 3: Too much intracellular labeling of VE-CADH

Occasionally, VE-CADH also stains the cell interior which will adversely affect cell boundary classification.

Potential Solution: Try alternative microscopy approach or modify Cellprofiler algorithm

If this is the case, either optimize staining with a different membrane marker, ~~n~~ or try confocal microscopy and image different focal planes. One can also in principle create in Cellprofiler a logical exclusion where overlap of VE-CADH and either Laconic or Hoechst causes VE-CADH to be deleted.

Problem 4: Elongated cells

When selecting a field of view for performing imaging, you may notice altered morphology of the endothelial cells. We note this occurs more often when using mRNA transfection versus adenoviral transduction (see Fig. 1).

Potential Solution: Adenoviral transduction

HAECs must not be used past passage 8. As the cells age, the morphology is more likely to change. We recommend using adenoviral transduction in lieu of mRNA if many experiments are to be performed for consistency of expression. Try avoiding using the same aliquot of defrosted cells for more than one month.

Problem 5: Injection causes cells to detach

Bubbles have been retained or formed in the imaging chamber or tubing.

Potential Solution:

Eliminate bubbles and make sure tubing and injection fluid is at the right temperature.

Bubbles may appear when the tubing is inserted into the Ibidi chambers. Flush the injection tubing thoroughly. Air may have been caught somewhere in the injection system. When attaching tubing to the chamber, make sure that no bubbles are entrained. When injecting, it must be done at a slow enough pace to not cause cavitation. Try reducing injection speed as well as to not dislodge any trapped air. Make sure all fluids are at the same temperature to prevent degassing.

Problem 6: Injection causes focus changes

After injecting solutions, focus is lost, likely due to rapid injection or accidental touching the microscope stage.

Potential Solution: Equilibrate the microscope at the right temperature

First, fix the sample tightly on the stage to prevent accidental movement. Make sure the microscope has thermally equilibrated – turn on the scope and stage top incubator for at least an hour prior to imaging. Finally, re-focus the sample quickly after injection prior to acquiring data.

Problem 7: Deep learning accuracy does not reach above 80%

Deep learning is unable to accurately semantically segment cells and properly classify pixels in an image.

Potential Solution: Ground truth is not accurate or there is not enough ground truth data.

Acquire more ground truth data. Carefully inspect the fixed samples and the output of Cellprofiler and check to make sure that classification is accurate.

Problem 8: MATLAB code has difficulty executing

Errors are returned at the command prompt.

Potential Solution: Make sure that the working directory is correct.

Make sure that the working directory is the same directory as with all the scripts. Check through the code to ensure that the directory referencing the location of images are correct.

A.I.11 Figures and tables

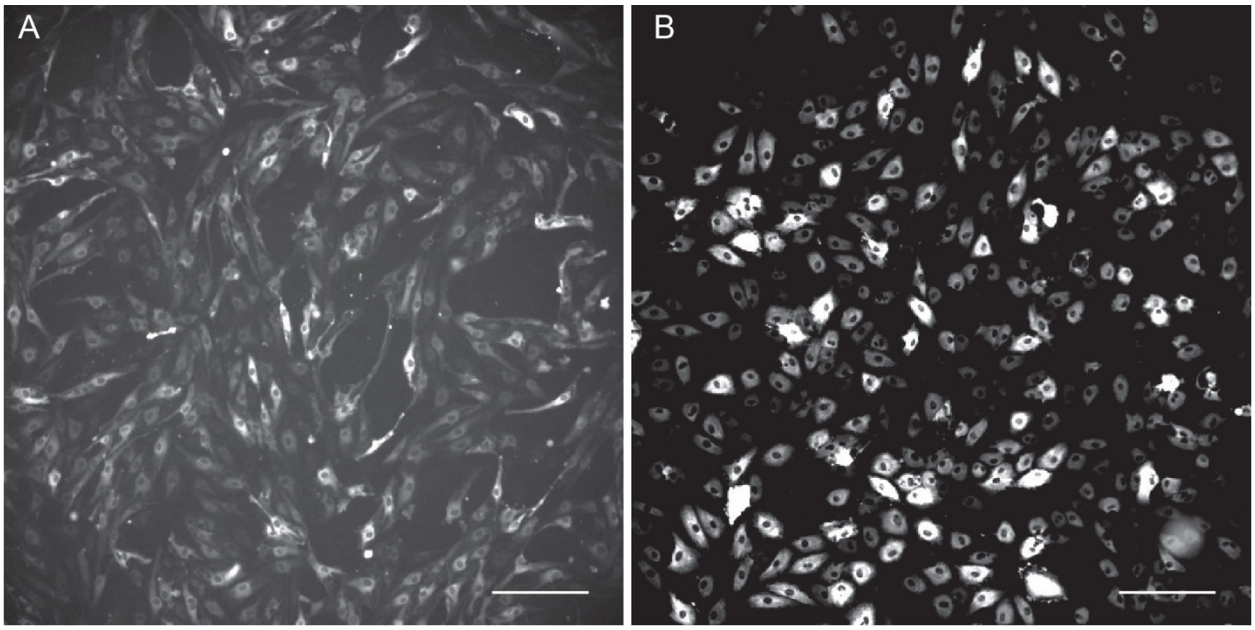


Figure A.I.1: Comparison of different methods of Laconic expression in endothelial cells

Comparison of mRNA versus adenoviral introduction of Laconic into human aortic endothelial cells after 48 hours. mRNA transfections can sometimes lead to cell elongation whereas transduced cells retain their original cobblestone-like morphology. Scale bars = 200 μm.

(A) 160 ng/cm^2 Laconic mRNA transfection.

(B) 50 MOI ad-Lac transduction.

Table A.I.1: Generating Laconic template for *in vitro* transcription

Forward (T7-F) and reverse (BGH-R) primers are used in the following PCR reaction in order to generate the template for *in vitro* transcription. PCR reaction steps are based on NEB Q5 Polymerase usage guidelines expecting a 2403 bp amplicon.

PCR cycling Conditions			
Steps	**Temperature**	**Time**	**Cycles**
Initial Denaturation	98 °C	30 s	1
Denaturation	98 °C	10 s	25-35 cycles
Annealing	63 °C	30 s	
Extension	72 °C	1.5 min	
Final Extension	72 °C	2 min	1
Hold	4 °C	Forever	

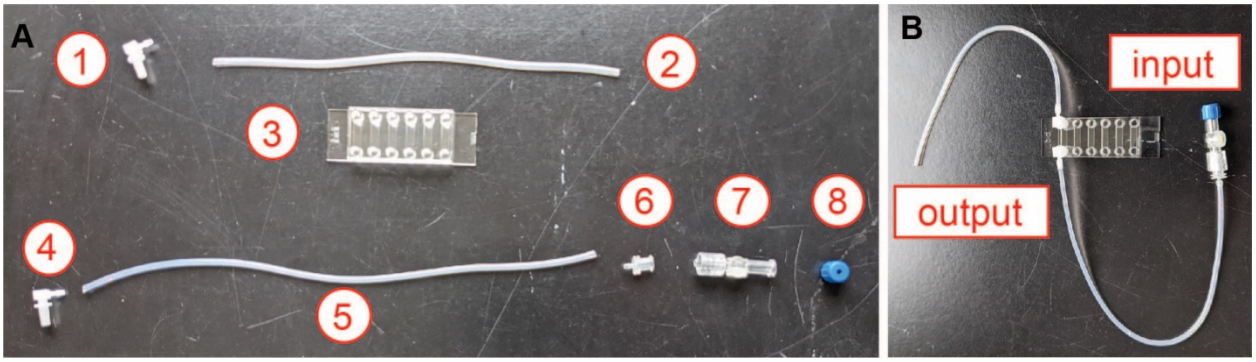


Figure A.I.2: Ibidi imaging chamber assembly

Components of the Ibidi imaging chamber are shown separated in (A) and assembled in (B).

(A) Male connector (1) is attached to tubing (2) to form the output or waste end of the apparatus which will connect to the Ibidi plate (3). Male connector (4) is attached to tubing (5) then to a female connector (6). The in-line injection port (7) is attached to the female end (6) to form the input or injection end of the apparatus. Following rinsing, the cap (8) must be added to close the input port. Once the input and output lines are assembled, they may be reused for multiple Ibidi plates.

(B) When performing imaging experiments, connect the input line before the output line into the bottom and top ports of one well in the Ibidi plate (3).

Table A.I.2: Solutions for calibration curve

Solutions for the calibration curve should be made the same day as imaging. Intracellular buffer (ICB) will be used as the solvent with varying concentrations of lactate in the presence of nigericin and rotenone for permeabilization. Lactate should first be serial diluted 1:10 5× then used to make to the following solutions.

Solution #	Component	Stock Solution	Final Concentration	Amount (µL)
1	ICB	1×	1×	988.6
	Rotenone	2.5 mM	1 µM	0.4
	Nigericin	10 mM	10 µM	1
	Lactate	1 M	10 mM	10
2	ICB	1×	1×	988.6
	Rotenone	2.5 mM	1 µM	0.4
	Nigericin	10 mM	10 µM	1
	Lactate	100 mM	1 mM	10
3	ICB	1×	1×	988.6
	Rotenone	2.5 mM	1 µM	0.4
	Nigericin	10 mM	10 µM	1
	Lactate	10 mM	100 µM	10
4	ICB	1×	1×	988.6
	Rotenone	2.5 mM	1 µM	0.4
	Nigericin	10 mM	10 µM	1
	Lactate	1 mM	10 µM	10
5	ICB	1×	1×	988.6
	Rotenone	2.5 mM	1 µM	0.4
	Nigericin	10 mM	10 µM	1
	Lactate	100 µm	1 mM	10
6	ICB	1×	1×	988.6
	Rotenone	2.5 mM	1 µM	0.4
	Nigericin	10 mM	10 µM	1
	Lactate	10 µm	0.1 mM	10

Table A.I.3: Example solution calculator for LPR injection solutions

Solutions should be prepared fresh on the same day as imaging. Extracellular buffer (ECB) or glucose-free Fluorobrite can be used as the solvent which should be warmed prior to solution preparation. If using glucose-containing Fluorobrite, glucose does not need to be added. The example calculations are dependent on 1 mL solution injections which should be adjusted depending on the length (and therefore volume) of the tubing.

Solution #	Component	Stock Solution	Final Concentration	Amount (µL)
1	ECB	1×	1×	990
	Glucose	1 M	10 mM	10
2	ECB	1×	1×	989
	Glucose	1 M	10 mM	10
	pCMBA	0.5 M	0.5 mM	1

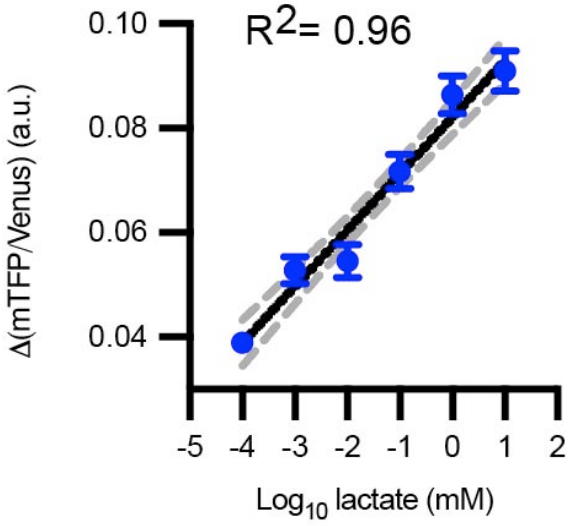


Figure A.I.3: Laconic calibration curve. mTFP/Venus (or 1/FRET) change is linearly correlated over 6 orders of magnitude of log lactate (n = 287 cells; black line is semilog fit with $R^2 = 0.96$, gray dotted lines are 95% confidence interval); error bars are SEM. Standard deviation of regression coefficients for R^2 for is 0.049.

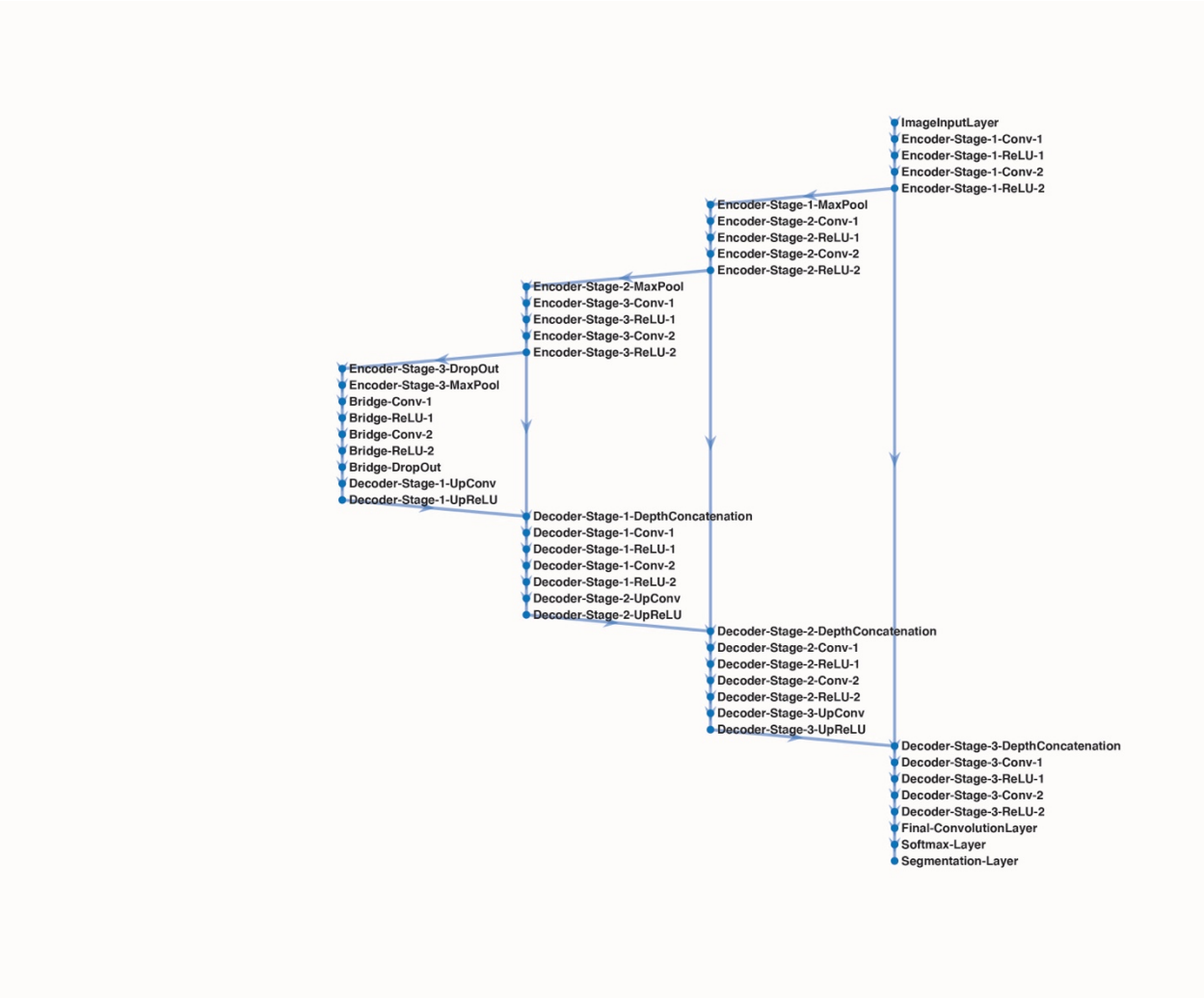


Figure A.I.4: Deep learning architecture for semantic segmentation.

Deep learning architecture for semantic segmentation, which consists of a contracting path (encoder) and an expansive path (decoder), forming a U-Net.

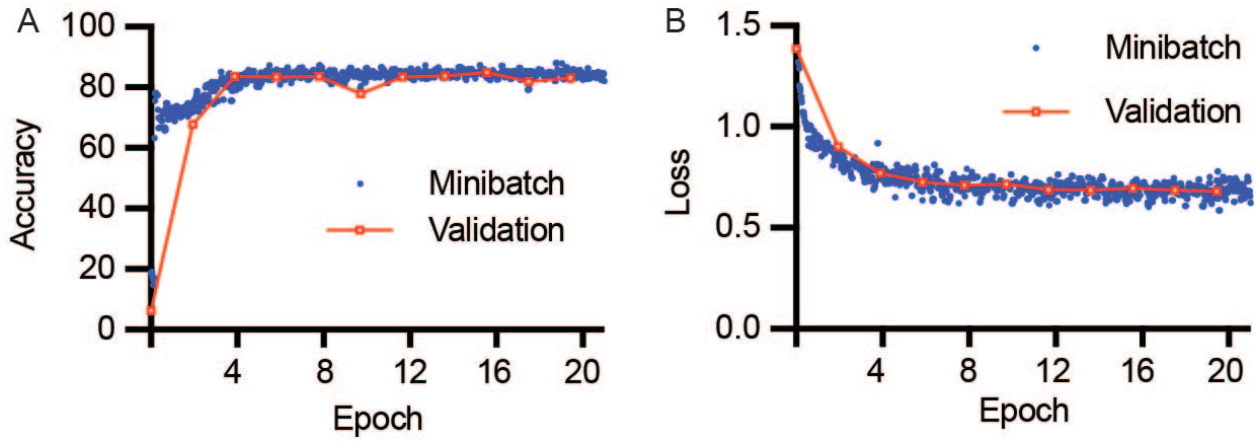


Figure A.I.5: Training and validation of the convolutional neural network. Accuracy (A) and loss (B) as a function of training epoch. Training was stopped when there was no further change to loss or accuracy.

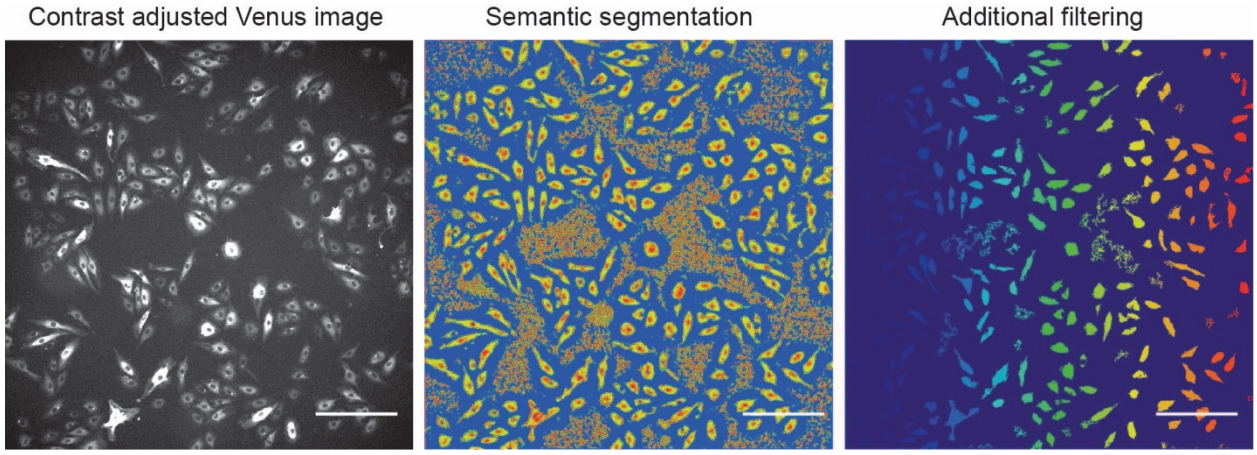


Figure A.I.6: Single field-of-view segmentation example. The contrast adjusted original Venus image (left) undergoes semantic segmentation (center) which classifies cell boundaries but must be filtered additionally to remove non-cell objects (right). Scale bar is 264 microns.

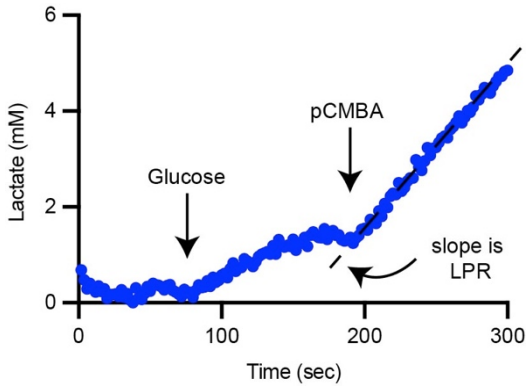


Figure A.I.7: LPR single-cell trace. Example of the 1/FRET trace of an individual cell during the LPR assay. Arrows indicate solution changes.

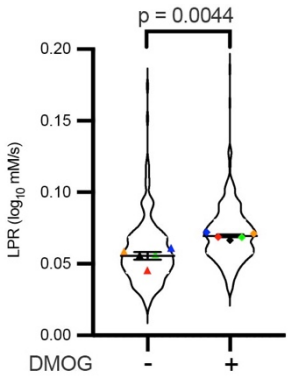


Figure A.I.8: LPR bulk data for distinguishable populations in HAECs treated with control vs DMOG. LPR assay was performed on vehicle DMSO-treated (–) or DMOG-treated (+) endothelial cells (n = 126 –, 71 +; 164 –, 226 +; 181 -, 221 +; 120 -, 262 +; 191 -, 234 +; for 5 biological replicates error bars are SEM).

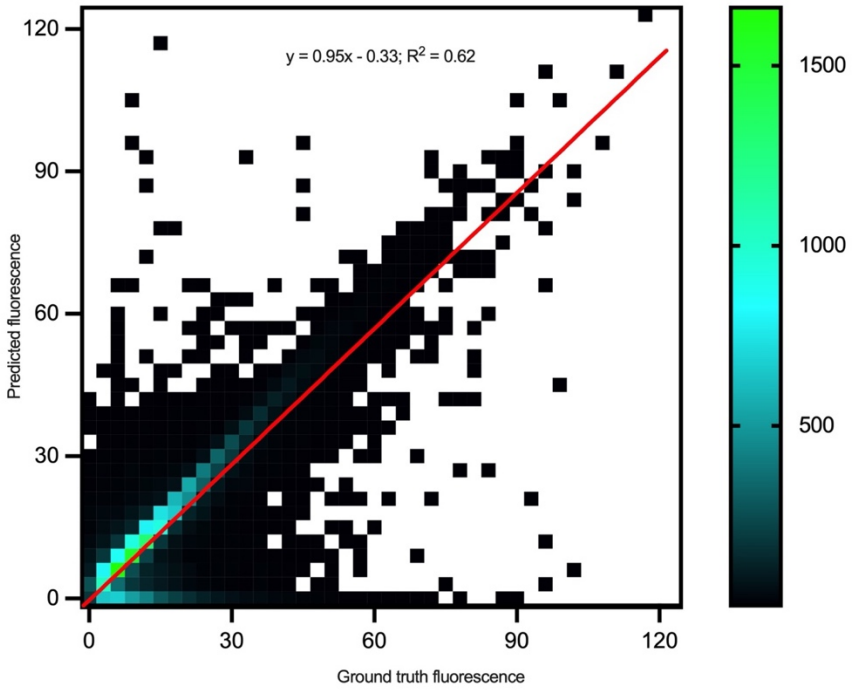


Figure A.I.9: Ground Truth Fluorescence vs. Predicted Fluorescence. To evaluate the performance of segmentation, computed fluorescence is compared to ground truth fluorescence, defined as the signal inside the cell boundary. In this example, there is a consistent underestimation of the total cell fluorescence. The color code indicates number of cells. Pure black indicates 1 cell. White indicates 0 cells. The red line is the fit between ground truth and predicted fluorescence. Fit equation and goodness of fit is inset.

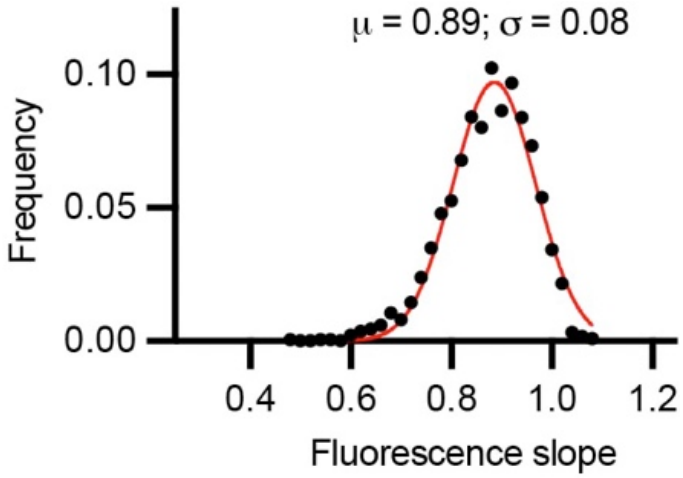


Figure A.I.10: Total quantification of LPR. Data from Figure A.I.9 were randomly sampled 100 times and fitted to a line to get the slope, which represents a simulated LPR calculation. The black dots represent the frequency distribution of the simulated LPR after repeating this process 10,000 times. The red line is a Gaussian fit with mean 0.89 and standard deviation of 0.08. In this example,

Figure A.I.10, continued: the deviation of the mean from 1.0 indicates that there is a consistent under-estimation of the "true" LPR, and a roughly 8% error. The deviation from 1.0 is likely due to the presence of consistent underestimation of total cell fluorescence, as in Figure A.I.9.

APPENDIX II:

MATERIALS AND METHODS

Cell Culture and cloning

Human aortic endothelial cells (HAECs) (Lonza, CC-2535) and grown in endothelial growth media (EGM-2) supplemented with SingleQuots (Lonza, CC-3156 & CC-4176) and Antibiotic-Antimycotic (Gibco, 15240062) at 37°C with 5% CO_2. HAECs were used from passage 6 to 8 for all experiments. Human pulmonary microvascular endothelial cells (HMVEC, Lonza, C12281) were maintained in EGM2-MV medium (Lonza, CC-3202) supplemented with 10% FBS. Human umbilical vein endothelial cells (HUVEC, Lonza C2519A) were maintained in EGM2-SingleQuot medium (2% FBS). HMVECs and HUVECs were used from passage 5 to 7 for all experiments. Cell lines were verified as mycoplasma free and that they are endothelial cells with CD31 verification by the vendor.

Laconic, Lifeact, ATeam, and FLIIP-glu700 expression

Laconic, ATeam, or FLIIPglu700 containing plasmid (Addgene: 44238, 51958, and 17866 respectively) were cloned into Ad5 adenovirus by VectorLabs for construction of Adenovirus-Laconic (Ad-Lac), Adenovirus-ATeam (ad-ATeam), or adenovirus-FLIIPglu700 (ad-Glu). Ad-Lifeact-RFP (ad-Lifeact) was from Ibidi (60122). For transduction into endothelial cells, Ad-Lac at 50:1 multiplicity of infection (MOI), ad-ATeam at 100:1 MOI, and ad-Glu at 200:1 MOI in 1:1 viral media (DMEM high glucose + 10 mM HEPES) and 3 μL GeneJammer (Agilent, 204130) per milliliter of final volume was added for 1 hour before replacement with complete media (EGM2). For migration and contraction experiments, ad-Lac and ad-Lifeact were co-transduced each with

MOI 50:1. Endothelial cells were used 48 hours post transduction to allow for cell recovery and maximal fluorescence.

T7-eBFP2, T7-mCherry, and RhoA overexpression

eBFP2 and mCherry constructs were generated from the Addgene plasmid #64323 and GeneCopoeia EX-C0726-M56-PFKFB3, respectively. For RhoA overexpression, pcDNA3-EGFP-RhoA-WT, pcDNA3-EGFP-RhoA-Q63L (Constitutively Active/CA), pcDNA3-EGFP-RhoA-T19N (Dominant Negative/DN) were purchased from Addgene (12965, 12968, 12967). EGFP was cloned out of each construct and replaced with either mScarlet-i (Addgene 85056 pLifeact-mScarlet-i_N1) or eBFP2 using the vector and insert primers in Table A.II.1, followed by Gibson assembly (NEB, E2611). PCR products containing T7 promotors for *in vitro* transcription were generated using NEB Q5 polymerase (New England Biolabs, M0491) and the primers (Integrated DNA Technologies) listed in Table A.II.1.

Table A.II.1: RhoA, mCherry, and eBFP2 overexpression primers

Name	**Forward Primer (5' -> 3')**	**Reverse Primer (5' -> 3')**
RhoA-Vector	GCATGGACGAGCTGTACAAGGAATTCATGGCT	TCCTCGCCCTTGCTCACCATGGTGGCAAGCTT
eBFP2- Insert	GGAGACCCAAGCTTGCCACCATGGTGAGCAAGGGCGAGGAG	CGGATGGCAGCCATGAATTCCTTGTACAGCTCGTCCATGCCGAGAG
mScarlet-i-Insert	GGAGACCCAAGCTTGCCACCATGGTGAGCAAGGGC	CGGATGGCAGCCATGAATTCCTTGTACAGCTCGTCCATGCC
T7-eBFP2	TAATACGACTCACTATAGGGAGATGCGGTGACGTGGAGGAGAATCCCGGCCCTGCTAGC	TAGAAGGCACAGTCGAGG
T7-mCherry	TAATACGACTCACTATAGGTACAAAGTGGTTCGATCTAGAATGGCTAGCATGGTGAGCAAGGGCGAGGAGGATAACATGGCC	TAGAAGGCACAGTCGAGG
T7-RhoA	TAATACGACTCACTATAGGG	TAGAAGGCACAGTCGAGG

mRNA transcripts were generated using mMESSAGE mMACHINE T7 Ultra Kit (ThermoFisher, AM1345). HAECs were transfected with 50 ng/cm^2 of mRNA with Lipofectamine MessengerMAX (ThermoFisher, LMRNA003) overnight in 20% Opti-MEM:EGM2. On the day of the LPR assay, cells, each dually transfected with either A) mCherry and Laconic or B) eBFP2 and Laconic, were split into two groups – A and B by themselves or mixed together into an Ibidi chamber.

Jurkat T Cells were gifted from Dr. Hans Schreiber (University of Chicago) and kept in RPMI 1640 (Corning, 10-040-CV) supplemented with 10% FBS (X&Y Cell Culture, FBS-500), Penicillin and Streptomycin (Gibco, 15140). Cells were stimulated with PMA/Ionomycin stimulation cocktail (Biolegend, 423301) in complete media per manufacturers recommendations for the time indicated per experiment. For imaging experiments, cells were adhered to the imaging chambers (Ibidi, 80176) using 0.1% poly-l-lysine (Sigma, P8920).

Electroporation of Jurkat T cells was performed using the Neon Transfection system (ThermoFisher, MPK5000) and 10 μg/2E6 cells of maxi-prepped (Zymo, D4027) Laconic plasmid (Addgene, 44238) using 1,350 v pulse voltage and 10 ms pulse width over 3 pulses. Cells were used 48 hours post electroporation to allow for cell recovery and maximal fluorescence.

RhoA-Flare Expression

HAECs were plated 5 × 10^4 cells/well in 8-well glass bottom dish (Ibidi 80827) two days prior to the experiment. One day prior to the experiment, RhoA-Flare (Addgene, 12150) plasmid was incubated with fluorine-modified polyethylenimine (F-PEI) at a 4:1 plasmid:F-PEI mass ratio for 30 minutes in serum-free media (Opti-MEM) then incubated with cells for 4 hrs at 37 °C. The F-PEI were synthesized according to a previous method[50]. Briefly, heptafluorobutyric anhydride was

added to PEI with a molar ratio of 7:1 then trimethylamine was added as 1.5-fold mole to heptafluorobutyric anhydride. This was stirred for 48 hours at room temperature then dialyzed with distilled water in a bag with a molecular weight cut off of 1 kDa. Media was exchanged after the 4 hr incubation to complete endothelial growth medium (EGM2) and cells were imaged the following day.

Thrombin, lysophosphatidic acid, Y27632, latrunculin B, para-amino-blebbistatin, or 2DG treatment

HAECs were first starved in EBM2 or Fluorobrite medium (Gibco, A1896701) for at least two hours prior to thrombin treatment for 10 minutes. Thrombin was used at 0.25 U/mL for all experiments except for Fig. 4d, which was 0.5 U/mL for 7-10 minutes prior to assay. Cells were treated with lysophosphatidic acid for 30 minutes prior to assay. Y27632, latrunculin B, para-amino blebbistatin, or 2DG containing samples were starved in EBM2 or Fluorobrite for one hour prior to thrombin treatment.

Metabolomics

Endothelial cells were plated at 500,000 cells/well using 6-well plates. Metabolites were extracted according to the manufacturer's protocol for metabolomics (HMT Metabolomics). The average lactate concentration measured by capillary electrophoresis time-of-flight mass spectrometry was 37973.5 ± 29376.25 pmol per million of cells. Assuming an average length, height, and aspect ratio of 100 mm, 4 mm, and 1.12, respectively[51], the estimated lactate concentration per cell was 0.77 ± 0.82 mM.

Laconic imaging

Imaging of Laconic sensor was performed on an Olympus IX-71 microscope with a 10× objective. FRET filter sets were from Semrock: excitation 438/24, mTFP emission 483/32, Venus emission 542/27, and dichroic FF458-Di02. Hoechst and TRITC filter set for visualizing Hoechst stain, eBFP2, and mCherry were from Semrock: Hoescht excitation 337/50, Hoescht emission, 447/60, Hoescht dichroic FF409-Di03, TRITC excitation 556/20, TRITC emission 617/73, TRITC dichroic Di03-R488/561. FRET images were taken in rapid succession using a computer controlled Prior filter excitation and emission wheels and a Photometrics 95B camera. The microscope system was enclosed in a heated chamber maintained at 37 ^{o}C and 5% CO_2 for all time-lapse microscopy experiments. The microscope system was controlled by MicroManager. Imaging flow chambers (Ibidi, 80176) were used according to the manufacturer's instructions. Injections for exchanging buffers were performed manually through attached tubing.

Laconic calibration

Ad-Laconic were transduced into HAECs and were replated into Ibidi chambers at approximately 100,000 cells / chamber 24 hours later, and then imaged 24 hours later. 1 x 10^6 Laconic-electroporated Jurkat T cells were seeded into each poly-lysine coated ibidi chambers 30 minutes prior to imaging. Cells were incubated in intracellular buffer (ICB) (10 mM NaCl, 130 mM KCl, 1.25 mM HEPES pH 7.2) with 10 μM nigericin and 2 μM of rotenone with varying concentrations of sodium lactate (0.0001 mM, 0.001 mM, 0.01 mM, 0.1 mM, 1 mM and 10 mM). mTFP and Venus fluorescence channel images were acquired every 2 seconds over 3 minutes per lactate concentration. The mTFP/Venus (donor/acceptor) intensity ratio per cell after background subtraction (hereafter, 1/FRET or FRET' in shorthand) was obtained after segmentation (described below).

Lactate concentration and production rate (LPR) calculation

One day after Ad-Lac transduction, HAECs were re-plated into Ibidi chambers at approximately 100,000 cells / chamber. After waiting another 24 hours, they were starved in extracellular buffer (ECB) composed of (112 mM NaCl, 5 mM KCl, 1.25 mM CaCl2, 1.25 mM MgSO4, 10 mM HEPES, 24 mM NaHCO3, pH 7.4) or Fluorobrite MEM (Gibco, A1896701) for at least 1 hour. The first injection was 10 mM glucose in ECB, then after 3 minutes, 10 mM glucose and 500 μM of pCMBA in ECB. The fluorescence images of mTFP and Venus were obtained with exposures between 100-300 ms/frame every 2 seconds until completion of the assay. LPRs were calculated as follows: after pCMBA injection, the FRET' rose ($FRET^{-1}$) as cells accumulated intracellular lactate. From the FRET' vs lactate calibration curve, we define *c* as a constant in Equation 1 which we use in Equation 2 to finally define LPR in Equation 3.

Eq. 1 $$\frac{\Delta FRET^{-1}}{\Delta Log_{10}Lactate} = c$$

Eq. 2 $$\frac{\Delta FRET^{-1}}{\Delta t} = c\frac{\Delta Log_{10}Lactate}{\Delta t}.$$

Eq. 3 $$LPR = \frac{\Delta Log_{10}Lactate}{\Delta t}.$$

Intracellular lactate was determined by first estimating the FRET' signal at zero lactate, which was after starvation for 1 hour in extracellular buffer and perfusion with 10 mM pyruvate. Following 10 mM glucose perfusion, the FRET' signal reached steady state after 2 minutes. At the end of each experiment, the FRET' value at 10 mM lactate was measured such that each individual cell had its own two-point calibration curve. An average FRET' value over 20 seconds during steady state was used to determine intracellular lactate.

DMOG stimulation of endothelial cells

HAECs were plated to confluency and transduced with Ad-Lac at 50 MOI two days prior to the LPR assay. One day prior to the LPR assay, cells were transfected with either T7-eBFP2 or T7-mCherry at 50 ng/cm2. The night before the assay, the cells were treated with 0.5 mM of DMOG or DMSO in EGM2. On the day of the LPR assay, cells, each dually labeled with either A) mCherry and Laconic or B) eBFP2 and Laconic, were split into two groups – A and B by themselves or mixed together into an Ibidi chamber.

RhoA-Q63L or RhoA-T19N expression in endothelial cells

HAECs were plated to confluency and transduced with Ad-Lac at 50 MOI two days prior to the LPR assay. One day prior to the LPR assay, cells were transfected with either T7-eBFP2-RhoA-Q63L, T7-mScarlet-i-RhoA-T19N, T7-eBFP2-RhoA-T19N, or T7-mScarlet-i-RhoA-Q63L at 25 ng/cm2. On the day of the LPR assay, cells, each dually labeled with either A) mScarlet-i and Laconic or B) eBFP2 and Laconic, were split into two groups – A and B by themselves or mixed together into an Ibidi chamber.

siRNA expression in endothelial cells with LPR measurements

Two days prior to the LPR assay, HAECs plated to confluency were transduced with with Ad-Lac at 50 MOI, Ad-ATeam at 100 MOI, or Ad-FLIIP-Glu700 at 200 MOI. 12 hours later the cells were transfected with either scrambled control or siRNA targeted towards SLC2A3 as above.

Deep learning enabled segmentation of cells

Sample generation for ground truth

Endothelial cells were transduced with Ad-Lac at 50 MOI as above. After 48 hours of transduction, cells were fixed for immunofluorescence as described above for VE-Cadh (CDH5) to mark cell boundaries and stained with Hoechst (1:1000). Samples were then stored at 4^{o}C wrapped in parafilm to be imaged at a later time. Images of cells were acquired in the FRET channel and Hoechst channel at 10× magnification.

Ground truth labeling

Cellprofiler[52] was used for ground truth labeling of 4 classes: background, border, cytoplasm, and nuclei. First, 1200´1200 pixel images in the FRET channel were background corrected with subtraction using a running average block size of 150 pixels across all images of the fixed samples. Next, using an adaptive threshold (Otsu) strategy, nuclei were identified after staining with Hoechst dye. Using nuclei as seeds, cell boundaries were found through the propagation algorithm. The cytoplasm was then defined as areas inside the cell boundaries (through immunofluorescence labeling with anti-CDH5 and secondary antibody anti-rabbit-Alexa 488), but not of the nuclei. Next, these images were recombined and labeled with a unique class identifier. Minor adjustments to the labeled images were made algorithmically and automatically in MATLAB, including making sure that a cell boundary encapsulates all cytoplasm and nuclei, and getting rid of cells that had no nuclei. Images of each label class were generated and visually inspected for accuracy. 432 images containing approximately 500 cells per image were used for training as described below. Of note, ground truth labeling required separate nuclei and boundary staining procedures which would have to be repeated on each separate dataset for precise determination of cell boundaries. This makes fast determination of LPR without manual boundary tracing impractical (I routinely collect hundreds of cells in each experiment). With deep learning, it became possible to avoid the two extra staining procedures and thereby significantly increases experimental throughput, and has the added benefit of being generalizable to other cell types and magnifications.

Deep-learning enabled semantic segmentation

The 432 image data set with labeled ground truth was randomized into training (70%), validation (15%), and test (15%) datasets. To enhance the dataset, patches were extracted and augmented with random reflection, rotation, and shear up to 10 degrees. Next, a U-net network (Ronneberger, Fischer, and Brox 2015) (Figure 2.2C) was trained using conventional deep learning, with final layer pixel classification consisting of an inverse class weighting (based on class frequency) cross entropy loss function over 50 epochs. 128´128 image tile size was chosen, with 8 mini-batches, using stochastic gradient of descent with 0.95 momentum (~38,000 unique images prior to augmentation; Background pixels: 2.93×10^8; Border pixels: 2.81×10^7; Cell body pixels: 9.15×10^7; Nuclei pixels: 2.54×10^7). Initial learning rate was 0.001 and was dropped by a factor of 10 every 10 epochs. The training was performed in MATLAB using the Deep Learning Toolbox on 2 NVIDIA GeForce 1080 Ti and 1 NVIDIA Titan V GPU. Total training time was about 96 hours and was stopped after no further reduction of loss. In this manner, a semantic segmentation network capable of assigning each pixel a separate class was created. Measures of deep learning accuracy are listed in Table 2.1. We found that inclusion of a nuclei class improved the classification of cell boundaries. Adding additional 2D convolutional layers to increase the receptive field did not improve the network accuracy but significantly reduced the learning rate. Convolutional layers had 3×3 kernel size. Skip connections were included in the U-net as depicted in Figure 2.2C.

Image Analysis

After feeding images into the semantic segmentation network, the output was further processed to remove cells below a pre-defined threshold, based on expected cell size. Next, FRET' trajectories of each cell over time were generated. To accomplish this, individual cells were extracted from the

labeled images: each cell was identified as an object surrounded by a boundary class and containing a nucleus. The mean position of the cell was matched to a cell with the closest position in a subsequent image, thus generating a position trajectory, and therefore FRET' trajectory (computed as the average mTFP fluorescence intensity divided by the average Venus fluorescence intensity inside the boundary minus background signal) of every cell. The FRET' trajectories were then subjected to a median filter of width 5 for denoising. To obtain the lactate production rate, pyruvate production rate, or glucose uptake rate, the slope of the FRET' (or regular FRET for glucose sensor) signal was calculated over 40 second trajectories and fit against a linear model during the portion of the time the cells were exposed to MCT1 inhibitor. ATP levels were determined by the average FRET signal before and after addition of agonist. Only if the R^2 value of the fit was greater than 0.9 was the data considered useable. Conversion of FRET' to LPR was calculated as described above.

Quantification of image analysis error

I estimated the error in deep learning assisted semantic segmentation by first computing the error between ground truth fluorescence and segmented fluorescence. First, we used a test data set of cells expressing Laconic for which we have ground truth and segmented these images with the deep learning algorithm. Then using the same image analysis pipeline, we plot the cell fluorescence as estimated from deep learning networks against the ground truth cell fluorescence (n ~ 20,000). The 95% confidence interval of the slope is 0.93-0.95, so there was consistently a small underestimation of the true fluorescence of each cell (Figure 2.2D).

To estimate how this error in fluorescence detection affects fitting of LPR data, we turn to Monte Carlo simulations of LPR (bootstrapping). Using the dataset (Figure 2.2D) which provides a real measure between ground truth and fluorescence, we generate a line x = y by randomly sampling

the ground truth fluorescence, each of which corresponds to a deep-learning generated fluorescence, 100 times. The slope of this line is then calculated by performing linear regression. This random sampling of fluorescence values, followed by slope calculation, simulates LPR calculation in real samples. The distribution of these bootstrapped slopes is plotted after repeating this 10,000 times, resulting in a Gaussian distribution of slopes (Figure 2.3C). The red line is fit to a Gaussian. The mean of the fit Gaussian is 0.9, similar to the correlation between ground truth and deep learning fluorescence above (0.94). The standard deviation of the Gaussian fit is 0.05. Thus, the error in estimating LPR, due to semantic segmentation, is 0.05/0.9 which is approximately 5%.

Per-pixel LPR

Cells were seeded into Ibidi chambers and the same protocol followed when imaging LPR as above, with the exception that a 40× plan-apochromat Olympus objective was used for imaging. After acquisition of the images, a tophat filter with width of 30 microns (in real space) was used to estimate the background. A Gaussian with width of 1 pixel was convolved with the original image to smooth noise artifact. To this smoothened image, the minimum of the estimated background image was subtracted. FRET' was calculated by dividing the mTFP image from the YFP image. Following, the per pixel LPR was calculated after binning by 4 in an average sense in each image in the time series (after addition of pCMBA). The slope of each super pixel in the time series was then calculated; the value of the slope was replotted as the LPR image. LPR images were then resized to the original size.

Actin turnover and overlap calculations Ten Lifeact-RFP images, taken 1 minute apart, were subtracted from each other in sequential order, and the maximum intensity of each of these difference images was projected as the final "difference" image. Both the Lifeact difference image

and LPR images were normalized to the largest value in the respective image. To calculate the Manders' Overlap Coefficient (MOC) or Pearson's Correlation Coefficient (PCC) (complementary statistical measures of spatial correlation) between the Lifeact difference image and the per pixel LPR image, Lifeact difference images were first segmented by hand. The mask of the cell was then applied to the LPR per pixel image to avoid background effects. Next, the actin difference image was thresholded at 5% of maximum intensity. Finally, the MOC and PCC were calculated as in equations 4 and 5, respectively.

Eq. 4
$$MOC = \frac{\sum_{i,j} x_{i,j} \cdot y_{i,j}}{\sum_{i,j} x_{i,j} \sum_{i,j} y_{i,j}}$$

Eq. 5
$$PCC = \frac{\sum_{i,j} (x_{i,j} - \langle x_{i,j} \rangle) \cdot (y_{i,j} - \langle y_{i,j} \rangle)}{\sum_{i,j} (x_{i,j} - \langle x_{i,j} \rangle) \sum_{i,j} (y_{i,j} - \langle y_{i,j} \rangle)}$$

where x and y are Lifeact difference and LPR images with i rows and j columns, and $\langle \cdots \rangle$ operator denotes mean. Simulated MOC or PCC was performed by randomizing the spatial location of the LPR pixel values within the masked area and calculating the MOC or PCC with the thresholded Lifeact difference image 10,000 times.

RhoA imaging, LPR vs RhoA activity

RhoA-Flare imaging was performed with FRET filter sets purchased from Semrock: excitation 438/24, mTFP emission 483/32, Venus emission 542/27, and dichroic FF458-Di02 on transfected cells. Integration times ranged from 100ms to 500ms with a Photometrics Prime95b camera using either a 40× or 100× plan-apochromat Olympus objective. Single cell LPR was performed on separate cells as described above. To calculate the LPR or RhoA activity as a function of distance from center, the cells were first segmented by hand in ImageJ. Line scan intensities of either RhoA activity (FRET) or LPR were performed from the geometric center of the cell to the edge of the contracting or non-contracting portions of the cell. These line scans were then normalized to

maximum intensity and interpolated using cubic splines to the same number of data points (1000). The signals were then averaged to produce the final figure. Each line scan in the category of contractile or not is from a different cell.

Mouse studies

Gene Expression Omnibus datasets (GEOD) were downloaded from EndoDB (https://endotheliomics.shinyapps.io/endodb/), a database of curated endothelial transcriptomics datasets[31]. All mouse endothelial datasets are of isolated primary cells in the untreated (control) arms of the experiments.

All animal care and treatment procedures were approved by the University of Chicago Institutional Animal Care and Use Committee. Animals were handled according to the National Institutes of Health Guide for the Care and Use of Laboratory Animals and all experiments were compliant with ethical guidelines from The Guide for the Care and Use of Laboratory Animals. All experimental animals were assigned unique identifiers to blind experimenter to treatment. For the mouse model of vascular leak, C57BL/6J mice were purchased from Jackson Laboratories (Bar Harbor, ME). All experimental animals were maintained in a pathogen-free environment with a humidity of 40-60%, a temperature of 20–24 °C, and a 12-h light/dark cycle at the University of Chicago. For *in vivo* human SLC2A3 or mScarlet-i transient overexpression, C57BL/6 mice, 10–12 wk old, were tail vein-injected with the solution containing 40 mg of endotoxin-free CDH5-SLC2A3 overexpression plasmid, CDH5-mScarlet-i, or control CDH5a containing plasmid DNA diluted with sterile 5% glucose and then mixed with polyethylenimine **(**PEI) nanoparticles (TurboFect *in vivo* Transfection Reagent) (Thermo Scientific) according to manual instructions. After 24 hours, mice were anesthetized with ketamine-xylazine (80 mg/kg:20 mg/kg) before

harvest of aorta and intimal RNA isolation, Evans blue assay, or fixation, paraffin-embedding and sectioning for visualization of mScarlet-i.

Evans blue dye assay

After anesthesia, retro-orbital injection of 4 mL/g of 2% Evans blue dye was performed. 1 hour later, aortas were immediately cleaned and harvested, photographed, and weighed. Evans blue dye was extracted from the aortas by sonication in 50% trichloroacetic acid (4 mL/mg). Each sample was centrifuged, and the supernatant mixed with 100% ethanol in a 1:3 ratio. The OD of each sample was read at 620 nm on a Biotek-3 instrument and normalized to aorta weight.

Aorta intima isolation for qRT-PCR

After careful isolation, the aorta was quickly flushed with 350 μl of Qiazol lysis reagent (Qiagen) using a 29G insulin syringe and the elute was collected in a microfuge tube for intimal RNA isolation. The leftover aorta after flushing with Qiazol was homogenized with 700 μl of Qiazol for RNA isolation of media and adventitia. Reverse transcription and qRT-PCR were performed using the Maxima First Strand cDNA Synthesis Kit (ThermoFisher) according to manufacturer's protocol. Mouse PCR primers are listed above.

Fluorescence of aortic intima

CDH5-mScarlet-i transfected aortas were fixed in 4% paraformaldehyde for 15 minutes and embedded in OCT after being immersed in OCT:sucrose=1:1 mixed solution for 24 hours. Frozen samples were sectioned in 5-8 μm. The sections were then mounted, permeabilized, blocked, and incubated with antibody to CDH5, followed by fluorescent secondary antibody (as above).

Samples were then incubated with ProLong Gold with DAPI (Thermo Fisher) and imaged with a confocal microscope (Olympus).

Statistics

The data were analyzed in Prism 9 (GraphPad Software Inc, La Jolla, CA). All data with error bars were shown as mean ± standard error of the mean (SEM) except for the metabolomics estimate which was the mean ± standard deviation (SD) (Fig. 1) to better highlight the distribution of intracellular lactate levels. Statistical significance was determined by unpaired Welch's t-test for individual differences and one-way ANOVA followed by Bonferroni's test for multiple comparisons. All t-tests were two-tailed. All experiments were biological replicates except for extracellular flux experiments, which included technical replicates. All measurements were taking from distinct samples.

Reagents and primary antibodies

Dimethyloxalylglycine (DMOG) (Sigma-Aldrich, D3695) was used at 500 μM final concentration. For monocarboxylate transporter 1 (MCT1) blockade, 4-chloromercuribenzoic acid (pCMBA) (Sigma-Aldrich, C5913) at 500 μM was used. Nigericin (Tocris, 4312), oligomycin (Millipore, 495455), Antimycin A (Sigma-Aldrich, A8674) were used at 1 μM. 2-deoxyglucose (Sigma-Aldrich, D8375) working concentration was 50 mM. Thrombin working concentration was 0.25-0.5 U/mL (Fisher, T4393). Lysophosphatidic acid (Santa Cruz, sc-2010503) working concentration was 10 μM. Y27632 (Tocris, 1254) working concentration was 10 μM. Latrunculin B (Sigma, 48020) working concentration was 20 nM. Para-amino blebbistatin (AxolBio, ax494682) working concentration was 50 μM. Antibodies for immunofluorescence: SLC2A3 (R&D Systems, MAB1415, 12.5 μg/mL), CDH5/VE-CADH (Cell Signaling, 2500S, 1:250 dilution), Phalloidin (PromoFluor 546, PK-PF546-7, 1:200). Antibodies for Western blot: SLC2A3 (ProteinTech, 20403-1-AP, 1:1000 dilution), SLC2A1 (ProteinTech, 21829-1-AP,

1:1000), pCFL (Cell Signaling, 3313T, 1:1000 dilution), tCFL (Cell Signaling, 5175T, 1:1000 dilution), ppMLC (Cell Signaling, 3674S, 1:1000 dilution), tMLC (Sigma, M4401, 1:1000 dilution), ACTB (Abcam, ab6276, 1:1000 dilution). Secondary antibodies: anti-Mouse IgG-HRP (Calbiochem 401253, 1:3000) or anti-Rabbit IgG-HRP (Cell Signaling 7074S, 1:5000).

siRNA and transfection

siRNAs targeting SLC2A3 (Qiagen, SI04250106, SI04313554, SI04359425) or SLC2A1 (Qiagen, SI03089401) and non-targeting siRNAs (Qiagen, 1027310) were purchased. The transfection (12.5 nM) was performed using Lipofectamine RNAiMAX (Life Technologies) in 20% Opti-MEM:EGM2. Cells were seeded 24 hours prior to siRNA treatment. After 48 hours, experiments were performed.

Western blot

Whole cell extracts were harvested with 1× SDS lysis buffer and separated by 12% Bis-Tris Protein Gels and transferred to PVDF membrane using Biorad Gel Transfer System (Biorad). After blocking with either 5% BSA in Tris-buffered saline with 0.1% Tween 20 (TBST) for 1 hour, the membranes were incubated with primary antibody against proteins of interest overnight at 4^{o}C, washed in TBST then followed by incubation with an HRP-conjugated secondary antibody for 1 hour at room temperature. Blots were developed with the ECL system (Pierce). Luminescence was detected by a ChemiDoc MP Imager (Bio-rad). Saturating luminescence of the protein of interest was avoided; occasionally, non-specific bands were allowed to saturate in order to maximize signal of the protein of interest. The bands were segmented by hand, the average value of each band obtained, and the background subtracted. Every effort was made to blot all proteins on a single

blot. However, strip and re-probe sometimes resulted in unusable images. Thus, samples were run on separate gels in equivalent amounts when this issue arose. All proteins were normalized to b-actin from the same blot, and phosho-proteins were thereafter normalized to total (phospho-CFL/total-CFL and phospho-MLC/total-MLC). Bands of different molecular weights were imaged after cutting. All original blots displayed in this dissertation can be found in the corresponding manuscript (Wu & Harrison, 2021) as the Source Data.

Quantitative real-time PCR (qRT-PCR)

Total RNA was isolated using Direct-zol RNA MiniPrep (Zymo Research) after Trizol lysis (ThermoFisher) (800 mL/35 mm dish). mRNA was reverse-transcribed into cDNA using High Capacity cDNA Reverse Transcription kit (Life Technologies). cDNA quantification was performed on LightCycler 480 II (Roche) using SYBR Green I Master for mRNA. Quantification of each gene of interest was normalized to beta-actin using the power up technique. PCR primers are listed in Table A.II.2.

Table A.II.2: Quantitative real-time PCR (qRT-PCR) primers

Name	Forward Primer (5'à3')	Reverse Primer (5'à3')
Human primers		
b-actin	TCCCTGGAGAAGAGCTACGA	AGGAAGGAAGGCTGGAAGAG
SLC2A1	GAACTCTTCAGCCAGGGTCC	ACCACACAGTTGCTCCACAT
SLC2A2	AGCTGGCCATCGTCACGGGC	GTAGCAGAGACTGAAGGATG
SLC2A3	CGTGGAGAAAACTTGCTGCTG	TCAGAGCTGGGGTGACCTTC
SLC2A4	TTCCAGTATGTTGCGGAGGC	TCTGTGCTGGGTTTCACCTC
SLC2A5	GAGCAACAGGATCAGAGCATG	GTTGACAGCAGCCACGTTGTA
SLC2A6	CTCAGCTTCATGCCCAACTC	GATACTCGGCTGCTCTGTCT
SLC2A7	TTCCATTGGGCCCAGTCCT	GGCAGATTCCGGCAAAGATG

SLC2A8	GGTCAACGCCGTCATGTTCT	CGCCCTGCTCTGTCCATGATG
SLC2A9	CGCCTTCGGCTCCTCCTTCCT	AGAGTGTCTGGGTCTATTGGA
SLC2A10	CTCGCCATGGGCCACT	ATGAGGAAGCCACCAACCAG
SLC2A11	CTGACCATCTGCGCTGCCG	GTGGCTCTCCAGTACGCGC
SLC2A12	GGGAAGCGGCTGTAACTTCT	TAAACATGCCGCAGCCTCTC
SLC2A13	AGACTGCGGTTTCTGCTACAA	TTCATTTTCACACCTGCCCC
SLC2A14	TGCATATGATAGGCCTTG	GGCCCTGGCTGAAGAGTT
Mouse primers		
b-actin	GATCAAGATCATTGCTCCTCCTG	AGGGTGTAAAACGCAGCTCA

Extracellular flux assay

Glycolytic rates were measured using the XFe24 Extracellular Flux Analyzer (Agilent). HAECs were seeded at a density of 6×10^4/well on Seahorse plates (Agilent, 100777) overnight in a standard incubator. Cells were next equilibrated with XF Base media (Agilent, 102353) at 37°C for one hour in an incubator lacking CO_2. Following an injection of 10 mM glucose, the average of 11 combined biological and technical replicates were quantified as the extracellular acidification rate (ECAR). Cell counts were performed post-Seahorse assays by Hoechst staining of nuclei, followed by imaging and counting cells with MATLAB via thresholding and regionprops command. Visual inspection was used to determine accuracy of algorithmic counting.

Electrical cell impedance assay

Cell permeability was evaluated by measuring transendothelial electrical resistance (TEER) across HAEC monolayers on 8-well electrode arrays 8W10E+ (Applied Biophysics) by an electrical cell-substrate impedance sensing system Model 1600R (Applied Biophysics). Cells were starved in EBM2 media for 2 hours prior to thrombin treatment. 40,000 cells/well were plated into 8-well electric cell-substrate impedance sensing (ECIS) chambers (Applied Biophysics, Inc. 8W10E+

PET) two days before each experiment. Plates were transferred to the ECIS apparatus in a CO_2, temperature, and humidity-controlled incubator. Impedance measurements were taken every 10 seconds at 4,000 Hz. For 2DG treatment, cells were pre-treated with 50 mM 2DG in EBM2 for 1 hour before thrombin addition. For glucose titration, cells were incubated in DMEM containing indicated amounts of glucose for one hour before thrombin addition. For siRNA experiments, cells were treated with 5 nM Scramble or SLC2A3 siRNA for 2 days prior to thrombin addition. For rescue experiments, cells were treated with 1 μM oligomycin 1 hour prior to thrombin addition. Change in impedance was defined as by .

Immunofluorescence protocol and TIRF imaging

After experiments were performed, cells in 8-well chambers (LabTek II) were fixed in PBS containing 4% formaldehyde (10 min), permeabilized with 0.25% Triton X-100 in TBS containing 0.1% Tween 20 (30 min), and blocked with 2% BSA in TBS containing 0.1% Tween 20 (TBST) (30 min). In between each step, the samples were washed with PBS three times. To stain SLC2A3, cells were incubated with mouse monoclonal antibody against SLC2A3 in 2%BSA in TBST overnight at 4^{o}C, followed by Alexa Flour 594 Goat Anti-Mouse IgG (1:1000 dilution in TBST, Life Technologies, A11037) for 1 hour at room temperature after 3 PBS washes. To stain VE-Cadherin, cells were incubated with rabbit polyclonal antibody against VE-Cadherin (CDH5) in 2% BSA in TBST overnight at 4^{o}C, followed by Alexa Flour 488 Goat Anti-Rabbit IgG (1:1000 dilution in TBST, Life Technologies, A11034) for 1 hour at room temperature after 3 PBS washes. TIRF microscopy was performed using a 532-nm laser line and epifluorescence microscopy was performed using a 470-nm LED on a Nikon Ti-2 microscope.

Flow microscopy assay

A flow device consisting of a computerized stepper motor UMD-17 (Arcus Technology, Livermore, CA) and a 1° tapered stainless steel cone was used to generate the physiologically-relevant shear stress pattern[4]. The flow device was placed in a 37°C incubator with 5% CO_2 on top of the inverted microscope. HAECs at 100% confluence, maintained in EGM2- medium containing 4% dextran in 6-well plates, were subjected to unidirectional steady flow (UF) or disturbed flow (DF) for 24 hours before cells being imaging. Following flow and performing of the LPR assay, the shear stress applied to the cells was measured below.

Measurement of flow shear stress

To measure the local shear stress in the cone and plate device, 1:10,000 dilution of 2 mM red microspheres (Spherotech, FH-206-2) in PBS were added to the cells following overnight flow and LPR assessment on top of the microscope. The flow was slowed to $1/20^{th}$ the original speed in order to track beads. Imaging was performed at a sufficient rate (30 Hz) to ensure that sequential images contained the same beads. The focus was kept at the apical surface of the cells. To track the beads, the background was estimated with a boxcar averaging filter with filter width of 22 pixels (the average microsphere size was about 5 pixels). To the background corrected image, a Gaussian filter with standard deviation of 1 pixel was applied to remove uncorrelated noise. Next, to identify microspheres, regions containing bead-sized objects were extracted from the images and filtered for cell debris (objects too large or too small). This method selected for in-focus microspheres along the apical surface of the endothelial cells, giving a good estimate of the local shear stress. Microspheres in sequential images were assumed to be the same if they were closest to each other. By computing bead displacement in sequential frames, a velocity profile orthogonal to the rotation axis was built up.

Migration / scratch assay

HAECs were plated 2×10^5 cells/well in 12-well plates and transduced with Ad-Lac and Ad-Lifeact one day prior to the assay. For higher magnification of migration, HAECs were plated 5×10^4 cells/well in 8-well glass bottom dishes (Ibidi 80827). A 10 mL pipette tip was gently passed once over the cells to produce a wound. Following the scratch, the media was changed in order to minimize floating debris. The cells were then placed on the microscope for time-lapse microscopy. After sufficient cell migration into the wound, the LPR assay was performed as described above. For analysis of cell migration, we measured the LPR of cells that had migrated more than 90 μm, which is 2 standard deviations greater than the mean migration distance.

Granule tracking of SLC2A3

Following immunofluorescence, images were acquired in epifluorescence for CDH5 (excitation 470 nm) and by TIRF (excitation 532 nm) for SLC2A3 on a Nikon Ti-2 microscope. SLC2A3 images were first convolved with a rolling disk filter of width 3 times the estimated size of a granule to estimate the true background. The original image was convolved with a Gaussian with width 1 pixel to suppress pixel noise. To this image, the background image was subtracted. This restored image was further processed by eliminating single pixel regions which were judged to be processing artifact. The remaining regions were identified as SLC2A3 granules. To determine which SLC2A3 granules lay on cells, cells were identified by simple background thresholding of CDH5 images. The fluorescence intensities of SLC2A3 granules when CDH5 signal was positive were then tabulated on a per-image basis.

Gap index and gap size index determination

At 10× magnification with 1.5× multiplier, all CDH5 or phalloidin images (with or without thrombin, with or without siSLC2A3) were cropped to eliminate non-uniform vignetting; images were then flattened and thresholded to determine foreground. The gap size index ((intercellular gap area/cell number) was determined by ([intercellular gap area/total cell area]×1000)/cell number) and gap index ((number of intercellular gaps/cell number) was calculated by ([intercellular gap number/total cell area]×1000)/cell number) according to Fraccaroli et al[1]. All data points reflecting gap index and gap size index are individual images.

HUVEC size determination

After thrombin treatment or not, HUVECs were fixed, permeabilized, and stained with phalloidin as described above. Images were then flattened as above. A threshold was used to find fluorescent cells which were counted in MATLAB.

Construction of CDH5 plasmids

The original plasmid containing CDH5 promoter was a gift from Dr. Youyang Zhao at Northwestern University. CDH5 promoter sequence was verified by sequencing. CDH5control plasmid was engineered by using NEBuilder HiFi DNA Assembly Cloning kit (NEB#5520) with the following primers (Table A.II.3). The original plasmid containing SLC2A3 (pDONR223_SLC2A3_wt) open reading frame was obtained from Addgene (#81787). SLC2A3 open reading frame was amplified with primers (Table A.II.3) and then assembled with the backbone fragment amplified from CDH5 control plasmid with primers (Table A.II.3) using NEBuilder HiFi DNA Assembly Cloning kit.

The original plasmid containing mScarlet-i (pLifeact-mScarlet-i-N1) (Addgene #85056) was used as the backbone fragment amplified with the following primers: mScarlet_F

(gctcaccggtGCCACCATGGTGAGCAAG), and mScarlet_R3 (tcacaacccgATGCATGGCGGTAATACG). The resulting fragment was then assembled with CDH5 promoter fragment amplified from CDH5_control plasmid with the following primers: CDH5(truncated)_F(cgccatgcatCGGGTTGTGAATGeAGGTCTG), CDH5(truncated)_R (ccatggtggcACCGGTGAGCTCTGTGGAG) by using NEBuilder HiFi DNA Assembly Cloning kit.

Table A.II.3: CDH5-Glut3 construction primers

Name	**Sequence**
CDH5control plasmid	
CDH5pro_v8F	tctgcttaggGCCAATTCTGCAGACAAATG
CDH5pro_v8R	gtcatcgtcCTTATAGTCCATGGTGGC
FLAG_Neg_v3F	ggactataagGACGATGACGACAAGTGATC
FLAG_Neg_v3R	cagaattggcCCTAAGCAGATTCTTCATGC
SLC2A3 ORF amplification	
Glut3_F	tgacgacaagATGGGGACACAGAAGGT
Glut3_R	tcgaggctgaTCAGACATTGGTGGTGGT
CDH5 control plasmid backbone amplification	
CDH5_BK for Glut3_F	caatgtctgaTCAGCCTCGACTGTGCCTTC
CDH5_BK for Glut3_R	gtgtccccatCTTGTCGTCATCGTCCTTATAGTCC

CONTRIBUTION STATEMENT

In order to properly credit my colleagues and collaborators, I created this section to give outline their contributions. First, Dave Wu and I have worked together and collaborated daily throughout my PhD. Dave and I both generate hypotheses, design experiments, execute experiments, analyze data, interpret results and write-up findings. However, Dave has been instrumental in putting together the code for segmentation and analysis, as well as running the western blots. Second, I must thank Teodora Szasz from the Research and Computing Center (RCC) at UChicago for her help in rigorously testing and evaluating our deep-learning pipeline. My labmates and collaborators Angelo Meliton, Chih-Fan Yeh, Tzu-Pin Shentu, Ru-Ting Huang, and Zhengjie Zhou helped tremendously on the *in vivo* experiments. Gökhan M. Mutlu helped design experiments and had the Seahorse bioenergetics assay. Finally, my advisors Yun Fang and Jun Huang wrote and edited manuscripts alongside Dave and me as well as helped interpret results and design experiments. I am so grateful to have worked with such smart and generous scientists!

BIBLIOGRAPHY

Almacellas, Eugènia, Joffrey Pelletier, Anna Manzano, Antonio Gentilella, Santiago Ambrosio, Caroline Mauvezin, and Albert Tauler. 2019. "Phosphofructokinases Axis Controls Glucose-Dependent MTORC1 Activation Driven by E2F1." *IScience* 20 (October): 434–48. https://doi.org/10.1016/j.isci.2019.09.040.

Almeida, Luís, Matthias Lochner, Luciana Berod, and Tim Sparwasser. 2016. "Metabolic Pathways in T Cell Activation and Lineage Differentiation." *Seminars in Immunology* 28 (5): 514–24. https://doi.org/10.1016/j.smim.2016.10.009.

Bantug, Glenn R., Lorenzo Galluzzi, Guido Kroemer, and Christoph Hess. 2018. "The Spectrum of T Cell Metabolism in Health and Disease." *Nature Reviews. Immunology* 18 (1): 19–34. https://doi.org/10.1038/nri.2017.99.

Blanchoin, Laurent, Rajaa Boujemaa-Paterski, Cécile Sykes, and Julie Plastino. 2014. "Actin Dynamics, Architecture, and Mechanics in Cell Motility." *Physiological Reviews* 94 (1): 235–63. https://doi.org/10.1152/physrev.00018.2013.

Csurka, Gabriela, Diane Larlus, and Florent Perronnin. 2013. "What Is a Good Evaluation Measure for Semantic Segmentation?" In *Proceedings of the British Machine Vision Conference 2013*, 32.1-32.11. Bristol: British Machine Vision Association. https://doi.org/10.5244/C.27.32.

Dai, Guohao, Mohammad R. Kaazempur-Mofrad, Sripriya Natarajan, Yuzhi Zhang, Saran Vaughn, Brett R. Blackman, Roger D. Kamm, Guillermo García-Cardeña, and Michael A. Gimbrone. 2004. "Distinct Endothelial Phenotypes Evoked by Arterial Waveforms Derived from Atherosclerosis-Susceptible and -Resistant Regions of Human Vasculature." *Proceedings of the National Academy of Sciences of the United States of America* 101 (41): 14871–76. https://doi.org/10.1073/pnas.0406073101.

Danthinne, X., and M. J. Imperiale. 2000. "Production of First Generation Adenovirus Vectors: A Review." *Gene Therapy* 7 (20): 1707–14. https://doi.org/10.1038/sj.gt.3301301.

Davies, P. F. 1995. "Flow-Mediated Endothelial Mechanotransduction." *Physiological Reviews* 75 (3): 519–60. https://doi.org/10.1152/physrev.1995.75.3.519.

Davies, Peter F., Mete Civelek, Yun Fang, and Ingrid Fleming. 2013. "The Atherosusceptible Endothelium: Endothelial Phenotypes in Complex Haemodynamic Shear Stress Regions in Vivo." *Cardiovascular Research* 99 (2): 315–27. https://doi.org/10.1093/cvr/cvt101.

De Bock, Katrien, Maria Georgiadou, Sandra Schoors, Anna Kuchnio, Brian W. Wong, Anna Rita Cantelmo, Annelies Quaegebeur, et al. 2013. "Role of PFKFB3-Driven Glycolysis in Vessel Sprouting." *Cell* 154 (3): 651–63. https://doi.org/10.1016/j.cell.2013.06.037.

Diebold, Lauren P., Hyea Jin Gil, Peng Gao, Carlos A. Martinez, Samuel E. Weinberg, and Navdeep S. Chandel. 2019. "Mitochondrial Complex III Is Necessary for Endothelial Cell

Proliferation during Angiogenesis." *Nature Metabolism* 1 (1): 158–71. https://doi.org/10.1038/s42255-018-0011-x.

Doddaballapur, Anuradha, Katharina M. Michalik, Yosif Manavski, Tina Lucas, Riekelt H. Houtkooper, Xintian You, Wei Chen, et al. 2015. "Laminar Shear Stress Inhibits Endothelial Cell Metabolism via KLF2-Mediated Repression of PFKFB3." *Arteriosclerosis, Thrombosis, and Vascular Biology* 35 (1): 137–45. https://doi.org/10.1161/ATVBAHA.114.304277.

Fazal, Fabeha, Kaiser M. Bijli, Mohd Minhajuddin, Theo Rein, Jacob N. Finkelstein, and Arshad Rahman. 2009. "Essential Role of Cofilin-1 in Regulating Thrombin-Induced RelA/P65 Nuclear Translocation and Intercellular Adhesion Molecule 1 (ICAM-1) Expression in Endothelial Cells." *The Journal of Biological Chemistry* 284 (31): 21047–56. https://doi.org/10.1074/jbc.M109.016444.

Feng, Shuang, Neil Bowden, Maria Fragiadaki, Celine Souilhol, Sarah Hsiao, Marwa Mahmoud, Scott Allen, et al. 2017. "Mechanical Activation of Hypoxia-Inducible Factor 1α Drives Endothelial Dysfunction at Atheroprone Sites." *Arteriosclerosis, Thrombosis, and Vascular Biology* 37 (11): 2087–2101. https://doi.org/10.1161/ATVBAHA.117.309249.

Fessel, Joshua P., Rizwan Hamid, Bryan M. Wittmann, Linda J. Robinson, Tom Blackwell, Yuji Tada, Nobuhiro Tanabe, Koichiro Tatsumi, Anna R. Hemnes, and James D. West. 2012. "Metabolomic Analysis of Bone Morphogenetic Protein Receptor Type 2 Mutations in Human Pulmonary Endothelium Reveals Widespread Metabolic Reprogramming." *Pulmonary Circulation* 2 (2): 201–13. https://doi.org/10.4103/2045-8932.97606.

Fraccaroli, Alessia, Bettina Pitter, Abdallah Abu Taha, Jochen Seebach, Stephan Huveneers, Julian Kirsch, Ricardo P. Casaroli-Marano, et al. 2015. "Endothelial Alpha-Parvin Controls Integrity of Developing Vasculature and Is Required for Maintenance of Cell-Cell Junctions." *Circulation Research* 117 (1): 29–40. https://doi.org/10.1161/CIRCRESAHA.117.305818.

Goddard, Lauren M., and M. Luisa Iruela-Arispe. 2013. "Cellular and Molecular Regulation of Vascular Permeability." *Thrombosis and Haemostasis* 109 (3): 407–15. https://doi.org/10.1160/TH12-09-0678.

Halestrap, Andrew P. 2013. "Monocarboxylic Acid Transport." *Comprehensive Physiology* 3 (4): 1611–43. https://doi.org/10.1002/cphy.c130008.

Harrison, Devin L., Yun Fang, and Jun Huang. 2019. "T-Cell Mechanobiology: Force Sensation, Potentiation, and Translation." *Frontiers in Physics* 0. https://doi.org/10.3389/fphy.2019.00045.

Harrison, Devin L., David Wu, Jun Huang, and Yun Fang. 2021. "Single-Cell Lactate Production Rate as a Measure of Glycolysis in Endothelial Cells.," *Cell STAR Protocols* [Accepted in principle]

Heerden, Johan H. van, Meike T. Wortel, Frank J. Bruggeman, Joseph J. Heijnen, Yves J. M. Bollen, Robert Planqué, Josephus Hulshof, Tom G. O'Toole, S. Aljoscha Wahl, and Bas Teusink. 2014. "Lost in Transition: Start-up of Glycolysis Yields Subpopulations of Nongrowing Cells." *Science (New York, N.Y.)* 343 (6174): 1245114. https://doi.org/10.1126/science.1245114.

Hensley, Christopher T., Brandon Faubert, Qing Yuan, Naama Lev-Cohain, Eunsook Jin, Jiyeon Kim, Lei Jiang, et al. 2016. "Metabolic Heterogeneity in Human Lung Tumors." *Cell* 164 (4): 681–94. https://doi.org/10.1016/j.cell.2015.12.034.

Hu, Hai, Ashish Juvekar, Costas A. Lyssiotis, Evan C. Lien, John G. Albeck, Doogie Oh, Gopal Varma, et al. 2016. "Phosphoinositide 3-Kinase Regulates Glycolysis through Mobilization of Aldolase from the Actin Cytoskeleton." *Cell* 164 (3): 433–46. https://doi.org/10.1016/j.cell.2015.12.042.

Huang, Jun, Mario Brameshuber, Xun Zeng, Jianming Xie, Qi-jing Li, Yueh-hsiu Chien, Salvatore Valitutti, and Mark M. Davis. 2013. "A Single Peptide-Major Histocompatibility Complex Ligand Triggers Digital Cytokine Secretion in CD4(+) T Cells." *Immunity* 39 (5): 846–57. https://doi.org/10.1016/j.immuni.2013.08.036.

Huang, Ru-Ting, David Wu, Angelo Meliton, Myung-Jin Oh, Matthew Krause, Joyce A. Lloyd, Recep Nigdelioglu, et al. 2017. "Experimental Lung Injury Reduces Krüppel-like Factor 2 to Increase Endothelial Permeability via Regulation of RAPGEF3-Rac1 Signaling." *American Journal of Respiratory and Critical Care Medicine* 195 (5): 639–51. https://doi.org/10.1164/rccm.201604-0668OC.

Huang, Yan, Li Lei, Dinggang Liu, Ion Jovin, Raymond Russell, Randall S. Johnson, Annarita Di Lorenzo, and Frank J. Giordano. 2012. "Normal Glucose Uptake in the Brain and Heart Requires an Endothelial Cell-Specific HIF-1α-Dependent Function." *Proceedings of the National Academy of Sciences of the United States of America* 109 (43): 17478–83. https://doi.org/10.1073/pnas.1209281109.

Imamura, H. 2009. "Visualization of ATP Levels inside Single Living Cells with Fluorescence Resonance Energy Transfer-Based Genetically Encoded Indicators." *Proceedings of the National Academy of Sciences of the United States of America*, no. 106: 15651–56.

Jang, Cholsoon, Li Chen, and Joshua D. Rabinowitz. 2018. "Metabolomics and Isotope Tracing." *Cell* 173 (4): 822–37. https://doi.org/10.1016/j.cell.2018.03.055.

Karmaus, Peer W. F., Xiang Chen, Seon Ah Lim, Andrés A. Herrada, Thanh-Long M. Nguyen, Beisi Xu, Yogesh Dhungana, et al. 2019. "Metabolic Heterogeneity Underlies Reciprocal Fates of TH17 Cell Stemness and Plasticity." *Nature* 565 (7737): 101–5. https://doi.org/10.1038/s41586-018-0806-7.

Khan, S., and et al. 2019. "EndoDB: A Database of Endothelial Cell Transcriptomics Data." *Nucleic Acids Research*, no. 47: D736–44.

Kim, Boa, Jia Li, Cholsoon Jang, and Zoltan Arany. 2017. "Glutamine Fuels Proliferation but Not Migration of Endothelial Cells." *The EMBO Journal* 36 (16): 2321–33. https://doi.org/10.15252/embj.201796436.

Koppenol, Willem H., Patricia L. Bounds, and Chi V. Dang. 2011. "Otto Warburg's Contributions to Current Concepts of Cancer Metabolism." *Nature Reviews Cancer* 11 (5): 325–37. https://doi.org/10.1038/nrc3038.

Kuo, Andrew, Monica Y. Lee, and William C. Sessa. 2017. "Lipid Droplet Biogenesis and Function in the Endothelium." *Circulation Research* 120 (8): 1289–97. https://doi.org/10.1161/CIRCRESAHA.116.310498.

Ma, Eric H., Mark J. Verway, Radia M. Johnson, Dominic G. Roy, Mya Steadman, Sebastian Hayes, Kelsey S. Williams, et al. 2019. "Metabolic Profiling Using Stable Isotope Tracing Reveals Distinct Patterns of Glucose Utilization by Physiologically Activated CD8+ T Cells." *Immunity* 51 (5): 856-870.e5. https://doi.org/10.1016/j.immuni.2019.09.003.

Martin, A., and et al. 2014. "Imaging Mitochondrial Flux in Single Cells with a FRET Sensor for Pyruvate." *PLoS One*, no. 9: e85780.

Masters, C. 1984. "Interactions between Glycolytic Enzymes and Components of the Cytomatrix." *The Journal of Cell Biology* 99 (1 Pt 2): 222s–25. https://doi.org/10.1083/jcb.99.1.222s.

Matsuda, T., and C. L. Cepko. 2007. "Controlled Expression of Transgenes Introduced by in Vivo Electroporation." *Proceedings of the National Academy of Sciences of the United States of America* 104: 1027–32. https://doi.org/10.1073/pnas.0610155104.

Mehta, Dolly, and Asrar B. Malik. 2006. "Signaling Mechanisms Regulating Endothelial Permeability." *Physiological Reviews* 86 (1): 279–367. https://doi.org/10.1152/physrev.00012.2005.

Menard, Lynda, David Maughan, and Jim Vigoreaux. 2014. "The Structural and Functional Coordination of Glycolytic Enzymes in Muscle: Evidence of a Metabolon?" *Biology* 3 (3): 623–44. https://doi.org/10.3390/biology3030623.

Menk, Ashley V., Nicole E. Scharping, Rebecca S. Moreci, Xue Zeng, Cliff Guy, Sonia Salvatore, Heekyong Bae, et al. 2018. "Early TCR Signaling Induces Rapid Aerobic Glycolysis Enabling Distinct Acute T Cell Effector Functions." *Cell Reports* 22 (6): 1509–21. https://doi.org/10.1016/j.celrep.2018.01.040.

Mole, David R., Imre Schlemminger, Luke A. McNeill, Kirsty S. Hewitson, Christopher W. Pugh, Peter J. Ratcliffe, and Christopher J. Schofield. 2003. "2-Oxoglutarate Analogue Inhibitors of HIF Prolyl Hydroxylase." *Bioorganic & Medicinal Chemistry Letters* 13 (16): 2677–80. https://doi.org/10.1016/s0960-894x(03)00539-0.

Mookerjee, Shona A., Renata L. S. Goncalves, Akos A. Gerencser, David G. Nicholls, and Martin D. Brand. 2015. "The Contributions of Respiration and Glycolysis to Extracellular Acid

Production." *Biochimica Et Biophysica Acta* 1847 (2): 171–81. https://doi.org/10.1016/j.bbabio.2014.10.005.

Morgan, Stacy-Anne, Dana C Nadler, Rayka Yokoo, and David F Savage. 2016. "Biofuel Metabolic Engineering with Biosensors." *Current Opinion in Chemical Biology*, Energy Mechanistic Biology, 35 (December): 150–58. https://doi.org/10.1016/j.cbpa.2016.09.020.

Nieuw Amerongen, G. P. van, S. van Delft, M. A. Vermeer, J. G. Collard, and V. W. van Hinsbergh. 2000. "Activation of RhoA by Thrombin in Endothelial Hyperpermeability: Role of Rho Kinase and Protein Tyrosine Kinases." *Circulation Research* 87 (4): 335–40. https://doi.org/10.1161/01.res.87.4.335.

Nieuw Amerongen, G. P. van, M. A. Vermeer, and V. W. van Hinsbergh. 2000. "Role of RhoA and Rho Kinase in Lysophosphatidic Acid-Induced Endothelial Barrier Dysfunction." *Arteriosclerosis, Thrombosis, and Vascular Biology* 20 (12): E127-133. https://doi.org/10.1161/01.atv.20.12.e127.

Nieuw Amerongen, Geerten P. van, Pieter Koolwijk, Amanda Versteilen, and Victor W. M. van Hinsbergh. 2003. "Involvement of RhoA/Rho Kinase Signaling in VEGF-Induced Endothelial Cell Migration and Angiogenesis in Vitro." *Arteriosclerosis, Thrombosis, and Vascular Biology* 23 (2): 211–17. https://doi.org/10.1161/01.atv.0000054198.68894.88.

Norris, Vic, Patrick Amar, Guillaume Legent, Camille Ripoll, Michel Thellier, and Judit Ovádi. 2013. "Sensor Potency of the Moonlighting Enzyme-Decorated Cytoskeleton: The Cytoskeleton as a Metabolic Sensor." *BMC Biochemistry* 14 (1): 3. https://doi.org/10.1186/1471-2091-14-3.

Park, Jin Suk, Christoph J. Burckhardt, Rossana Lazcano, Luisa M. Solis, Tadamoto Isogai, Linqing Li, Christopher S. Chen, et al. 2020. "Mechanical Regulation of Glycolysis via Cytoskeleton Architecture." *Nature* 578 (7796): 621–26. https://doi.org/10.1038/s41586-020-1998-1.

Pertz, Olivier, Louis Hodgson, Richard L. Klemke, and Klaus M. Hahn. 2006. "Spatiotemporal Dynamics of RhoA Activity in Migrating Cells." *Nature* 440 (7087): 1069–72. https://doi.org/10.1038/nature04665.

Pollard, Thomas D., and Robert D. Goldman. 2018. "Overview of the Cytoskeleton from an Evolutionary Perspective." *Cold Spring Harbor Perspectives in Biology* 10 (7): a030288. https://doi.org/10.1101/cshperspect.a030288.

Rhee, Jerry M., Melinda K. Pirity, Chantal S. Lackan, Jonathan Z. Long, Gen Kondoh, Junji Takeda, and Anna-Katerina Hadjantonakis. 2006. "In Vivo Imaging and Differential Localization of Lipid-Modified GFP-Variant Fusions in Embryonic Stem Cells and Mice." *Genesis* 44 (4): 202–18. https://doi.org/10.1002/dvg.20203.

Riedl, Julia, Alvaro H. Crevenna, Kai Kessenbrock, Jerry Haochen Yu, Dorothee Neukirchen, Michal Bista, Frank Bradke, et al. 2008. "Lifeact: A Versatile Marker to Visualize F-Actin." *Nature Methods* 5 (7): 605–7. https://doi.org/10.1038/nmeth.1220.

Ronneberger, Olaf, Philipp Fischer, and Thomas Brox. 2015. "U-Net: Convolutional Networks for Biomedical Image Segmentation." In *Medical Image Computing and Computer-Assisted Intervention – MICCAI 2015*, edited by Nassir Navab, Joachim Hornegger, William M. Wells, and Alejandro F. Frangi, 234–41. Lecture Notes in Computer Science. Cham: Springer International Publishing. https://doi.org/10.1007/978-3-319-24574-4_28.

San Martín, Alejandro, Sebastián Ceballo, Iván Ruminot, Rodrigo Lerchundi, Wolf B. Frommer, and Luis Felipe Barros. 2013. "A Genetically Encoded FRET Lactate Sensor and Its Use to Detect the Warburg Effect in Single Cancer Cells." *PloS One* 8 (2): e57712. https://doi.org/10.1371/journal.pone.0057712.

Sasmal, Dibyendu K., Wei Feng, Sobhan Roy, Peter Leung, Yanran He, Chufan Cai, Guoshuai Cao, et al. 2020. "TCR-PMHC Bond Conformation Controls TCR Ligand Discrimination." *Cellular & Molecular Immunology* 17 (3): 203–17. https://doi.org/10.1038/s41423-019-0273-6.

Sasmal, Dibyendu K., Laura Pulido, Shan Kasal, and Jun Huang. 2016. "Single-Molecule Fluorescence Resonance Energy Transfer in Molecular Biology." *Nanoscale* 8 (48): 19928–44. https://doi.org/10.1039/c6nr06794h.

Song, JJ, R Haque, X Song, and F Lei. 2016. "C-Myc Regulation by Notch Signaling Modulates T Cell Differentiation." *The Journal of Immunology*. https://www.jimmunol.org/content/196/1_Supplement/121.16.

Sonveaux, Pierre, Tamara Copetti, Christophe J. De Saedeleer, Frédérique Végran, Julien Verrax, Kelly M. Kennedy, Eui Jung Moon, et al. 2012. "Targeting the Lactate Transporter MCT1 in Endothelial Cells Inhibits Lactate-Induced HIF-1 Activation and Tumor Angiogenesis." *PLOS ONE* 7 (3): e33418. https://doi.org/10.1371/journal.pone.0033418.

Sorbara, L. R., T. M. Davies-Hill, E. M. Koehler-Stec, S. J. Vannucci, M. K. Horne, and I. A. Simpson. 1997. "Thrombin-Induced Translocation of GLUT3 Glucose Transporters in Human Platelets." *The Biochemical Journal* 328 (Pt 2) (December): 511–16. https://doi.org/10.1042/bj3280511.

Takanaga, Hitomi, Bhavna Chaudhuri, and Wolf B. Frommer. 2008. "GLUT1 and GLUT9 as Major Contributors to Glucose Influx in HepG2 Cells Identified by a High Sensitivity Intramolecular FRET Glucose Sensor." *Biochimica Et Biophysica Acta* 1778 (4): 1091–99. https://doi.org/10.1016/j.bbamem.2007.11.015.

Tang, Maoxue, Guangping Gao, Carlos B. Rueda, Hang Yu, David N. Thibodeaux, Tomoyuki Awano, Kristin M. Engelstad, et al. 2017. "Brain Microvasculature Defects and Glut1 Deficiency Syndrome Averted by Early Repletion of the Glucose Transporter-1 Protein." *Nature Communications* 8 (January): 14152. https://doi.org/10.1038/ncomms14152.

Tang, Xiaoning, Yongmei Huang, Jinli Lei, Hui Luo, and Xiao Zhu. 2019. "The Single-Cell Sequencing: New Developments and Medical Applications." *Cell & Bioscience* 9 (1): 53. https://doi.org/10.1186/s13578-019-0314-y.

Trepat, Xavier, Zaozao Chen, and Ken Jacobson. 2012. "Cell Migration." *Comprehensive Physiology* 2 (4): 2369–92. https://doi.org/10.1002/cphy.c110012.

Van Valen, David A., Takamasa Kudo, Keara M. Lane, Derek N. Macklin, Nicolas T. Quach, Mialy M. DeFelice, Inbal Maayan, Yu Tanouchi, Euan A. Ashley, and Markus W. Covert. 2016. "Deep Learning Automates the Quantitative Analysis of Individual Cells in Live-Cell Imaging Experiments." *PLoS Computational Biology* 12 (11): e1005177. https://doi.org/10.1371/journal.pcbi.1005177.

Vandenbroucke, Emily, Dolly Mehta, Richard Minshall, and Asrar B. Malik. 2008. "Regulation of Endothelial Junctional Permeability." *Annals of the New York Academy of Sciences* 1123 (March): 134–45. https://doi.org/10.1196/annals.1420.016.

Wang, Ruoning, Christopher P. Dillon, Lewis Zhichang Shi, Sandra Milasta, Robert Carter, David Finkelstein, Laura L. McCormick, et al. 2011. "The Transcription Factor Myc Controls Metabolic Reprogramming upon T Lymphocyte Activation." *Immunity* 35 (6): 871–82. https://doi.org/10.1016/j.immuni.2011.09.021.

Wang, Zhong, Mark Gerstein, and Michael Snyder. 2009. "RNA-Seq: A Revolutionary Tool for Transcriptomics." *Nature Reviews. Genetics* 10 (1): 57–63. https://doi.org/10.1038/nrg2484.

Wilhelm, K., and et al. 2016. "FOXO1 Couples Metabolic Activity and Growth State in the Vascular Endothelium." *Nature*, no. 529: 216–20.

Windt, Gerritje J. W. van der, David O'Sullivan, Bart Everts, Stanley Ching-Cheng Huang, Michael D. Buck, Jonathan D. Curtis, Chih-Hao Chang, et al. 2013. "CD8 Memory T Cells Have a Bioenergetic Advantage That Underlies Their Rapid Recall Ability." *Proceedings of the National Academy of Sciences* 110 (35): 14336–41. https://doi.org/10.1073/pnas.1221740110.

Wu, Congqing, Ru-Ting Huang, Cheng-Hsiang Kuo, Sandeep Kumar, Chan Woo Kim, Yen-Chen Lin, Yen-Ju Chen, et al. 2015. "Mechanosensitive PPAP2B Regulates Endothelial Responses to Atherorelevant Hemodynamic Forces." *Circulation Research* 117 (4): e41–53. https://doi.org/10.1161/CIRCRESAHA.117.306457.

Wu, David, Devin L. Harrison, Teodora Szasz, Chih-Fan Yeh, Tzu-Pin Shentu, Angelo Meliton, Ru-Ting Huang, et al. 2021. "Single-Cell Metabolic Imaging Reveals a SLC2A3-Dependent Glycolytic Burst in Motile Endothelial Cells." *Nature Metabolism* 3 (5): 714–27. https://doi.org/10.1038/s42255-021-00390-y.

Wu, David, Ru-Ting Huang, Robert B. Hamanaka, Matt Krause, Myung-Jin Oh, Cheng-Hsiang Kuo, Recep Nigdelioglu, et al. 2017. "HIF-1α Is Required for Disturbed Flow-Induced Metabolic Reprogramming in Human and Porcine Vascular Endothelium." *ELife* 6 (May): e25217. https://doi.org/10.7554/eLife.25217.

Yao, Linpeng, Xing Xue, Peipei Yu, Yicheng Ni, and Feng Chen. 2018. "Evans Blue Dye: A Revisit of Its Applications in Biomedicine." *Contrast Media & Molecular Imaging* 2018: 7628037. https://doi.org/10.1155/2018/7628037.

Yu, Pengchun, Kerstin Wilhelm, Alexandre Dubrac, Joe K. Tung, Tiago C. Alves, Jennifer S. Fang, Yi Xie, et al. 2017. "FGF-Dependent Metabolic Control of Vascular Development." *Nature* 545 (7653): 224–28. https://doi.org/10.1038/nature22322.

Zhang, Di, Zhanyun Tang, He Huang, Guolin Zhou, Chang Cui, Yejing Weng, Wenchao Liu, et al. 2019. "Metabolic Regulation of Gene Expression by Histone Lactylation." *Nature* 574 (7779): 575–80. https://doi.org/10.1038/s41586-019-1678-1.

Zhang, Jing, Jonathan Muri, Gillian Fitzgerald, Tatiane Gorski, Roberto Gianni-Barrera, Evi Masschelein, Gommaar D'Hulst, et al. 2020. "Endothelial Lactate Controls Muscle Regeneration from Ischemia by Inducing M2-like Macrophage Polarization." *Cell Metabolism* 31 (6): 1136-1153.e7. https://doi.org/10.1016/j.cmet.2020.05.004.

Zhang, Linwen, and Akos Vertes. 2018. "Single-Cell Mass Spectrometry Approaches to Explore Cellular Heterogeneity." *Angewandte Chemie (International Ed. in English)* 57 (17): 4466–77. https://doi.org/10.1002/anie.201709719.